
Article:

Kalucka, J, Bierhansl, L, Conchinha, NV et al. (36 more authors) (2018) Quiescent Endothelial Cells Upregulate Fatty Acid β-Oxidation for Vasculoprotection via Redox Homeostasis. Cell Metabolism, 28 (6). 881-894.e13. ISSN 1550-4131

https://doi.org/10.1016/j.cmet.2018.07.016

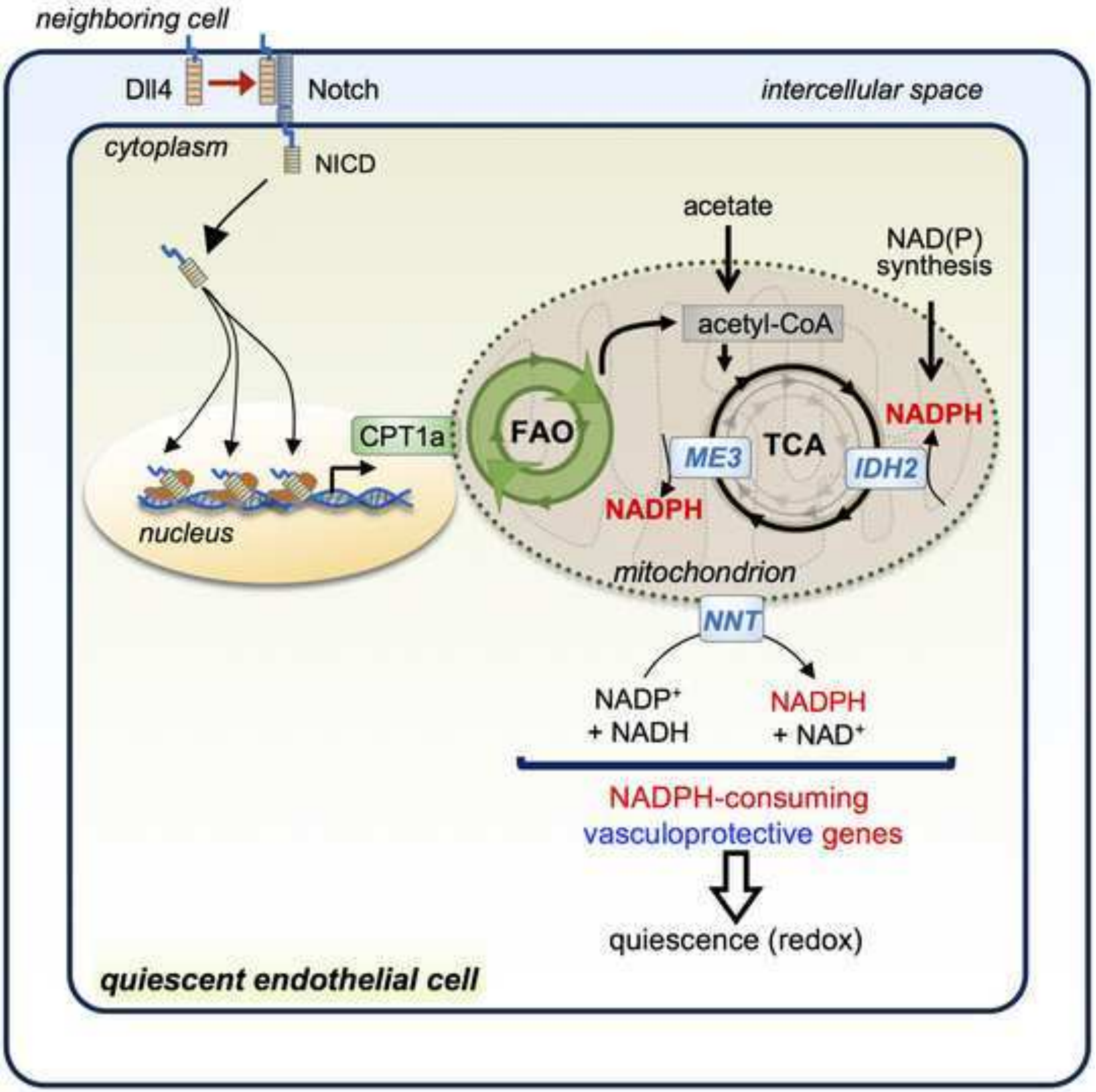
neighboring cell
Dll4
Notch
intercellular space
cytoplasm
NICD
acetate
NAD(P) synthesis
acetyl-CoA
CPT1a
FAO
TCA
NADPH
ME3
IDH2
NADPH
nucleus
mitochondrion
NNT
NADP⁺ + NADH
NADPH + NAD⁺
NADPH-consuming vasculoprotective genes
quiescence (redox)
quiescent endothelial cell

QUIESCENT ENDOTHELIAL CELLS UPREGULATE FATTY ACID β-OXIDATION FOR VASCULOPROTECTION VIA REDOX HOMEOSTASIS

Joanna Kalucka[1-3], Laura Bierhansl[1,3*], Nadine Vasconcelos Conchinha [1,3*], Rindert Missiaen[1,3*], Ilaria Elia[4,5], Ulrike Brüning[1,3], Samantha Scheinok[6], Lucas Treps[1,3], Anna Rita Cantelmo[1,3], Charlotte Dubois[1,3], Pauline de Zeeuw[1,3], Jermaine Goveia[1,3], Annalisa Zecchin[1,3], Federico Taverna[1,3], Francisco Morales-Rodriguez[1,3], Aleksandra Brajic[1,3], Lena-Christin Conradi[1,3], Sandra Schoors[1,3], Ulrike Harjes[1,3], Kim Vriens[4,5]**, **Richard Cubbon[7], Bernard Thienpont[8,9], Bert Cruys[1,3], Brian W. Wong[1,3], Bart Ghesquière[10,11], Mieke Dewerchin[1,3], Katrien De Bock[1,3#], Xavier Sagaert[12], Sebastian Jessberger[13], Elizabeth A. V. Jones[14,15], Bernard Gallez[6], Diether Lambrechts[8,9], Massimiliano Mazzone[16,17], Guy Eelen[1,3], Xuri Li[2&], Sarah-Maria Fendt[4,5] & Peter Carmeliet[1-3&#]*

(1) Laboratory of Angiogenesis and Vascular Metabolism, Center for Cancer Biology (CCB), Vesalius Research Center, VIB, Leuven, B-3000, Belgium; (2) State Key Laboratory of Ophthalmology, Zhongsan Ophthalmic Center, Sun Yat-Sen University, Guangzhou, 51006, China; (3) Laboratory of Angiogenesis and Vascular Metabolism, Department of Oncology and Leuven Cancer Institute (LKI), KU Leuven, Leuven, B-3000, Belgium; (4) Laboratory of Translational Genetics, Department of Oncology and Leuven Cancer Institute (LKI), KU Leuven, Leuven, B-3000, Belgium; (5) Laboratory of Translational Genetics, Vesalius Research Center, Center for Cancer Biology (CCB), VIB, Leuven, B-3000, Belgium; (6) Université Catholique de Louvain, Louvain Drug Research Institute, Biomedical Magnetic Resonance Research Group, Brussels, B-1200, Belgium; (7) Division of Cardiovascular and Diabetes Research, Multidisciplinary Cardiovascular Research Centre, University of Leeds, Leeds, LS2 9JT, U.K; (8) Laboratory of Translational Genetics, Department of Oncology and Leuven Cancer Institute (LKI), KU Leuven, Leuven, B-3000, Belgium; (9) Laboratory of Translational Genetics, Center for Cancer Biology, VIB, Leuven, B-3000, Belgium; (10) Metabolomics Expertise Center, VIB Center for Cancer Biology (CCB), VIB, Leuven, B-3000, Belgium; (11) Metabolomics Expertise Center, Department of Oncology, KU Leuven, Leuven, B-3000, Belgium; (12) Translational Cell & Tissue Research, Department of Imaging & Pathology, KU Leuven, Leuven, B-3000, Belgium; (13) Brain Research Institute, Faculty of Medicine and Science, University of Zurich, Zurich 8057, Switzerland; (14) Department of Cardiovascular Sciences, KU Leuven, UZ Herestraat 49, Box 911, Leuven, B-3000, Belgium; (15) Centre for Molecular and Vascular Biology, KU Leuven, UZ Herestraat 49, Box 911, Leuven, B-3000, Belgium; (16) Laboratory of Tumor Inflammation and Angiogenesis, VIB Center of Cancer Biology, Leuven, B-3000, Belgium; (17) Laboratory of Tumor Inflammation and Angiogenesis, Department of Oncology, Univeristy of Leuven, Leuven, B-3000 Belgium.

*: equal co-author; &: co-corresponding author; # lead contact
#: Present address: Laboratory of Exercise and Health, Department of Health Sciences and Technology, Swiss Federal Institute of Technology (ETH) Zurich, Schwerzenbach 8603, Switzerland

Editorial correspondence: P. Carmeliet & M. Dewerchin
phone: 32-16-37.32. 04; fax: 32-16-37.25.85
e-mail: peter.carmeliet@kuleuven.vib.be

Xuri Li
phone: 0086-20-87331815
e-mail: lixr6@mail.sysu.edu.cn

SUMMARY

Little is known about the metabolism of quiescent endothelial cells (QECs). Nonetheless, when dysfunctional, QECs contribute to multiple diseases. Previously, we demonstrated that proliferating ECs (PECs) use fatty acid β-oxidation (FAO) for *de novo* dNTP synthesis. We report now that QECs are not hypometabolic, but upregulate FAO >3-fold higher than proliferating ECs (PECs), not to support biomass or energy production, but to sustain the TCA cycle for redox homeostasis through NADPH regeneration. Hence, endothelial loss of FAO-controlling CPT1A in CPT1A$^{\Delta EC}$ mice promotes EC dysfunction (leukocyte infiltration, barrier disruption) by increasing endothelial oxidative stress, rendering CPT1A$^{\Delta EC}$ mice more susceptible to LPS and inflammatory-bowel-disease. Mechanistically, Notch1 orchestrates the use of FAO for redox balance in QECs. Supplementation of acetate (metabolized to acetyl-CoA) restores endothelial quiescence and counters oxidative stress-mediated EC dysfunction in CPT1A$^{\Delta EC}$ mice, offering therapeutic opportunities. Thus, QECs use FAO for vasculoprotection against oxidative stress-prone exposure.

INTRODUCTION

Dysfunctional endothelial cells (ECs) contribute to numerous diseases with high morbidity and mortality, including atherosclerosis, stroke, diabetes or glaucoma, affecting millions of people worldwide. Hence, reversal or prevention of EC dysfunction is a therapeutic objective, and understanding how quiescent ECs (QECs) protect themselves against dysfunction is an unmet medical need. Most ECs in a healthy adult are quiescent (Eelen et al., 2018). They mediate tissue perfusion, counteract thrombosis and vascular inflammation, and maintain vasoregulation and barrier function (Chistiakov et al., 2017). QECs are however exposed to high oxygen levels, and thus prone to oxidative stress (Polet and Feron, 2013), known to induce EC dysfunction in multiple cardiovascular disorders (Chistiakov et al., 2017). We hypothesized that QECs must therefore possess metabolic mechanisms to protect themselves against oxidative stress. However, a possible involvement of cellular metabolism in EC quiescence has not been considered, and it is unknown if metabolic changes accompany or underlie the vasculoprotective homeostatic phenotype of QECs.

Nonetheless, a role for EC metabolism is suggested. Indeed, (i) EC dysfunction can result from enhanced oxidative stress, generated by uncoupled eNOS and mitochondrial respiration (Eelen et al., 2018). (ii) Pathways sensing changes in cellular energy balance are altered by oxidative stress in dysfunctional ECs (Donato et al., 2015). (iii) Dietary glycine modulates glutathione biosynthesis, which protects ECs against oxidative stress (Ruiz-Ramirez et al., 2014). And, (iv) ROS-scavenging systems such as glutathione peroxidase require reduced glutathione (GSH), which is regenerated from its oxidized form (GSSG) by NADPH-dependent glutathione reductase (Gorrini et al., 2013). Aside from this fragmentary evidence, it remains unknown if and how QECs reprogram their metabolism to adopt a vasculoprotective phenotype.

When QECs become angiogenic, they increase glycolysis to promote migration and proliferation (De Bock et al., 2013). In proliferating ECs (PECs), fatty acid β-oxidation (FAO) is important to sustain the TCA cycle in conjunction with an anaplerotic carbon source to support nucleotide synthesis (Schoors et al., 2015), while ECs forming a vascular network in a matrix also upregulate FAO (Patella et al., 2015). In contrast, FOXO1, promoting growth arrest, decreases glycolysis in ECs (Wilhelm et al., 2016). Hence, one might expect that QECs would be hypometabolic, though this remains untested. Here, we characterized how ECs reprogram their metabolism when switching from proliferation to quiescence.

RESULTS

TRANSCRIPTOMIC SIGNATURE OF METABOLIC GENES IN QUIESCENT ENDOTHELIAL CELLS

To induce quiescence of endothelial cells, we used two complementary methods. We cultured human umbilical vein endothelial cells (referred to as “ECs”) until they were contact-inhibited (Noseda et al., 2004), or stimulated ECs with Dll4 to activate pro-quiescent Notch signaling (Harrington et al., 2008), yielding similar results. With either approach, fewer ECs proliferated, while more cells resided in the G_0 phase (Fig. 1A; Fig. S1A), and elevated expression of downstream Notch-target genes (Fig. S1B,C), without signs of senescence (Fig. S1D). We assessed global metabolic changes induced by quiescence by performing an unbiased transcriptomics analysis in proliferating ECs (PECs) *versus* quiescent ECs (QECs), focusing on the 1,444 detected metabolic genes. Correlation heatmap analysis and hierarchical clustering revealed that QECs and PECs grouped into distinct metabolic clusters ($p < 0.05$), indicating different metabolic gene signatures (Fig. 1B).

QECS UPREGULATE FATTY ACID OXIDATION

Cell quiescence has been associated with cellular hypometabolism (Wilhelm et al., 2016). Surprisingly therefore, of the 10 self-contained gene sets of central carbon metabolism, rotation gene set test (ROAST) analysis revealed that FAO was the only significantly upregulated pathway and had the highest fraction of upregulated genes of all pathways in central metabolism (FDR-adjusted p = 1.00E-04). An opposite effect or trend was observed for glycolysis, serine biosynthesis, tricarboxylic acid (TCA) cycle, oxidative phosphorylation (OXPHOS), nucleotide and fatty acid synthesis (Table S1). By heatmap and pathway mapping analysis, QECs upregulated transcripts of various FAO genes (some only modestly), while lowering transcripts of genes involved in glycolysis, TCA cycle, purine / pyrimidine synthesis and pathways contributing to nucleotide synthesis (non-oxidative pentose phosphate pathway, one carbon metabolism) (Fig. 1C,D; Fig. S1E; Table S2 & S3 for full name of genes), consistent with their lower proliferation rate and anabolic need (Fig. 1A). Since PECs utilize FAO to support nucleotide synthesis (Schoors et al., 2015), we had expected that QECs would have *lower* – not *higher* – FAO levels, since QECs synthesize fewer nucleotides as they proliferate less. We therefore focused on the surprising finding that FAO gene expression was higher in QECs than PECs.

ENDOTHELIAL CELLS INCREASE FAO FLUX WHEN BECOMING QUIESCENT

FAO flux increased when ECs became quiescent, up to 3-to 4-fold higher than in PECs (Fig. 2A,B; Fig. S2A), while glycolytic flux and glucose consumption were reduced (Fig. 2A,C,D; Fig. S2B). Glucose and glutamine oxidation, and fatty acid synthesis were also reduced in QECs (Fig. 2E-G; Fig. S2C-E). Expression of CPT1A, a rate-controlling enzyme of FAO (Schoors et al., 2015), was increased, while that of PFKFB3, a glycolytic activator (De Bock et al., 2013), declined when ECs became quiescent (Fig. 2H,I; Fig. S2F,G; Table S4). Similar metabolic changes were detected in arterial ECs (Fig. S2H,I). Use of other models of EC quiescence, based on exposing ECs to physiological shear-stress (Lin et al., 2000), confirmed higher CPT1A expression (Fig. S2J,K).

FAO IS DISPENSABLE FOR ENERGY HOMEOSTASIS, BIOMASS SYNTHESIS AND HISTONE ACETYLATION IN QECS

As cells use FAO for ATP and acetyl-CoA production (Ghesquiere et al., 2014; Xiong et al., 2018), redox homeostasis (Harjes et al., 2016), epigenetic regulation (Wong et al., 2017) or DNA synthesis (Schoors et al., 2015), we assessed for which purpose QECs increased FAO, by comparing QECs *versus* PECs, and by knockdown of CPT1A (CPT1A^{KD}) using two lentiviral vectors, each expressing a different shRNA (Schoors et al., 2015) and reducing CPT1A and FAO levels (Fig. S3A-C). This combined approach revealed that CPT1A-driven FAO was dispensable for energy homeostasis (Fig. S3D-I), biomass synthesis (Fig. S3J-R) and histone acetylation (Fig. S3S,T; Table S5), and that these processes were not affected by CPT1A^{KD}. We thus explored if QECs utilized FAO for redox homeostasis.

INCREASED CONTRIBUTION OF FATTY ACID-DERIVED CARBONS TO THE TCA CYCLE IN QECS

To analyze how QECs utilize fatty acids (FAs), we supplemented [U-^{13}C]-palmitate and determined ^{13}C-label incorporation into TCA cycle intermediates, revealing that the total contribution of ^{13}C-carbons to TCA-cycle intermediates was higher in QECs than PECs (Fig. 3A). Mass distribution analysis revealed an increase in m+4 citrate and m+3 α-ketoglutarate (αKG), fumarate and malate in QECs, suggesting that FA-derived carbons sustained an oxidative TCA cycle in QECs (Fig. 3B,C; Fig. S3U). However, even though QECs used FA-derived carbons to sustain the TCA cycle flux to a larger extent than PECs, anaplerotic replenishment of the TCA cycle by glutamine and glucose was reduced in QECs, consistent with their lower anabolism (Fig. 3D,E).

QECS INCREASE FAO FOR NADPH REGENERATION

In cancer cells, FAO regulates redox homeostasis by generating acetyl-CoA to sustain the TCA cycle (Rohrig and Schulze, 2016; Smolkova and Jezek, 2012). Indeed, the TCA cycle metabolites (iso)citrate and malate serve as substrates for reactions mediated by isocitrate dehydrogenase (IDH) and malic enzyme (ME) to regenerate NADPH from $NADP^+$ (Rohrig and Schulze, 2016; Smolkova and Jezek, 2012). Transcript levels of mitochondrial IDH2 and ME3 were higher in QECs (Fig. 4A,B), and partial knock-down of IDH2 and ME3 increased the $NADP^+$/NADPH ratio in QECs (Fig. S4A,B; more complete knock-down was toxic). NADPH levels were higher in QECs (Fig. 4C), while $CPT1A^{KD}$ lowered the elevated NADPH levels in QECs to levels observed in PECs, and increased the $NADP^+$/NADPH ratio (Fig. 4C, S4C). $CPT1A^{KD}$ did not affect NADPH regeneration in PECs (Fig. 4C), consistent with findings that PECs do not use FAO for redox homeostasis (Schoors et al., 2015). QECs expressed higher transcript levels of genes involved in NAD(P) production, including nicotinamide N-methyltransferase (NNMT), nicotinate phosphoribosyltransferase (NAPRT), NAD synthetase 1 (NADSYN1), and nicotinamide riboside kinase 1 (NMRK1) (Fig. 4D). Thus, the elevated NADPH levels in QECs result from a combined effect on increased $NADP^+$ synthesis and on regeneration of NADPH from $NADP^+$ by the increased use of FA-derived carbons to sustain the TCA cycle.

QECS HAVE REDUCED OXIDATIVE STRESS

Since NADPH is used by glutathione reductase (GR) to convert oxidized glutathione (GSSG) to its reduced form (GSH), a key cellular anti-oxidant, we measured GSSG, GSH and ROS levels, in baseline conditions and upon exposure to exogenous H_2O_2 (a measure of the cell's capacity to cope with elevated oxidative stress) (referred to as "stress conditions"). Levels of GSSG (% of total GSSG + GSH) and cellular ROS were lower in QECs, in baseline and stress conditions (Fig. 4E,F). In line, $CPT1A^{KD}$ in QECs increased ROS and GSSG levels, supporting a role of FAO in counteracting oxidative stress (Fig. 4G; Fig. S4D). Unlike PECs, QECs increased NADPH regeneration, while maintaining a lower $NADP^+$/ NADPH ratio in baseline and stress conditions (Fig. 4H; Fig. S4E). Silencing of ACADvl and HADHB ($ACADvl^{KD}$/ $HADHB^{KD}$) (catalyzing critical steps of FAO) similarly increased ROS levels (Fig. S4F-H), indicating that FAO, and not only CPT1A-mediated fatty acid import in mitochondria, controls redox homeostasis in QECs.

As different species of ROS, such us superoxide ($O_2^{\cdot -}$), hydrogen peroxide (H_2O_2) or hydroxyl radical (OH°), may have different biological functions (Birben et al., 2012; Schieber and Chandel, 2014), yet excess of each of them can trigger EC dysfunction (Incalza et al., 2018), we characterized the ROS species. Use of complementary assays revealed that mitochondrial / cellular levels of $O_2^{\cdot -}$, H_2O_2 and OH° were all reduced in QECs (Fig. S4I-O). Overall, QECs are better equipped to scavenge ROS and to cope with oxidative stress.

MOLECULAR MECHANISM OF UPREGULATION OF FAO IN QECS

As QECs upregulated Notch signaling and Notch activation promoted EC quiescence (see above), we focused on Notch as a possible transcriptional activator of CPT1A gene expression in QECs. Blocking Notch signaling with DAPT (N-[N-(3,5-difluorophenacetyl)-L-alanyl]-S-phenylglycine t-butyl ester) in QECs decreased CPT1A expression and FAO flux (Fig. 5A,B). We then investigated if Notch signaling increased CPT1A transcription. The transcriptionally active Notch intracellular domain (NICD) does not bind to DNA directly, but only via interaction with RBPJκ, a DNA-binding protein (Castel et al., 2013). Notably, we identified 4 putative RBPJκ binding motifs (Castel et al., 2013) in close proximity to the start codon of the CPT1A gene (referred to as interaction site (IS)1, IS2, IS3 and IS4) (Fig. S5A).

ChIP-qPCR analysis, using an anti-Notch1 (αNotch1) antibody that captures NICD, revealed an interaction of NICD with 3 of the 4 identified sites (IS1, IS2, IS3) in QECs, which was reduced upon treatment with DAPT (Fig. 5C; Fig. S5B,C). We also tested ECs overexpressing V5-tagged NICD ($NICD^{OE}$), which – as expected (given that Notch is a pro-quiescent signal) – were more quiescent, and had increased levels of FAO and CPT1A transcripts (Fig. S5D-G). Use of an anti-V5 tag antibody (αV5) showed that NICD interacted with IS1, IS2 and IS3 in $NICD^{OE}$ but not control ECs (Fig. 5D, Fig.S5H,I). Cloning of the CPT1A fragments, containing the IS1, IS2 and IS3 sequences, in luciferase reporter constructs with a minimal promoter confirmed that $NICD^{OE}$ enhanced the luciferase activity, as a parameter of increased CPT1A gene transcription (Fig. 5E). Thus, Notch signaling upregulates FAO flux, at least in part via induction of CPT1A gene expression. Similar analyses showed that Notch regulated the expression of IDH2 and ME3, involved in NADPH regeneration and redox homeostasis in QECs (Fig. S5J,K).

FAO INHIBITION DUE TO LOSS OF CPT1A IN QECS CAUSES OXIDATIVE STRESS *IN VIVO*

To translate our *in vitro* findings, we used two *in vivo* approaches: (i) adult 8 week old mice (containing only / primarily QECs) with a conditional inactivation of CPT1A in ECs (Cdh5(PAC)-Cre^{ERT2} - CPT1A$^{lox/lox}$ mice) upon tamoxifen treatment (referred to as "CPT1A$^{\Delta EC}$ mice") (Schoors et al., 2015) (Fig. S6A,B); and (ii) young P8 mice (in which growing blood vessel contain both PECs and QECs) treated with etomoxir, an irreversible pharmacological blocker of CPT1 that lowers FAO levels in ECs (Schoors et al., 2015).

By RNA sequencing or RT-PCR analysis, freshly isolated CPT1A$^{\Delta EC}$ QECs upregulated the expression of genes involved in redox homeostasis, presumably to restore redox homeostasis. Gene set enrichment analysis (GSEA) and pathway mapping revealed that glutathione metabolism, a key pathway in redox homeostasis, ranked among the top 3 most upregulated pathways in QECs of CPT1A$^{\Delta EC}$ mice ($p = 0.0017$; p.adjust = 0.03) (Fig. S6C; Table S6). RT-PCR confirmed the upregulation of enzymes involved in ROS scavenging (e.g. peroxiredoxin-1 [Prdx1], mitochondrial glutaredoxin-2 [Glrx2], glutathione peroxidase 3 [Gpx3]) (Fig. 6A). Also, the rate-controling enzyme of the oxidative PPP (glucose-6-phosphate dehydrogenase [G6pdx], generating NADPH in the cytosol, was upregulated in CPT1A$^{\Delta EC}$ QECs (Fig. 6B), in line with an increased oxPPP flux in QECs upon CPT1A^{KD} (Fig. S6D). Thus, CPT1A$^{\Delta EC}$ QECs upregulate metabolic pathways producing NADPH, presumably to restore redox homeostasis.

We then assessed if CPT1A$^{\Delta EC}$ QECs elevated ROS levels in intact vessels by staining for the ROS marker dihydroethidium (DHE) and the EC marker isolectin using the aorta and portal vein open book preparation (Sumiyoshi et al., 2008). DHE levels were comparable in ECs in wild type (WT) and CPT1A$^{\Delta EC}$ mice in baseline conditions (Fig. 6C,D; Fig. S6E,F). However, upon adminstration of lipopolysaccharide (LPS), which induces EC dysfunction, vascular damage and leakage because of ROS production (Kratzer et al., 2012), intracellular ROS levels in QECs were higher in CPT1A$^{\Delta EC}$ mice (Fig. 6C,D; Fig. S6E,F). Thus, CPT1A gene loss in QECs elevated ROS levels *in vivo* and rendered them more prone to oxidative stress upon an inflammatory insult, known to cause EC dysfunction.

To provide evidence for the dual role of FAO in PECs (proliferation) *versus* QECs (redox homeostasis), simultaneously occurring in a single tissue ("mixed model"), we analyzed freshly isolated ECs from growing vessels of different organs (heart, lung, liver) in control or etomoxir treated P8 mice upon EdU injection to identify EdU^{pos} PECs and EdU^{neg} QECs by flow cytometry; we measured cellular ROS levels by flow cytometry upon DHE staining. This analysis showed that, consistent with our previous findings (Schoors et al., 2015), etomoxir reduced the fraction of PECs, thus rendering the endothelium more quiescent (Fig. S6G). Coincidently, ROS levels in isolated ECs were increased upon etomoxir treatment (Fig. S6H). Given that the large majority of ECs were EdU^{neg} QECs and etomoxir further expanded this population, FAO inhibition elevated oxidative stress in QECs also in this mixed model containing both PECs and QECs.

FAO INHIBITION CAUSES EC DYSFUNCTION DUE TO OXIDATIVE STRESS

EC dysfunction due to oxidative stress is characterized by a higher pro-thrombotic state, increased adhesiveness of inflammatory leukocytes, and enhanced leakiness (Incalza et al., 2018; Kevil et al., 2000). We assessed *in vitro* if FAO inhibition by etomoxir promoted QEC activation / dysfunction, in baseline conditions and upon treatment with LPS. First, compared to control, QECs treated with etomoxir tended to have increased mRNA levels of the anti-fibrinolytic enzyme plasminogen activator inhibitor (PAI)-1 in baseline, a difference that became significant upon exposure to LPS (Fig. 6E). Second, etomoxir increased leukocyte adhesion upon activation of QECs with LPS (Fig. 6F). In agreement, infiltration of $CD45^+$ leukocytes into the lungs of $CPT1A^{\Delta EC}$ mice was increased upon LPS administration (Fig. 6G). $CPT1A^{\Delta EC}$ mice were more sensitive to LPS, as they died earlier than WT mice, indicating that reduced FAO in QECs aggravates the response to LPS (Fig. S6I). In line, at 24 hours after LPS injection, serum levels of pro-inflammatory cytokines (INF-γ, TNF-α, IL-5, IL-17, IL-23) were higher in $CPT1A^{\Delta EC}$ mice (Fig. S6J), likely contributing to the shorter survival. Third, transendothelial electrical resistance (TEER) was lower (reflecting decreased barrier function) in etomoxir-treated QECs, both in baseline and LPS conditions (Fig. 6H). In agreement, etomoxir-treated QECs contained fewer VE-cadherin$^+$ continuous stable adherens junctions, in which VE-cadherin is localized linearly along cell-cell borders (Fig. 6I,J). Accordingly, treatment of QECs with trimetazidine (TMZ), inhibiting long-chain 3-ketoacyl coenzyme A thiolase (encoded by *HADHB*), increased oxidative stress and endothelial permeability, as demonstrated by reduced TEER levels (Fig. S6K), and increased discontinuous VE-cadherin$^+$ junctions (Fig. S6L).

To assess the role of ROS, we supplemented QECs with mitoTEMPO, a scavenger of mitochondrial ROS. The induction of PAI-1 expression in etomoxir and LPS pre-treated QECs was reduced to control levels after exposure to mitoTEMPO (Fig. 6K). Also, mitoTEMPO treatment of etomoxir-treated QECs rescued the increased leakiness, induced by blocking CPT1A in QECs (Fig. 6L). Together, FAO is a safeguard for QECs to maintain redox homeostasis, and inhibition of FAO predisposes QECs to activation and dysfunction, when exposed to oxidative stress.

FAO INHIBITION ACCELERATES DSS INDUCED COLITIS

To provide additional evidence for a role of FAO in QEC homeostasis, we used a model of inflammatory bowel disease (IBD). The gut-vascular barrier (GVB) is normally impermeable, but becomes leaky in IBD, thus promoting leukocyte infiltration and aggravating disease progression (Cibor et al., 2016). Oxidative stress plays a key role in IBD by increasing GVB permeability (Tian et al., 2017). In addition to leukocytes (the major source of ROS), ECs also produce ROS in IBD (Oshitani et al., 1993). We thus hypothesized that the decreased capacity of CPT1A$^{\Delta EC}$ QECs to scavenge ROS (produced by QECs or other sources) might aggravate permeability, infiltration of leukocytes, and overall susceptibility to dextran sodium sulfate (DSS)-induced colitis.

The disease activity index (DAI) (scoring body weight loss, stool consistency, and blood in the stool and anal region) was more severe in CPT1A$^{\Delta EC}$ mice (Fig. 6M). Also, in CPT1A$^{\Delta EC}$ mice, colons shrunk more (Fig. 6N; Fig. S6M), and displayed more severe histological signs of colitis, including loss of crypts, separation of the crypt base from the muscularis mucosa and colonic wall thickening (Fig. S6N), more pronounced infiltration of CD45$^+$ leukocytes in colons (Fig. 6O), and increased vascular leakiness resulting from a breached QEC barrier (Fig. 6P). At the same time, neovessels form in the inflamed colonic mucosa, thus representing a “mixed model”. In line with previous findings (Schoors et al., 2015), the vessel area and fraction of proliferating PCNA$^+$ PECs were reduced in CPT1A$^{\Delta EC}$ mice (Fig. S6O,P), confirming that FAO has different biological roles in PECs *versus* QECs in a single tissue.

ACETATE SUPPLEMENTATION LOWERS OXIDATIVE STRESS IN QECS OF CPT1A$^{\Delta EC}$ MICE

Finally, we explored a possible translational therapeutic potential. We hypothesized that supplementation of acetate (metabolized to acetyl-CoA, a downstream product of FAO) might lower ROS levels in QECs, a finding of therapeutic relevance to counter EC dysfunction. Acetate supplementation of QECs (exposed to H_2O_2) prevented the increase in ROS levels upon CPT1A silencing (Fig. 7A). Also, treating CPT1A$^{\Delta EC}$ mice with sodium acetate prevented the increase in DHE$^+$ ROS levels in QECs upon LPS treatment (Fig.7B,C) and reduced infiltration of $CD45^+$ leukocytes into the lungs (Fig.7D). Control experiments showed that mitochondrial conversion of acetate to acetyl-CoA is essential for the rescue by acetate (Fig. S7A-G; Table S7).

DISCUSSION

QUIESCENT ECS USE FAO FOR REDOX HOMEOSTASIS

QECs are not hypometabolic, but increase FAO, up to 3- to 4-fold, the largest change of any metabolic pathway flux we observed in healthy ECs to date (De Bock et al., 2013; Huang et al., 2017; Schoors et al., 2015; Wong et al., 2017). QECs did not rely on FAO for ATP production, nucleotide synthesis or histone acetylation, unlike PECs that utilize FAO to sustain DNA synthesis (Schoors et al., 2015), or lymphatic ECs that use FAO for epigenetic regulation of lymphatic gene expression (Wong et al., 2017).

Instead, QECs utilize FAO for redox homeostasis, partly by regenerating $NADP^+$ to NADPH likely at the IDH2 and ME3 reaction steps. However, QECs also upregulate the expression of genes involved in $NADP^+$ production, contributing to improved redox homeostasis. The importance of CPT1A-driven FAO for redox homeostasis of QECs *in vivo* was supported by evidence that ROS levels were elevated after LPS challenge in QECs of $CPT1A^{\Delta EC}$ mice. As a consequence of the ROS-mediated induction of EC barrier dysfunction, leukocyte infiltration into the lung was increased and survival of $CPT1A^{\Delta EC}$ mice was compromized. A similar outcome was observed when $CPT1A^{\Delta EC}$ mice were challenged with DSS-induced colitis.

By using FAO for redox homeostasis, QECs differ from other non-transformed cell types. Indeed, certain immune, glial and neural stem cells rely on FAO for energy production (Ghesquiere et al., 2014; Stoll et al., 2015), but not for redox balance. Opposite to the anti-oxidant role of FAO in QECs, M1-like macrophages even use FAO for the production of bactericidal mitochondrial ROS (Ghesquiere et al., 2014). Only some cancer cells utilize FAO for redox control (Harjes et al., 2016), though they mostly use FAO for energy production (Qu et al., 2016), epithelial-to-mesenchymal transition (Nath and Chan, 2016), or metastasis (Pascual et al., 2017).

CONTROL OF REDOX HOMEOSTASIS BY FAO COUNTERACTS QEC DYSFUNCTION

Oxidative stress promotes EC activation / dysfunction, leading to increased vascular thrombogenicity, leakiness and inflammation (Incalza et al., 2018; Kevil et al., 2000). Consistent with a role of FAO in EC redox homeostasis, CPT1A inhibition elevated ROS levels, leading to decreased anti-fibrinolytic gene expression, vascular wall leakage *in vitro* and *in vivo*, and increased leukocyte adhesion *in vitro* and infiltration *in vivo*. Notably, treatment of QECs with a mitochondrial anti-oxidant rescued vascular leakage, a key feature of EC dysfunction. Blood vessel lining QECs are exposed to high levels of oxygen in the blood and thus to an oxidative stress-prone environment, while blood vessel forming PECs invade avascular, hypoxic areas. We speculate that QECs require a higher level of redox buffering capacity than PECs.

MOLECULAR MECHANISM: NOTCH AT A CROSSROAD

We show that Notch upregulates CPT1A, IDH2 and ME3 expression, by interacting with the DNA-binding protein RBPJκ. As such, Notch signaling constitutes a molecular switch (rheostat) that elevates FAO to produce more NADPH in QECs, though other molecular regulators may also contribute. Notch is known to inhibit DNA synthesis in ECs through induction of the cell cycle inhibitor $p27^{KIP1}$ and suppression of nuclear translocation of the cell cycle drivers cyclinD1-cdk4 (Noseda et al., 2004; Rostama et al., 2015). In agreement, we detected lower expression of nucleotide synthesis genes in QECs than PECs. This may explain how Notch signaling redirects the use of FAO from nucleotide synthesis in PECs to NADPH regeneration in QECs. Indeed, by transcriptionally lowering genes involved in nucleotide synthesis, QECs are programmed to no longer use (or use less) TCA cycle metabolites for nucleotide synthesis. Thus, even though FAO sustains the TCA cycle more in QECs than PECs, QECs are prevented from anabolic synthesis of nucleotides by the cell cycle inhibitory signaling activity of Notch. Hence, as a metabolic adaptation accompanying the cellular shift to quiescence by Notch, QECs no longer / less use FAO for nucleotide synthesis, even though FAO levels are increased, but rather to sustain the TCA cycle for NADPH regeneration. Our findings highlight the plasticity of how a single cell type (EC) can reprogram the use of the same metabolic pathway (FAO) either for nucleotide synthesis or redox homeostasis, depending on the cellular status (proliferation *versus* quiescence). Our data are not in conflict with a report that Notch signaling in ECs induces the expression of fatty acid transporters, including FABP4 (Harjes et al., 2014), and that silencing of FABP4 in PECs induces oxidative stress and inhibits tumor angiogenesis (Harjes et al., 2017), since it remains unclear if FABP4 fuels FAs to FAO and FABP4 has various FAO-independent activities (Furuhashi et al., 2014).

QECS SWITCH ON ADDITIONAL NADPH-PRODUCING VASCULOPROTECTIVE PATHWAYS

Interestingly, QECs also upregulated the expression of other NADPH-regenerating pathways, such as the oxidative PPP and nicotine nucleotide transhydrogenase (NNT; converting NADH (produced by FAO) into NADPH) (Fig. 7E), as well as NADP$^+$ producing pathways. Interestingly, QECs also upregulated the expression of enzymes such as endothelial nitric oxide synthase (NOS3), prostaglandin G/H synthase 1 (PTGS1) and glutaredoxin (GRX) (Fig. 7F-H), involved in vasculoprotection against EC dysfunction induced by oxidative stress (Egan and FitzGerald, 2006; Heiss et al., 2015). Remarkably, these vasculoprotective enzymes use NADPH as cofactor (Davidge, 2001; Ulrich et al., 2013). Hence, these findings suggest an appealing model, whereby QECs mount a broad vasculoprotective program, relying on enzymes, several of which require / consume NADPH. To meet these increased needs of NADPH, QECs reprogram their metabolism to upregulate NADPH regeneration via several complementary mechanisms, of which FAO is a major contributor.

POSSIBLE TRANSLATIONAL IMPLICATIONS?

Consistent with our findings that QECs, exposed to high oxygen levels and thus prone to oxidative stress, require FAO to secure redox homeostasis, human QECs expressed higher CPT1A levels in the highly- than poorly-oxygenated tissues tested (Fig. S7H,I). Moreover, our findings that acetate supplementation restored the ROS scavenging potential of CPT1A-silenced ECs in the LPS model, and normalized the elevated endothelial ROS levels and leukocyte infiltration in mice lacking endothelial CPT1A suggest that promoting FAO or stimulating the use of acetate-derived carbons might be beneficial to counteract EC dysfunction in disease. Given that EC dysfunction has been postulated to contribute to multiple diseases, in fact more than the dysfunction of other cell types (Dahlman et al., 2014), identifying such metabolite-based strategies to counteract / prevent EC dysfunction through improved anti-oxidant control might possibly offer therapeutic opportunities.

LIMITATIONS OF THE STUDY

Our data highlight that FAO is indispensable for maintaining redox homeostasis in ECs. Using two different disease models, we document that loss of CPT1A in ECs induces EC dysfunction, resulting from elevated oxidative stress. Our data also indicate that acetate treatment is capable of counteracting redox imbalance in conditions of CPT1A suppression. It will be interesting to explore further whether inadequate FAO levels contribute to diseases characterized by EC dysfunction due to oxidative stress, and whether acetate supplementation might have a therapeutic potential in counteracting imbalanced oxidative stress, EC dysfunction and progression of these diseases.

ACKNOWLEDGEMENTS

We thank R. Adams for providing Cdh5(PAC)-Cre^{ERT2} mice, S. Christen for help with GC-MS data interpretation and the lab members for their assistance, feedback and discussion. J.K., R.M., N.C., J.G., P.d.Z., F.R.M., C.D. and U.H. are supported by the Research Foundation Flanders (FWO); L.B. by a Leopoldina Postdoc Scholarship; L.T. by a Marie Curie-IEF Fellowship; L.-C.C. by Fritz Thyssen Stiftung. The work of R.C. is supported by funded by a British Heart Foundation Intermediate Clinical Fellowship (FS/12/80/29821); S.M.F. is supported by Marie Curie CIG, FWO-Odysseus II, Bayer Healthcare Pharmaceuticals; P.C. is supported by the VIB TechWatch program, a Federal Government Belgium grant (IUAP7/03), long-term structural Methusalem funding by the Flemish Government, grants from the Research Foundation Flanders (FWO-Vlaanderen), Foundation against Cancer (2012-175 and 2016-078) and ERC Advanced Research Grant (EU-ERC743074). X.L. is supported by the State Key Laboratory of Ophthalmology, Zhongshan Ophthalmic Center at the Sun Yat-Sen University and by the National Natural Science Foundation of China (81330021, 81670855).

AUTHOR CONTRIBUTIONS

All authors were involved in experiments and/or data analysis; JK, LB, NC, RM & PC designed experiments; BG, GE, MD, MM, DL, SMF & XL contributed to the execution, support and analysis of experiments, data interpretation and/or advice; JK, LB & NC made the figures; JK & PC largely wrote the paper; PC conceptualized the study. All authors discussed the results and commented on the manuscript.

DECLARATION OF INTEREST: P.C. declares to be named as inventor on patent applications, claiming subject matter related to the results described in this paper. The other authors declare no competing financial interests.

AUTHOR INFORMATION: Correspondence and requests for materials should be addressed to PC (peter.carmeliet@kuleuven.vib.be).

REFERENCES

Belousov, V.V., Fradkov, A.F., Lukyanov, K.A., Staroverov, D.B., Shakhbazov, K.S., Terskikh, A.V., and Lukyanov, S. (2006). Genetically encoded fluorescent indicator for intracellular hydrogen peroxide. Nat Methods *3*, 281-286.

Benedito, R., Roca, C., Sorensen, I., Adams, S., Gossler, A., Fruttiger, M., and Adams, R.H. (2009). The notch ligands Dll4 and Jagged1 have opposing effects on angiogenesis. Cell *137*, 1124-1135.

Birben, E., Sahiner, U.M., Sackesen, C., Erzurum, S., and Kalayci, O. (2012). Oxidative stress and antioxidant defense. World Allergy Organ J *5*, 9-19.

Cantelmo, A.R., Conradi, L.C., Brajic, A., Goveia, J., Kalucka, J., Pircher, A., Chaturvedi, P., Hol, J., Thienpont, B., Teuwen, L.A., et al. (2016). Inhibition of the Glycolytic Activator PFKFB3 in Endothelium Induces Tumor Vessel Normalization, Impairs Metastasis, and Improves Chemotherapy. Cancer Cell *30*, 968-985.

Castel, D., Mourikis, P., Bartels, S.J., Brinkman, A.B., Tajbakhsh, S., and Stunnenberg, H.G. (2013). Dynamic binding of RBPJ is determined by Notch signaling status. Genes Dev *27*, 1059-1071.

Chistiakov, D.A., Orekhov, A.N., and Bobryshev, Y.V. (2017). Effects of shear stress on endothelial cells: go with the flow. Acta Physiol (Oxf) *219*, 382-408.

Christen, S., Lorendeau, D., Schmieder, R., Broekaert, D., Metzger, K., Veys, K., Elia, I., Buescher, J.M., Orth, M.F., Davidson, S.M., et al. (2016). Breast Cancer-Derived Lung Metastases Show Increased Pyruvate Carboxylase-Dependent Anaplerosis. Cell Rep *17*, 837-848.

Cibor, D., Domagala-Rodacka, R., Rodacki, T., Jurczyszyn, A., Mach, T., and Owczarek, D. (2016). Endothelial dysfunction in inflammatory bowel diseases: Pathogenesis, assessment and implications. World J Gastroenterol *22*, 1067-1077.

Dahlman, J.E., Barnes, C., Khan, O.F., Thiriot, A., Jhunjunwala, S., Shaw, T.E., Xing, Y., Sager, H.B., Sahay, G., Speciner, L., et al. (2014). In vivo endothelial siRNA delivery using polymeric nanoparticles with low molecular weight. Nature nanotechnology *9*, 648-655.

Davidge, S.T. (2001). Prostaglandin H synthase and vascular function. Circ Res *89*, 650-660.

De Bock, K., Georgiadou, M., Schoors, S., Kuchnio, A., Wong, B.W., Cantelmo, A.R., Quaegebeur, A., Ghesquiere, B., Cauwenberghs, S., Eelen, G., et al. (2013). Role of PFKFB3-driven glycolysis in vessel sprouting. Cell *154*, 651-663.

Debacq-Chainiaux, F., Erusalimsky, J.D., Campisi, J., and Toussaint, O. (2009). Protocols to detect senescence-associated beta-galactosidase (SA-betagal) activity, a biomarker of senescent cells in culture and in vivo. Nat Protoc *4*, 1798-1806.

Donato, A.J., Morgan, R.G., Walker, A.E., and Lesniewski, L.A. (2015). Cellular and molecular biology of aging endothelial cells. J Mol Cell Cardiol *89*, 122-135.

Eelen, G., de Zeeuw, P., Treps, L., Harjes, U., Wong, B.W., and Carmeliet, P. (2018). Endothelial Cell Metabolism. Physiol Rev *98*, 3-58.

Egan, K., and FitzGerald, G.A. (2006). Eicosanoids and the vascular endothelium. Handb Exp Pharmacol, 189-211.

Fernandez, C.A., Des Rosiers, C., Previs, S.F., David, F., and Brunengraber, H. (1996). Correction of 13C mass isotopomer distributions for natural stable isotope abundance. J Mass Spectrom *31*, 255-262.

Furuhashi, M., Saitoh, S., Shimamoto, K., and Miura, T. (2014). Fatty Acid-Binding Protein 4 (FABP4): Pathophysiological Insights and Potent Clinical Biomarker of Metabolic and Cardiovascular Diseases. Clin Med Insights Cardiol *8*, 23-33.

Ghesquiere, B., Wong, B.W., Kuchnio, A., and Carmeliet, P. (2014). Metabolism of stromal and immune cells in health and disease. Nature *511*, 167-176.

Gorrini, C., Harris, I.S., and Mak, T.W. (2013). Modulation of oxidative stress as an anticancer strategy. Nat Rev Drug Discov *12*, 931-947.

Harjes, U., Bridges, E., Gharpure, K.M., Roxanis, I., Sheldon, H., Miranda, F., Mangala, L.S., Pradeep, S., Lopez-Berestein, G., Ahmed, A., et al. (2017). Antiangiogenic and tumour inhibitory effects of downregulating tumour endothelial FABP4. Oncogene *36*, 912-921.

Harjes, U., Bridges, E., McIntyre, A., Fielding, B.A., and Harris, A.L. (2014). Fatty acid-binding protein 4, a point of convergence for angiogenic and metabolic signaling pathways in endothelial cells. J Biol Chem *289*, 23168-23176.

Harjes, U., Kalucka, J., and Carmeliet, P. (2016). Targeting fatty acid metabolism in cancer and endothelial cells. Crit Rev Oncol Hematol *97*, 15-21.

Harrington, L.S., Sainson, R.C., Williams, C.K., Taylor, J.M., Shi, W., Li, J.L., and Harris, A.L. (2008). Regulation of multiple angiogenic pathways by Dll4 and Notch in human umbilical vein endothelial cells. Microvasc Res *75*, 144-154.

Heiss, C., Rodriguez-Mateos, A., and Kelm, M. (2015). Central role of eNOS in the maintenance of endothelial homeostasis. Antioxid Redox Signal *22*, 1230-1242.

Huang, H., Vandekeere, S., Kalucka, J., Bierhansl, L., Zecchin, A., Bruning, U., Visnagri, A., Yuldasheva, N., Goveia, J., Cruys, B., et al. (2017). Role of glutamine and interlinked asparagine metabolism in vessel formation. EMBO J *36*, 2334-2352.

Incalza, M.A., D'Oria, R., Natalicchio, A., Perrini, S., Laviola, L., and Giorgino, F. (2018). Oxidative stress and reactive oxygen species in endothelial dysfunction associated with cardiovascular and metabolic diseases. Vascul Pharmacol *100*, 1-19.

Kevil, C.G., Oshima, T., Alexander, B., Coe, L.L., and Alexander, J.S. (2000). H(2)O(2)-mediated permeability: role of MAPK and occludin. Am J Physiol Cell Physiol *279*, C21-30.

Kratzer, E., Tian, Y., Sarich, N., Wu, T., Meliton, A., Leff, A., and Birukova, A.A. (2012). Oxidative stress contributes to lung injury and barrier dysfunction via microtubule destabilization. Am J Respir Cell Mol Biol *47*, 688-697.

Lin, K., Hsu, P.P., Chen, B.P., Yuan, S., Usami, S., Shyy, J.Y., Li, Y.S., and Chien, S. (2000). Molecular mechanism of endothelial growth arrest by laminar shear stress. Proc Natl Acad Sci U S A *97*, 9385-9389.

Nath, A., and Chan, C. (2016). Genetic alterations in fatty acid transport and metabolism genes are associated with metastatic progression and poor prognosis of human cancers. Sci Rep *6*, 18669.

Noseda, M., Chang, L., McLean, G., Grim, J.E., Clurman, B.E., Smith, L.L., and Karsan, A. (2004). Notch activation induces endothelial cell cycle arrest and participates in contact inhibition: role of p21Cip1 repression. Mol Cell Biol *24*, 8813-8822.

Oshitani, N., Kitano, A., Okabe, H., Nakamura, S., Matsumoto, T., and Kobayashi, K. (1993). Location of superoxide anion generation in human colonic mucosa obtained by biopsy. Gut *34*, 936-938.

Pascual, G., Avgustinova, A., Mejetta, S., Martin, M., Castellanos, A., Attolini, C.S., Berenguer, A., Prats, N., Toll, A., Hueto, J.A., et al. (2017). Targeting metastasis-initiating cells through the fatty acid receptor CD36. Nature *541*, 41-45.

Patella, F., Schug, Z.T., Persi, E., Neilson, L.J., Erami, Z., Avanzato, D., Maione, F., Hernandez-Fernaud, J.R., Mackay, G., Zheng, L., et al. (2015). Proteomics-based metabolic modeling reveals that fatty acid oxidation (FAO) controls endothelial cell (EC) permeability. Mol Cell Proteomics *14*, 621-634.

Polet, F., and Feron, O. (2013). Endothelial cell metabolism and tumour angiogenesis: glucose and glutamine as essential fuels and lactate as the driving force. J Intern Med *273*, 156-165.

Qu, Q., Zeng, F., Liu, X., Wang, Q.J., and Deng, F. (2016). Fatty acid oxidation and carnitine palmitoyltransferase I: emerging therapeutic targets in cancer. Cell Death Dis *7*, e2226.

Rohrig, F., and Schulze, A. (2016). The multifaceted roles of fatty acid synthesis in cancer. Nat Rev Cancer *16*, 732-749.

Rostama, B., Turner, J.E., Seavey, G.T., Norton, C.R., Gridley, T., Vary, C.P., and Liaw, L. (2015). DLL4/Notch1 and BMP9 Interdependent Signaling Induces Human Endothelial Cell Quiescence via P27KIP1 and Thrombospondin-1. Arterioscler Thromb Vasc Biol *35*, 2626-2637.

Ruiz-Ramirez, A., Ortiz-Balderas, E., Cardozo-Saldana, G., Diaz-Diaz, E., and El-Hafidi, M. (2014). Glycine restores glutathione and protects against oxidative stress in vascular tissue from sucrose-fed rats. Clin Sci (Lond) *126*, 19-29.

Schieber, M., and Chandel, N.S. (2014). ROS function in redox signaling and oxidative stress. Curr Biol *24*, R453-462.

Schoors, S., Bruning, U., Missiaen, R., Queiroz, K.C., Borgers, G., Elia, I., Zecchin, A., Cantelmo, A.R., Christen, S., Goveia, J., et al. (2015). Fatty acid carbon is essential for dNTP synthesis in endothelial cells. Nature *520*, 192-197.

Smolkova, K., and Jezek, P. (2012). The Role of Mitochondrial NADPH-Dependent Isocitrate Dehydrogenase in Cancer Cells. Int J Cell Biol *2012*, 273947.

Stoll, E.A., Makin, R., Sweet, I.R., Trevelyan, A.J., Miwa, S., Horner, P.J., and Turnbull, D.M. (2015). Neural Stem Cells in the Adult Subventricular Zone Oxidize Fatty Acids to Produce Energy and Support Neurogenic Activity. Stem Cells *33*, 2306-2319.

Sumiyoshi, K., Mokuno, H., Iesaki, T., Shimada, K., Miyazaki, T., Kume, A., Kiyanagi, T., Kuremoto, K., Watanabe, Y., Tada, N., et al. (2008). Deletion of the Fc receptors gamma chain preserves endothelial function affected by hypercholesterolaemia in mice fed on a high-fat diet. Cardiovasc Res *80*, 463-470.

Tian, T., Wang, Z., and Zhang, J. (2017). Pathomechanisms of Oxidative Stress in Inflammatory Bowel Disease and Potential Antioxidant Therapies. Oxid Med Cell Longev *2017*, 4535194.

Ulrich, C.M., Steindorf, K., and Berger, N.A. (2013). Exercise, energy balance, and cancer. (New York: Springer).

Wilhelm, K., Happel, K., Eelen, G., Schoors, S., Oellerich, M.F., Lim, R., Zimmermann, B., Aspalter, I.M., Franco, C.A., Boettger, T., et al. (2016). FOXO1 couples metabolic activity and growth state in the vascular endothelium. Nature *529*, 216-220.

Wong, B.W., Wang, X., Zecchin, A., Thienpont, B., Cornelissen, I., Kalucka, J., Garcia-Caballero, M., Missiaen, R., Huang, H., Bruning, U., et al. (2017). The role of fatty acid beta-oxidation in lymphangiogenesis. Nature *542*, 49-54.

Xiong, J., Kawagishi, H., Yan, Y., Liu, J., Wells, Q.S., Edmunds, L.R., Fergusson, M.M., Yu, Z.X., Rovira, II, Brittain, E.L., et al. (2018). A Metabolic Basis for Endothelial-to-Mesenchymal Transition. Mol Cell *69*, 689-698 e687.

FIGURE LEGENDS

FIGURE 1: METABOLIC TRANSCRIPTOMICS OF QECS VS PECS

(**A**) Percentage of EdU^{neg} cells (left) and ^{3}H-thymidine incorporation into DNA (proliferation assay; right) in contact-inhibited QECs and PECs (n=3). DPM, disintegrations per minute. (**B**) Correlation heatmap and hierarchical cluster analysis of transcript levels of 1,444 metabolic genes of central carbon metabolism in QECs vs PECs (n=4 biological replicates with 3 technical replicates each). Color scale: red, high correlation; blue, low correlation. (**C**) Heatmap of transcript levels of FAO, oxPPP, non-oxPPP and glycolytic genes in contact-inhibited QECs and PECs (n=4 biological replicates with 3 technical replicates each). Color scale: red, high correlation; blue, low correlation. (**D**) Pathway map showing changes in transcript levels of genes in central carbon metabolism in QECs relative to PECs. Color scale: red, upregulated genes by at least 15%; gray: unchanged, change <15%; blue: downregulated by at least 15%. For full gene names, see Table S2 and S3. Statistics: mixed models statistics (A). Data are mean ± SEM; *p<0.05. See also Figure S1 and Table S1-S3.

FIGURE 2: METABOLIC ADAPTATIONS UPON INDUCTION OF EC QUIESCENCE

(**A**) Progressive changes of EC metabolism (glycolysis, red; FAO, blue) and proliferation (^{3}H-thymidine incorporation, black) during induction of contact-inhibited EC quiescence (n=4). (**B-F**) FAO (B), glycolytic rate (C), glucose consumption (D) glucose oxidation (E) and glutamine oxidation (F) in contact-inhibited QECs vs PECs (n=3-8). (**G**) Fatty acid synthesis measured by [U-^{14}C]-acetate incorporation in fatty acids, in QECs vs PECs (n=4). (**H**) Representative immunoblot (n=5) for NICD, CPT1A and PFKFB3 during induction of EC quiescence by contact inhibition. α-tubulin was used as loading control. For densitometric quantifications see Table S4. (**I**) qRT-PCR analysis of *CPT1A* in contact-inhibited QECs relative to PECs (n=5). In panels A and H, proliferating ECs (day 1) are standard proliferating cultures. In panels B-G,I: PECs were obtained by reseeding QECs, which initiates cell proliferation. DPM, disintegrations per minute. Statistics: mixed models statistics (A-C,E-G), two-tailed t test with Welch correction (D,I). Data are mean ± SEM; *p<0.05 vs day 1 (A) or vs PEC (B-G,I). See also Figure S2; S3 and Table S4, S5.

FIGURE 3: FAO-DERIVE CARBONS CONTRIBUTE TO THE TCA CYCLE IN QECS IN DLL4-INDUCED QECS

(**A**) Total contribution of ^{13}C palmitate carbons to the indicated TCA intermediates in QECs vs PECs (n=5). (**B,C**) Analysis of m+4 (B) and m+3 (C) labeled TCA intermediates (from [U-^{13}C]-palmitate) in QECs vs PECs (n=5). (**D**) Total contribution of ^{13}C glutamine carbons to α-KG (n=3). (**E**) Calculation of relative pyruvate carboxylase (PC)-dependent anaplerosis in QECs vs PECs (n=3). α-KG, α-ketoglutarate. Statistics: mixed models statistics (A-E). Data are mean ± SEM; *p<0.05.

FIGURE 4: ROLE OF FAO IN REDOX HOMEOSTASIS

(**A,B**) qRT-PCR analysis of *IDH1, IDH2* (A), and *ME1, ME2, ME3* (B) in QECs relative to PECs (n ≥ 3). (**C**) Total intracellular NADPH levels in ctrl and CPT1A^{KD} QECs or PECs (n=3). (**D**) qRT-PCR analysis of *NNMT*, *NARPT1*, *NADSYN1* and *NMRK1* in QECs relative to PECs (n ≥ 3). (**E-H**) Oxidized glutathione levels (% of total GSSG + GSH, expressed relative to PECs) in PECs and contact-inhibition induced QECs (E, n=3), intracellular ROS levels (CM-H_2DCFDA fluorescence) (F, n=8), intracellular ROS levels (CM-H_2DCFDA fluorescence) of ctrl or CPT1A^{KD} QECs in baseline and upon supplementation with H_2O_2 (50 µM, 2 hr) (G, n=5), and total intracellular NADPH levels (H, n=3) in PECs and contact-inhibition induced QECs, in baseline and upon supplementation with H_2O_2 (50 µM, 2 hr). Unless otherwise indicated, all experiments were performed using the Dll4 induced quiescence model. AU, arbitrary units. Statistics: two-tailed t test with Welch correction (A,B,D), ANOVA and Bonferroni post-hoc test (C,E,H), mixed models statistics (F, G). Data are mean ± SEM; ns, not significant; *p<0.05. See also Figure S4.

FIGURE 5: EFFECT OF NOTCH-SIGNALLING ON CPT1A EXPRESSION

(**A**) qRT-PCR analysis of *CPT1A* in QECs without or with treatment with DAPT (n=3). (**B**) FAO in QECs without or with treatment with DAPT (n=8). (**C**) ChIP-qPCR analysis of NICD binding to the *CPT1A* promoter at the NICD-RBPjκ consensus interaction site (IS) 1, 2 or 3, in PECs or QECs, treated or not with DAPT and pulled down with anti-Notch1 (αNotch1) or IgG antibody. Data are presented as percentage of input (% input) (n=4). (**D**) ChIP-qPCR analysis of NICD binding to the *CPT1A* promoter at the binding site (IS) 1, 2 or 3 in control ECs (pRRL) and in ECs overexpressing V5-tagged NICD (NICD^{OE}). Samples were pulled down with anti-V5 (αV5) or IgG antibody and the data are presented as percentage of input (% input). (n=4). (**E**) Relative luciferase activity of reporter constructs driven by a minimal promoter alone (ctrl) or together with NICD-RBPjκ interaction site 1, 2 or 3 of the *CPT1A* promoter, in control or NICD^{OE} ECs (n=3). Unless otherwise indicate, all experiments were performed using the contact-inhibition induced quiescence model. Statistics: two-tailed t test with Welch correction (A,E), mixed models statistics (B), ANOVA and Bonferroni post-hoc test (C,D). Data are mean ± SEM; *p<0.05; ns, not significant. See also Figure S5.

FIGURE 6: ROLE OF FAO IN EC BARRIER FUNCTION AND VASCULOPROTECTION *IN VIVO* AND *IN VITRO*

(**A,B**) qRT-PCR analysis of enzymes involved in glutathione metabolism (*Prdx1*, *Glrx2* and *Gpx3*)(A) and enzymes of pentose phosphate pathway (PPP) (*G6pdx*) (B) in ECs freshly isolated from wild type (WT) and EC-specific CPT1A knock-out (CPT1A$^{\Delta EC}$) mice (n ≥ 3). (**C,D**) $O_2^{\cdot -}$ formation in the portal vein in WT and CPT1A$^{\Delta EC}$ mice at 4 and 12 hours after injection of vehicle (PBS) or LPS, evaluated by staining for the oxidative fluorescent dye dihydroethidium (DHE). (C) Representative photomicrographs of portal vein open book preparations from the 12 hours treated mice, stained for DHE (red), the EC marker isolectin B4A (green) and nuclei (Hoechst; blue). Lower panels show larger magnifications of the boxed areas in the upper panels. (D) Quantification of DHE fluorescence signal normalized for Hoechst fluorescence, and expressed relative to control (n=3 independent experiments, each comprising n>4 mice per group). (**E**) qRT-PCR analysis of *PAI-1* in QECs upon single or combined treatment with etomoxir and LPS (to induce oxidative stress) (n=4). (**F**) Leukocyte adhesion to a QEC monolayer upon single or combined treatment with etomoxir and LPS (n=3). (**G**) Quantification of CD45^{+} cells in the lungs of WT and CPT1A$^{\Delta EC}$ mice, 4 hours after injection of LPS (n=6). (**H**) TEER analysis of QEC monolayers upon single or combined treatment with etomoxir and LPS (n=3). (**I**) Representative images of QECs and PECs, stained for VE-cadherin (red), without (vehicle) or with etomoxir treatment. White arrowheads denote discontinuous junctions; yellow arrowheads denote continuous junctions; asterisk denotes a gap between ECs resulting from discontinuous junctions. (**J**) Quantification of discontinuous junctions in quiescent QECs vs PECs without (vehicle) or with etomoxir treatment (n=3). (**K**) qRT-PCR analysis of *PAI-1* in QECs upon treatment with etomoxir and LPS (to induce oxidative stress) and with or without the ROS scavenger mitoTEMPO (n=3). (**L**) TEER measurements over 8 consecutive days, without (black lines) or with etomoxir treatment (red lines) and without (solid lines) or with subsequent mitoTEMPO treatment (dashed lines) (n=5). Arrows indicate initiation of treatments. (**M**) Disease activity index (DAI) of colitis in WT and CPT1A$^{\Delta EC}$ mice during treatment with 2.5% DSS in their drinking water for 7 consecutive days (n=7). (**N**) Colon length of WT and CPT1A$^{\Delta EC}$ mice after DSS treatment. The values are express relative to vehicle treated control group (n=7). (**O**) CD45^{+} cell infiltration in the colon wall in WT and CPT1A$^{\Delta EC}$ mice after DSS treatment (n=7). (**P**) Quantification of vascular leakiness (histological analysis of extravascular dextran) in WT and CPT1A$^{\Delta EC}$ mice after DSS treatment (n=7). Scale bar: 50 µm (C, upper panels), 20 µm (C, lower panels), 100 µm (I). All *in vitro* experiments were performed using the contact-inhibition induced quiescence model. Since CPT1A^{KD} reduces EC proliferation, precluding these cells to form a monolayer of contact-inhibited QECs, we treated contact-inhibited QEC with etomoxir in order to inhibit FAO, in panels E,F,H-L. Statistics: two-tailed t test with Welch correction (A,B,D,G,K,M-P), ANOVA and Bonferroni post-hoc test (E,F,J), mixed models statistics (H,L). Data are mean ± SEM; ns, not significant, * and #p<0.05. In (L) asterisks (*) denote statistical differences between control and etomoxir, hashtags (#) between etomoxir and etomoxir plus MitoTEMPO. See also Figure S6 Table S6.

FIGURE 7: EFFECT OF ACETATE SUPPLEMENTATION ON OXIDATIVE STRESS IN QUIESCENT ECS *IN VIVO* AND *IN VITRO* AND VASCULOPROTECTIVE GENE EXPRESSION IN PEC VS QEC.

(**A**) Intracellular ROS levels (CM-H_2DCFDA fluorescence) of ctrl and CPT1A^{KD} QECs, with or without acetate supplementation, upon exposure to H_2O_2 (50 µM, 2 hr) (n=5; Dll4 induced quiescence model). AU, arbitrary units. (**B,C**) Quantification of $O_2^{\cdot-}$ formation (DHE fluorescence normalized for Hoechst fluorescence) of portal vein (B) and aorta (C) open book preparations in WT or CPT1A$^{\Delta EC}$ mice, at 12 hours after injection with vehicle (PBS) or LPS, with or without acetate treatment (n>10). Dashed horizontal line, value for untreated WT control. (**D**) Quantification of CD45^{+} cells in the lungs of WT and CPT1A$^{\Delta EC}$ mice with or without acetate treatment, 12 hours after injection of LPS (n>10). (**E-H**) qRT-PCR analysis of *NNT* (E) (n=5), *NOS3* (F), *PTGS1* (G) and *GRX* (H) in PECs and contact-inhibited QECs (n=4). Statistics: mixed models statistics (A), ANOVA and Bonferroni post-hoc test (B-D), two-tailed t test with Welch correction (E-H). Data are mean ± SEM; ns, not significant, *p<0.05. See also Figure S7 and Table S7.

STAR METHODS

CONTACT FOR REAGENT AND RESOURCE SHARING

Further information and requests for resources and reagents should be directed to and will be fulfilled by the Lead Contact, Peter Carmeliet (peter.carmeliet@kuleuven.vib.be).

EXPERIMENTAL MODEL AND SUBJECT DETAILS

MICE

Animal housing and all experimental procedures were approved by the Institutional Animal Ethics Committee of the KU Leuven (Belgium). Mice from the EC-specific inducible Cre-driver line Cdh5(PAC)-Cre^{ERT2} (Benedito et al., 2009) were crossed with previously generated *Cpt1a*$^{lox/lox}$ mice (Schoors et al., 2015) to obtain mice with EC-specific deletion of the *Cpt1a* gene upon tamoxifen treatment to induce Cre-mediated gene excision (CPT1A$^{\Delta EC}$ mice). These lines were on a 100% C57Bl/6 background. Tamoxifen (Sigma-Aldrich) treatment was done using 8 week old mice by gavage (0.114 mg/g body weight/day, for 5 consecutive days and an additional day after a 2-day treatment free interval) one week before the experiment.

CELL ISOLATION AND CULTURE

PRIMARY HUMAN UMBILICAL ENDOTHELIAL CELLS: Human umbilical vein endothelial cells (HUVECs) and human umbilical artery endothelial cells (HUAECs) were freshly isolated from umbilical cords obtained from multiple donors (with approval from the Medical Ethical Committee KU Leuven / UZ Leuven and informed consent obtained from all subjects) as previously described (Schoors et al., 2015), regularly tested for mycoplasma. The ECs were maintained in M199 medium (1 mg/mL D-glucose) (ThermoFisher Scientific) supplemented with 20% fetal bovine serum (FBS) (Biochrom BmgH), 2 mM L-glutamine (ThermoFisher Scientific), Endothelial Cell Growth Supplement (ECGS)/ Heparin (PromoCell), 100 IU/mL penicillin and 100 µg/mL streptomycin (ThermoFisher Scientific) or in endothelial cell basal medium (EGM2) (PromoCell) supplemented with endothelial cell growth medium supplement pack (PromoCell). In all experiments, HUVECs and HUAECs were always used as single-donor cultures and were used between passage (p) 1 and 4.

ADULT HUMAN ENDOTHELIAL CELLS: As a source of adult human ECs, we used ECs isolated from healthy adjacent tissue from lung or kidney tumor biopsies. Following surgical resection, adjacent lung or kidney tissue was taken, and transported to the research facility (with approval from the Medical Ethical Committee KU Leuven / UZ Leuven). Upon arrival, samples were rinsed with PBS (ThermoFisher Scientific), minced into smaller pieces of less than 1 mm^3, and transferred to 5 mL digestion medium consisting of Dulbecco's Modified Eagle medium (DMEM) (4500 mg/L glucose) (ThermoFisher Scientific), supplemented with 100 U/mL penicillin/streptomycin (ThermoFisher Scientific), 1 mM sodium pyruvate (ThermoFisher Scientific), MEM NEAAs (1x) (ThermoFisher Scientific), 2 mM glutamine (ThermoFisher Scientific), endothelial cell growth medium supplement pack (PromoCell) and containing 0.2% collagenase I/II (ThermoFisher Scientific), 250 μg/mL DNase (Sigma-Aldrich) and 0.25U/mL Dispase (ThermoFisher Scientific). Samples were incubated for 30 minutes at 37°C, with manual shaking every 5 minutes. Next, 10 mL cold PBS containing BSA 0.1% (Sigma-Aldrich) were added and the samples were filtered using a 100 µm strainer (Corning, NY, USA). Following centrifugation at 300 g at RT for 5 minutes, the supernatant was decanted and discarded. The cell pellet was resuspended in 6 mL of a mix of M199 (containing 10% FBS and sodium pyruvate, MEM NEAAs, glutamine and heparin as above) and EGM2 medium (1:1), further supplemented with antibiotic/antimycotic (2x) (ThermoFisher Scientific). The single cell suspension was plated out in 3 wells of a 6-well plate pre-coated with 0.1% gelatin (Sigma-Aldrich). The next day the medium was changed to EGM2 supplemented with antibiotic/antimycotic (ThermoFisher Scientific) and thereafter refreshed every other day. When reaching confluency and upon detection of EC cell colonies (patches with cobblestone appearance), the ECs were purified using human anti-CD31 coated magnetic beads according to the manufacturer's instructions (MACS Technology, Miltenyi Biotec). The resulting MACS-purified endothelial cells were further cultured in EGM2 medium as single-donor cultures and used for experiments in as early passage as possible (usually up to passage 3-5).

ADULT MOUSE ENDOTHELIAL CELLS: Mouse ECs were isolated from perfused healthy lungs of adult CPT1A$^{\Delta EC}$ mice and their WT littermates. Briefly, before starting the perfusion, the mice were anesthetized with Ketamine/Xylazine (500 µL/mouse of Ketamine 0.65%; Xylazine 0.05% diluted in physiologic saline solution) and once the withdrawal reflex was absent in pelvic limbs, the perfusion procedure was started. Mice were perfused with 5 mL of PBS followed by dissection and dissociation of the lung using the Lung Dissociation Kit according to the manufacturer's instructions (Miltenyi Biotec), at a perfusion rate of 2 mL/minute. Lungs were further dissociated using the gentleMACS dissociator system (MACS Technology, Miltenyi Biotec). Next, samples were centrifuged, resuspended in 5 mL of PBS based wash buffer (containing 0.5% BSA; 2 mM EDTA) and applied to a pre-separation 70 µm filter (Corning, NY, USA). The filtered cells were washed twice with wash buffer and ECs were selected using first CD45 MicroBeads to deplete CD45+ cells and then labelled with CD31 MicroBeads according to the manufacturer's instructions (MACS Technology, Miltenyi Biotec). Positively selected $CD31^+$ cells were stained with viability dye, CD102-APC and CD45-PeCy7 and the fraction of viable, $CD102^+$ and $CD45^-$ cells obtained by FACS sorting was directly collected into TRIzol LS reagent (Thermo Fisher Scientific).

Neonatal mouse (P8) endothelial cells: ECs were isolated from perfused lungs, hearts and livers of P8 mice treated with etomoxir (30 mg/kg; i.p. injection once a day starting 48 hours before euthanization) or vehicle (0.9% NaCl). To obtain a sufficient number of ECs, organs of three P8 mice of each group were pooled. For detection of proliferating cells, 5-ethynyl-2´-deoxyuridine (EdU) (Thermo Fisher Scientific) was injected 2 hours before organ dissection. As described above, mice were anesthetized with Ketamine/Xylazine and the perfusion procedure was started once the withdrawal reflex was absent in pelvic limbs. Mice were perfused with 1 mL of PBS followed by dissection and dissociated with 5 mL of a DMEM based digestion buffer containing either 0.2% collagenase II, 0.2% collagenase IV (lungs, hearts) or 0.1% collagenase I, 0.1% collagenase II (livers), Dispase (0.25 U/mL) (livers and hearts) (ThermoFisher Scientific), 250 µg/mL DNase (Sigma-Aldrich), 2 mM $CaCl_2$, 1% antibiotic/antimycotic, at a perfusion rate of 1 mL/minute. Lungs and hearts were further dissociated using the gentleMACS dissociator system (MACS Technology, Miltenyi Biotec). Next, samples were centrifuged, resuspended in 5 mL of PBS based wash buffer (containing 0.5% BSA; 2 mM EDTA) and applied to a pre-separation 70 µm filter (Corning, NY, USA). The filtered cells were washed twice with wash buffer and ECs were selected using CD45 MicroBeads to deplete CD45+ cells (this step was only applied to lung and heart tissue) and CD31 MicroBeads according to the manufacturer's instructions (MACS Technology, Miltenyi Biotec). Isolated cells were used immediately to assess ROS levels and cell cycle phase as described in detail below (See FLOW CYTOMETRY ANALYSIS: *ANALYSIS OF ENDOTHELIAL SUPEROXIDE LEVELS AND CELL CYCLE IN VIVO)*.

METHOD DETAILS

EC QUIESCENCE MODELS

CONTACT INHIBITION MODEL OF EC QUIESCENCE: ECs (p1 or p2) were seeded in 100% EGM2 at a density of 15,000 cells/cm^2. During the progressive induction of EC-quiescence, the culture medium was gradually changed from 100% EGM2 to M199/EGM2 mix in ratio 1:1 (further referred to as growth medium). To generate the corresponding proliferative control, contact inhibited cells (day 6 QECs) were trypsinized (using Trypsin-EDTA (0.25%); ThermoFisher Scientific) and cultured in growth medium for at least 36 hours to re-initiate proliferation. PECs, used as proliferating controls for contact-inhibited QECs are always reseeded QECs.

DLL4 STIMULATION MODEL OF EC QUIESCENCE: Culture plates were coated overnight at 4°C on a plate shaker with 1 µg/mL recombinant human Delta like ligand4 (rhDll4, R&D Systems) with 0.1% gelatin. The control plates were coated with 0.1% gelatin supplemented with 0.02% BSA (Sigma-Aldrich), which was used as a carrier for Dll4. Prior to EC seeding, excessive coating solution was removed by aspiration and ECs were seeded at a density of 30,000 cells/cm^2 in growth medium. Experiments were performed 24 hours after seeding. PECs, used as proliferating controls for Dll4-induced QECs are always ECs grown in parallel on BSA coated plates.

LAMINAR SHEAR STRESS MODEL OF EC QUIESCENCE: ECs were seeded at a density of 30,000 cells/cm2 in growth medium on SuperFrost Excell object slides (Thermo Scientific Menzel) overnight and exposed to laminar shear stress (10 dynes/cm^2) for 24 hours. The parallel-plate flow chamber system was built in-house and combined with a peristaltic pump (COLE-PARMER INSTRUMENT 7519-06 Masterflex L/S Cartridge Pump Head, 8-Channel, 4-Roller). HUVECs seeded on SuperFrost object slides overnight were used as static controls.

KNOCK-DOWN AND OVEREXPRESSION STRATEGIES

LENTIVIRAL TRANSDUCTIONS: For overexpression of the Notch intracellular domain (V5-NICD; gift from M. Potente), the cDNA was cloned in the pRRLsinPPT.CMV.MCS MM W prevector (Wong et al., 2017). To generate shRNA vectors against CPT1A, ACSS1, IDH2, ME3, ACADvl and HADHB oligonucleotides were cloned into the pLKO-shRNA2 vector (Clontech). A nonsense scrambled shRNA sequence was used as a negative control. Oligonucleotides are listed in the Key Resources Table. Production of lentiviruses by transfection into 293T cells was performed as described (Wong et al., 2017). For transductions, a multiplicity of infection (MOI) of 5 was used for all shIDH2 experiments, 10 was used for all shME3, shACADvl and shHADHB experiments, 20 was used in all shCPT1A, shACSS1 experiments. For transductions with NICD, a MOI of 10 was used. Cells were transduced overnight and re-fed with fresh medium the next day. Transduced cells were used in functional assays at least 3 to 4 days post-transduction.

TRANSCRIPTOMIC ANALYSIS

MICROARRAY ANALYSIS: RNA from PECs and contact-inhibited QECs was extracted, reverse transcribed into cDNA, biotin-UTP labelled using the Illumina TotalPrep RNA Amplification kit (ThermoFisher Scientific) and hybridized to the Illumina HumanHT-12 v4 Expression BeadChip for microarray analysis using standard protocols (Illumina). Differentially expressed genes and their false discovery rate (FDR) corrected p-values were identified by the limma package (Cantelmo et al., 2016). Heatmap analysis was performed using the D3heatmap package, and significant clusters were calculated via multiscale bootstrap analysis with the Pvclust package (Cantelmo et al., 2016). The rotation gene set (ROAST) algorithm as implemented in the limma package was used to perform self-contained gene set analysis. Gene expression data were mapped on KEGG metabolic pathways using Pathview (Cantelmo et al., 2016). Microarray data are available in GEO (www.ncbi.nlm.nih.gov/geo/) under accession GSE89174.

RNA-SEQUENCING: RNA from freshly isolated murine lung ECs was prepared using TRIzol reagent according to the manufacturer’s instruction. Starting from 1 µg total RNA, poly-adenylated fragments were isolated, reverse transcribed and converted into indexed sequencing libraries using the KAPA stranded mRNA-seq kit (Sopachem, Eke, Belgium). The first 50 bases of these libraries were sequenced on a HiSeq 4000 system (Illumina, San Diego, CA). The raw sequenced reads were mapped to the mouse reference transcriptome and genome (GRCm38/mm10) using the Bowtie TopHat pipeline. Mapped reads were assigned to Ensembl gene IDs by HTSeq, resulting in on average 14,814,487 ± 5,948,836 counts per sample. Genes expressed at a level of at least 1 count per million reads in at least three of eight samples were filtered out with the EdgeR package (Cantelmo et al., 2016), and differentially expressed genes and their false discovery rate (FDR) corrected p-values were identified using Limma (Cantelmo et al., 2016). Heatmap analysis was performed using the D3heatmap package and significant clusters were calculated via multiscale bootstrap analysis with the Pvclust package (Cantelmo et al., 2016). The rotation gene set (ROAST) algorithm as implemented in the Limma package (Cantelmo et al., 2016) was used to perform self-contained gene set analysis. Gene expression data were mapped on KEGG metabolic pathways using Pathview. RNA-sequencing data are available in GEO (https://www.ncbi.nlm.nih.gov/geo/) under accession E-MTAB-6595.

RNA ISOLATION AND QUANTITATIVE RT-PCR

RNA was collected and purified using the PureLink® RNA Mini Kit (ThermoFisher Scientific) and converted to cDNA using the iScript cDNA synthesis kit (Bio-Rad). For RNA-sequencing validation, RNA from isolated ECs was collected into TRIzol Reagent and extracted and, then, converted to cDNA using the SuperScript™ III Reverse Transcriptase (ThermoFisher Scientific). RNA expression analysis was performed by Taqman quantitative RT-PCR (ThermoFisher Scientific) as described using premade primer sets (IDT) (Schoors et al., 2015). Premade primer set ID numbers are listed in the Key Resources Table. For comparison of gene expression between conditions, expression (normalized to HPRT endogenous control) is expressed relative to control condition.

IMMUNOBLOT ANALYSIS

Protein extraction and immunoblot analysis were performed using a modified Laemmli sample buffer (125 mM Tris-HCl, pH 6.8 buffer containing 2% SDS and 10% glycerol) or cell lysis buffer (Cell Signaling Technology) in the presence of protease and phosphatase inhibitors (Roche). Lysates were separated by SDS-PAGE under reducing conditions, transferred to a nitrocellulose or PVDF membrane, and analyzed by immunoblotting. Primary antibodies used were rabbit anti-CPT1A (Cell Signaling Technology), anti-total AMPKα (Cell Signaling Technology), rabbit anti-phospho-AMPKα Thr172 (Cell Signaling Technology), anti-PFKFB3 (Cell Signaling Technology), anti-NICD (Cell Signaling Technology), anti-Histone H2A (Cell Signaling Technology), anti-Acetyl-Histone H2A (Lys5) (Cell Signaling Technology), anti-Histone H3 (Cell Signaling Technology), anti-Acetyl-Histone H3 (Lys9) (Cell

Signaling Technology), anti-Histone H4 (Cell Signaling Technology), anti-Acetyl-Histone H4 (Lys8) (Cell Signaling Technology), anti-α-tubulin (Sigma) and anti-acetyllysine (PTM-Biolab). Appropriate secondary antibodies were from Cell Signaling Technology. Signal was detected using the ECL or Femto system (ThermoFisher Scientific) according to the manufacturer's instructions. Densitometric quantifications of bands were done with Fiji software (https://fiji.sc).

HISTONE EXTRACTION: ECs were washed with cold PBS, scraped and collected in cold hypotonic lysis buffer (10 mM Tris-HCL (pH 7.5), 1 mM KCl, 1.5 mM $MgCl_2$, to which was freshly added: 1 mM DTT, 1× protease inhibitors, 10 mM sodium butyrate (Sigma-Aldrich), 0.1% IGEPAL (an NP-40 substitute; Sigma-Aldrich), 1 μM trichostatin A (TSA; Sigma-Aldrich). The collected samples were incubated for 30 minutes on a rotator at 4°C to promote hypotonic swelling of cells and lysis by mechanical shearing during rotation. Nuclei were pelleted at 15,000 rpm for 5 minutes at 4 °C and immediately resuspended in 0.4 N H_2SO_4 followed by incubation overnight at 4 °C. After centrifugation at 15,000 rpm for 10 minutes at 4 °C, histones were precipitated from the supernatant by addition of 20% trichloroacetic acid for 2 hours, followed by centrifugation at 15,000 rpm for 10 minutes at 4 °C. Pellets were washed twice with acetone. Histone proteins were resuspended in H_2O and used for immunoblot analysis.

FLOW CYTOMETRY ANALYSIS

IN VIVO ANALYSIS OF ENDOTHELIAL SUPEROXIDE LEVELS AND CELL CYCLE: We developed a new FACS-based method to measure ROS levels and subsequently proliferation of ECs freshly isolated from different organs (heart, liver, lung) of P8 neonatal mice, in which blood vessels are still growing and expanding (thus containing PECs) but also already contain QECs. Because of technical reasons, we first had to stain and sort for the ROS marker dehydroethidium (DHE) and thereafter for EdU as described below. This avoided that when first stained for EdU, the DHE signal was completely lost due to the fixation and permeabilisation treatment required for the EdU nuclear staining. *Detection of superoxide levels in freshly isolated murine ECs:* Briefly, freshly isolated ECs from lungs, hearts and livers of P8 neonatal mice (as described above) were stained with viability dye, CD45-PeCy7, CD102-APC and DHE (20 μmol/L; ThermoFisher Scientific) at 4°C for 30 minutes. Next, based on DHE staining we FACS sorted viable, $CD45^-$, $CD102^+$ and DHE^+ ECs and viable, $CD45^-$, $CD102^+$ and DHE^- ECs separately into two Eppendorf tubes. The cells were then immediately processed and stained for EdU as described below. *Cell cycle analysis in freshly isolated murine ECs:* Cells in G1 were identified as a population positive for EdU incorporation. Briefly, the DHE^+ and DHE^- FACS sorted ECs from lungs, hearts and livers of EdU treated P8 mice were fixed with 4% PFA (15 minutes at RT). The incorporated EdU was detected by a 'click-It reaction' with Alexa Fluor 488 according to the manufacturer's instructions (ThermoFisher Scientific). Data were recorded by flow cytometry, and analyzed with the FlowJo 8.8.6 software (https://www.flowjo.com).

CELL CYCLE ANALYSIS IN VITRO: Cells in G0 were identified as a 2N DNA population lacking EdU incorporation. Briefly, cells were labeled with 10 µM EdU over 24 hours, collected by trypsinization and fixed (4% PFA). The incorporated EdU was detected by a 'click-It reaction' with Alexa Fluor 647 according to the manufacturer's instructions (ThermoFisher Scientific). Data were recorded by flow cytometry, and resultant data were analyzed with the FlowJo 8.8.6 software (https://www.flowjo.com).

METABOLIC ASSAYS

FATTY ACID OXIDATION: ECs were incubated in fully supplemented growth medium, supplemented with 100 µM unlabeled palmitate and 50 µM carnitine (Sigma-Aldrich). Cells were incubated for 6 hours in growth medium containing 2 µCi/mL [9,10-^{3}H]-palmitate (Schoors et al., 2015; Wong et al., 2017) (Perkin Elmer). Thereafter, supernatant was transferred into glass vials sealed with rubber stoppers. ^3H_2O was captured in hanging wells containing a Whatman paper soaked with H_2O over a period of 48 hours at 37°C to reach saturation (Schoors et al., 2015). Radioactivity was determined by liquid scintillation counting.

GLYCOLYSIS: Glycolysis was measured analogously to fatty acid oxidation (see above) using 80 mCi/mmol [5-^{3}H]-D-glucose (Perkin Elmer) (Schoors et al., 2015).

FATTY ACID SYNTHESIS: ECs were incubated in growth medium supplemented with [U-^{14}C]-acetate (Perkin Elmer) for 24 hours following snap freezing and methanol-water-chloroform extraction. Phase separation was achieved by centrifugation at 4˚C and the methanol-water phase containing polar metabolites was used as negative control. Chloroform phase containing fatty acids was added to scintillation liquid and counts were normalized to protein concentrations determined of the dried protein interphase.

^{14}C-GLUCOSE OXIDATION: Cells were incubated for 6 hours in growth medium containing 100 µCi/mmol [6-^{14}C]-D-glucose (Perkin Elmer). Thereafter, 250µL of 2 M perchloric acid was added to each well to stop cellular metabolism and wells were immediately covered with a 1x hyamine hydroxide-saturated Whatman paper. Overnight absorption of $^{14}CO_2$ released during oxidation of glucose into the paper was performed at room temperature, and radioactivity in the paper was determined by liquid scintillation counting.

^{14}C-GLUTAMINE OXIDATION: was performed similarly as glucose oxidation, except that 0.5 µCi/mL [U-^{14}C]-glutamine (Perkin Elmer) as tracer was used.

OXIDATIVE PENTOSE PHOSPHATE PATHWAY: The oxidative pentose phosphate pathway (oxPPP) flux was measured as $^{14}CO_2$ formation using [6-^{14}C]-D-glucose (Hartmann Analytic) ($^{14}CO_2$ formation only in the TCA cycle) and [1-^{14}C]-D-glucose (Hartmann Analytic) ($^{14}CO_2$ formation in both the TCA cycle and the oxPPP). Cells were incubated in parallel in medium containing [6-^{14}C]-D-glucose (1 µCi/mmol) or medium containing [1-^{14}C]-D-glucose (1 µCi/mmol). Released $^{14}CO_2$ was captured in a similar manner as described above for the glucose or glutamine oxidation. The oxPPP flux was then calculated by subtracting the [6-^{14}C]-D-glucose flux from the [1-^{14}C]-D-glucose flux and was normalized to the glycolytic flux to correct for total cellular glucose usage.

PALMITATE MEDIATED DNA, RNA AND PROTEIN SYNTHESIS: was measured by the incorporation of ^{14}C into DNA, RNA or protein using 100 µCi/mmol [U-^{14}C]- palmitic acid (Perkin Elmer) and was corrected for the total amount of DNA/RNA per sample. Total DNA/RNA was extracted using TRIzol® Reagent as an alternative extraction method for DNA and RNA.

ATP MEASUREMENT: Analysis of total ATP levels was performed using a commercially available kit (ATPlite™, PerkinElmer).

OXYGEN CONSUMPTION: Cells were seeded at 30,000 cells per well on Seahorse XF24 tissue culture plates (Seahorse Bioscience Europe). The oxygen consumption was measured over a period of 2 minutes. At any condition, 5 consecutive measurements of OCR are done. After OCR measurement at baseline conditions, oligomycin, a blocker of ATP synthase is injected at 12 µM (final concentration in the cell 1.2 µM) to assess OCR_{ATP}.

DETECTION OF GLUTATHIONE SPECIES, NADPH AND DNTPS: Metabolites from ECs grown on a 6 well plate were extracted in 300 µL of a 50:30:20 (methanol: acetonitrile: 20 mM Tris, pH 9.3) extraction buffer**.** Extraction samples were then centrifuged for 5 minutes at 15,000 x G and the supernatant was transferred to LC-MS vials. Targeted measurements of GSSG, GSH, $NADP^+$, NADPH, dATP, dTTP and dCTP were performed using a Dionex UltiMate 3000 LC System (Thermo Scientific) coupled to a Q Exactive Orbitrap mass spectrometer (Thermo Scientific) operated in negative mode. Practically, 35 µL of sample was injected on a SeQuant ZIC/ pHILIC Polymeric column (Merck Millipore). The gradient started with 20% of solvent B (10 mM NH_4-acetate in MQH_2O, pH 9.3) and 80% solvent A (LC-MS grade acetonitrile) and remained at 20% B until 2 minutes post injection. Next, a linear gradient to 80% B was carried out until 29 minutes. At 38 minutes the gradient returned to 40% B followed by a decrease to 20% B at 42 minutes. The chromatography was stopped at 58 minutes. The flow was kept constant at 100 µl per minutes at the column was placed at 25 °C throughout the analysis. The MS was operated both in targeted MS2 mode using a spray voltage of 3.5 kV, capillary temperature of 320 °C, sheath gas at 10.0, auxiliary gas at 5.0. For the targeted MS2 mode, AGC was set at 2e5, maximum IT at 100 ms, a resolution of 17.500 and an isolation window of 1.2 m/z. Data collection was performed using *Xcalibur* software (ThermoFisher Scientific).

GLUCOSE CONSUMPTION: Cells were incubated for 24 hours in growth medium. To 20 µl of medium 80 µl of 100% methanol was added and kept for 3 hours at -80 °C in order to precipitate proteins. Following a centrifugation at 20,000 x g for 10 minutes, the supernatant was dried using a vacuum centrifuge. To the dried fraction, 50 µl of hydroxylamine hydrochloride solution (20 mg/mL in pyridine) was added. The samples were heated at 90 °C for 60 minutes, followed by the addition of 100 µL of propionic anhydride. After 30 minutes incubation at 60 °C, the samples were again evaporated to dryness and dissolved in 100 µL of ethyl acetate and transferred into GC vials for GC–MS analysis. The injection volume was 1 µL and samples were injected using a 1:20 split ratio. GC oven temperature was held at 80 °C for 1 minute, increased to 280 °C at 20 °C per minute, and held for 3 minutes. The mass spectrometer operated in SIM mode and glucose was determined from the fragment at m/z 370 ($C_{17}H_{24}O_8N_1$), which contains carbon atoms C1–C5 of glucose. Data collection was performed using *Xcalibur* software.

ENERGY BALANCE ASSESSMENT: Samples were collected in 300 µl cold (chilled on dry ice) 50:30:20 (methanol: acetonitrile: 20 mM Tris, pH 9.3) extraction buffer and 100 µl of the mixture was injected onto an Agilent 1260 HPLC equipped with a C18-Symmetry column (150 x 4.6 mm; 5 µm) (Waters), thermostatted at 22.5 °C. Flow rate was kept constant at 1 mL per minute. A linear gradient using solvent A (50 mM NaH_2PO4, 4 mM tetrabutylammonium, adjusted to pH 5.0 using H_2SO4) and solvent B (50 mM NaH_2PO4, 4 mM tetrabutylammonium, 30% CH_3CN, adjusted to pH 5.0 using H_2SO4) was accomplished as follows: 95% A for 2 minutes, from 2 to 25 minutes linear increase to 100% B, from 25 to 27 minutes isocratic at 100% B, from 27 to 29 minutes linear gradient to 95% A and finally from 29 to 35 minutes at 95% A. Detection of ATP, ADP and AMP occurred at 259 nm. The energy charge was calculated using the following equation:

$$\text{Energy charge} = \frac{[\text{ATP}] + \frac{1}{2}[\text{ADP}]}{[\text{ATP}] + [\text{ADP}] + [\text{AMP}]}$$

^{13}C TRACER EXPERIMENTS AND METABOLITE LEVELS

For ^{13}C-carbon incorporation from palmitate in metabolites, cells were incubated for 48 hours with labeled substrates. For ECs, [U-^{13}C]-palmitate, [U-^{13}C]-glucose, [U-^{13}C]-glutamine, [U-^{13}C]-acetate labeling was done in the setting of 100% labeling, whereby all cold metabolites in growth medium were replaced by 100 µM [U-^{13}C]-palmitate, 5.5 mM [U-^{13}C]-glucose, 2 mM [U-^{13}C]-glutamine (Cambridge isotope laboratories) or 500 µM [U-^{13}C]-acetate (Sigma-Aldrich) respectively. For palmitate labelling charcoal stripped serum (which does not contain any fatty acids) was used in growth medium (Sigma-Aldrich). Metabolites for the subsequent mass spectrometry analysis were prepared by quenching the cells in liquid nitrogen followed by a cold two-phase methanol-water-chloroform extraction (Schoors et al., 2015). Phase separation was achieved by centrifugation at 4˚C and the methanol-water phase containing polar metabolites was separated and dried using a vacuum concentrator. The dried metabolite samples were stored at -80˚C (Schoors et al., 2015). Polar metabolites were derivatized for 90 minutes at 37°C with 7.5 µL of 20 mg/mL methoxyamine in pyridine and subsequently for 60 minutes at 60°C with 15 µL of N-(tert-butyldimethylsilyl)-N-methyl-trifluoroacetamide, with 1% tert-butyldimethyl-chlorosilane (Schoors et al., 2015). Isotopomer distributions and metabolite levels were measured with a 7890A GC system (Agilent Technologies) combined with a 5975C Inert MS system (Agilent Technologies). One microliter of sample was injected onto a DB35MS column in splitless mode using an inlet temperature of 270˚C (Schoors et al., 2015). The carrier gas was helium with a flow rate of 1 mL per minute. Upon injection, the GC oven was held at 100˚C for 3 minutes and then ramped to 300˚C with a gradient of 2.5˚C per minute. The MS system was operated under electron impact ionization at 70 eV and a mass range of 100–650 amu was scanned. Isotopomer distributions were extracted from the raw ion chromatograms using a custom Matlab M-file, which applies consistent integration bounds and baseline correction to each ion. In addition, we corrected for naturally occurring isotopes using the method of Fernandez et al (Fernandez et al., 1996). For relative metabolite levels, the total ion count was normalized to the internal standards norvaline and glutarate and to the protein content. To correct for enrichment dilution, we used previously reported methods, i.e. we divided the fractional contribution of a labeled metabolite of interest by the fractional contribution of its precursor. The total contribution of carbon was calculated using the following equation:

$$\text{Total contribution of carbon} = \sum_{i=0}^{n} i * m_i \,/ \left(n * \sum_{i=0}^{n} m_i\right)$$

Herewith, “n” is the number of C atoms in the metabolite, “i” represents the different mass isotopomers and “m” refers to the abundance of a certain mass. Glycolytic carbon contribution was calculated based on [U-^{13}C]-glucose labeling and label dilution in pyruvate . For total metabolite levels, arbitrary units of the metabolite of interest were normalized to the protein content.

PC-dependent anaplerosis was estimated from the difference of m+3 malate and m+3 succinate using [U-^{13}C]-glucose, as described previously (Christen et al., 2016). Briefly, malate m+3 from [U-^{13}C]-glucose is generated by PC flux, but can also arise from an oxidative TCA cycle flux. Succinate m+3 from [U-^{13}C]-glucose can arise from an oxidative TCA cycle flux, but not from PC flux (given that reverse succinate dehydrogenase flux is marginal or not present). Thus, under the prerequisite that pyruvate enrichment from [U-^{13}C]-glucose is similar, comparing malate m+3 and succinate m+3 allows to conclude about relative changes of PC-dependent anaplerosis.

IN VITRO FUNCTIONAL ASSAYS

PROLIFERATION: EC Proliferation was quantified by incubating cells for 2 hours with 1 µCi/mL [3H]-thymidine (Perkin Elmer). Thereafter, cells were fixed with 100% ethanol for 15 minutes at 4°C, precipitated with 10% TCA and lysed with 0.1 N NaOH. The amount of [^{3}H]-thymidine incorporated into DNA was measured by scintillation counting.

LDH VIABILITY ASSAY: Cell survival was assessed by lactate dehydrogenase (LDH) release into the media using the LDH assay kit (Roche) as indicated in manufacturer's specifications, whereby low LDH release signifies low cell death and high survival. 1.2 µM oligomycin (Sigma-Aldrich) was used to verify whether pharmacological targeting of ATP can affect viability of ECs upon induction of quiescence and or CPT1A^{KD}.

TRANS-ENDOTHELIAL ELECTRICAL RESISTANCE: 25,000 ECs were seeded in growth medium on 6.5 mm 0.1% gelatin-coated polyester transwells, 0.4 µm pore size (Costar ref. 3470, Sigma-Aldrich). The trans-endothelial electrical resistance (TEER) was measured using the Endohm-6 electrode (World Precisions Instruments) connected to an EVOM2 voltohmmeter (World Precisions Instruments). Gelatin-coated wells without cells were used to measure the intrinsic electrical resistance of the inserts and these values were then subtracted to the values measured in the presence of cells. Measurements were performed every day, taking at least 2 measurements per treatment. Overnight incubation with etomoxir (100 µM) and trimetazidine (TMZ) (250 µM; Sigma-Aldrich) was used to assess the effect of pharmacological FAO inhibition, LPS (1 µg/mL) (Escherichia coli, 0111:B4, Sigma-Aldrich) was used to assess the effect of the stressors, hydroxycitrate (HCA) (1mM; Sigma-Aldrich) was used to assess the inhibition of ATP-dependent citrate lyase. The mitochondrial ROS scavenger MitoTEMPO (Sigma-Aldrich) was used with a concentration of 5 µM.

LEUKOCYTE ADHESION ASSAY: Whole blood from healthy human volunteers was collected (with approval from the Medical Ethical Committee KU Leuven / UZ Leuven and informed consent obtained from all subjects) and anticoagulated with K_2EDTA (1.8 mg/mL, using plastic whole blood spray-coated K_2EDTA tubes, Bection Dickinson). Peripheral blood mononuclear cell (PBMC) were isolated by gradient centrifugation over Ficoll-paque plus (GE healthcare). PBMCs were labelled with Calcein (cell-permeant dye, ThermoFisher Scientific). HUVECS (plated 7 days before (7.5 x 10^4 cells/well, 12-wells plate), were washed with PBS and incubated either with vehicle (sterile PBS), etomoxir (100 µM) or LPS (1 µg/mL) overnight (37°C, 5% CO_2). After this period, medium was removed and ECs were washed with PBS. The mononuclear cells were added (5 x 10^5/well) and incubated for 60 minutes (37°C, 5% CO_2). Non-adherent cells were removed by washing 5 times with PBS and cells where fixed using 4% PFA. Five fields per well, randomly chosen, were analyzed and the number of adherent leukocytes per field was determined using a Leica DMI6000B microscope (magnification 20X).

ANALYSIS OF ROS SPECIES

INTRACELLULAR ROS ANALYSIS: Intracellular ROS levels were measured using 5-(and-6)-chloromethyl-2′,7′-dichlorodihydrofluorescein diacetate, acetyl ester (CM-H2DCFDA) according to the manufacturer's instructions (ThermoFisher Scientific). CM-H2DCFDA is metabolized by intracellular esterases to a non-fluorescent molecule, which is oxidized by H_2O_2 to the fluorescence product CM-DCF. The intracellular ROS levels were determined by pre-incubation of the ECs for 30 minutes with 10 µM CM-H_2DCFDA and H_2O_2 scavenging capacity was determined after a subsequent incubation for 0-2 hours with 50 µM H_2O_2 (Merck, Milipore) in serum free M199. The mitochondrial ROS scavenger MitoTEMPO (Sigma-Aldrich) was used with a concentration of 5 µM. The fluorescent intensity was measured according to the manufacturer's instructions.

MITOCHONDRIAL ROS ANALYSIS VIA MITOSOX™: Intracellular accumulation of superoxide was estimated using MitoSOX™ Red (ThermoFisher Scientific), which is selectively targeted to the mitochondria, where it is oxidized by superoxide and exhibits red fluorescence upon binding to nucleic acids. Cells were loaded with MitoSOX™ at 2.5 µM for 30 minutes, collected by trypsinization and washed with PBS supplemented with 2% FBS. Using a flow cytometer, MitoSOX Red was excited at 488 nm and fluorescence emission at 575 nm was measured. Fluorescence intensity was used as measurement of mitochondrial superoxide production and the data were analyzed with the FlowJo 8.8.6 software.

TOTAL LEVELS OF H_2O_2: Total levels of H_2O_2 were measured by using the Amplex® Red Hydrogen Peroxide/Peroxidase Assay Kit (ThermoFisher Scientific), according to the manufacturer's instructions.

MITOCHONDRIAL LEVELS OF H_2O_2: Measurements of the mitochondrial levels of H_2O_2 were performed using the HyPER-dMito probe (Evrogen) as previously described (Belousov et al., 2006). Briefly, ECs were transduced overnight with HyPER-dMito (cloned in the pRRLsinPPT.CMV.MCS MM W prevector) and re-fed with fresh medium the next day. Transduced cells were used for confocal imaging using a Zeiss LSM 780 confocal microscope (oil objective: x40) (Carl Zeiss) and were treated with or without 50 µM H_2O_2 for 10 minutes. Cells were placed in the microscope stage incubator and HyPER-dMito fluorescence was activated by 488 nm or 405 nm laser. Band pass 530/40 emission filter was used in both cases. For each condition 10 independent images were taken. To assess mitochondrial levels of H_2O_2, the ratio of fluorescence intensity upon excitation at 488nm over fluorescence intensity upon excitation at 405 nm (ratio 488/405 nm) was calculated.

OH° DETECTION BY ELECTRON PARAMAGNETIC RESONANCE (EPR) SPECTROSCOPY: Quiescent (QEC) or proliferating cells (PEC) were washed twice with PBS and incubated for 3-5 minutes with trypsin/EDTA at 37 °C. Harvested cells were centrifuged for 5 minutes at 1,200 rpm, washed with DPBS, and resuspended in PBS at a concentration of $2x10^6$ cells/mL. Spin trapping reagents 5-diisopropoxyphosphoryl-5-methyl-1-pyrroline N-oxide (DIPPMO, final concentration 50 mM) (Enzo Life Science) and diethylenetriaminepentaacetic acid (DTPA, final concentration 1 mM) (Sigma-Aldrich) were added and the solution was transferred to a flat quartz cell for the EPR measurements. This ensured reproducible measurement as the whole resonator was filled with the same volume of material. For measurement on lysates, cells were lysed by sonication (20s, Labsonic U, B. Braun).
For control experiments with superoxide dismutase-polyethylene glycol (SOD-PEG, final concentration 200 U/mL) (Sigma-Aldrich) or catalase-peg (CAT-PEG, final concentration 100 U/mL) (Sigma-Aldrich), cells were preincubated for 30 minutes (37°C) with the appropriate enzyme before adding the spin trap reagents. EPR measurements were performed using a Bruker EMX-Plus spectrometer (Bruker, Rheinstetten, Germany), operating in X-band (9.85 GHz) and equipped with

a SHQ high- sensitivity resonator. Settings used were as follows: microwave power: 20 mW; modulation frequency: 100 kHz; modulation amplitude: 0.1 mT (lysate) or 0.2 mT (cells); receiver gain: 60 dB; time constant: 10.24 ms; conversion time, 50.04 ms; data points, 1024; sweep width, 20 mT; number of scan: 15. Computer simulations were performed using Winsim from the Public Electron Paramagnetic Resonance Software Tools library of the NIH (USA).

IMMUNOCHEMISTRY AND MORPHOMETRY

QUANTIFICATION OF VE-CADHERIN JUNCTIONS: Cells were fixed with 4% PFA for 10 minutes at room temperature and subjected to immunofluorescence staining for adherence junctions using anti-VE-cadherin (ThermoFisher Scientific) and Alexa-488 Fluor conjugated phalloidin (ThermoFisher Scientific). Alexa-568 or -647 conjugated secondary antibodies were used (ThermoFisher Scientific). Imaging was performed using a Zeiss LSM 780 confocal microscope (oil objectives: x40 NA 1.3, x63 NA 1.4, x100 NA 1.46) (Carl Zeiss). Junctional length was calculated by measuring the length of all segments of continuous and discontinuous junctions on confluent ECs stained for VE-cadherin as described (Cantelmo et al., 2016). The sum of all segments was considered the total junctional length (100%), and the sum of all discontinuous segments was calculated as the percentage of total junctional length. A minimum of 5 fields was quantified (≈30 cells per field) per experiment.

β-GALACTOSIDASE SENESCENCE STAINING: Staining was performed as previously described (Debacq-Chainiaux et al., 2009). Briefly, The EC cultures were fixed for 5 minutes at room temperature with fixation solution (2% formaldehyde (vol/vol) and 0.2% glutaraldehyde (vol/vol) in PBS) followed by overnight incubation with the staining solution (40 mM citric acid/Na phosphate buffer, 5 mM $K_4[Fe(CN)_6]$, 5 mM $K_3[Fe(CN)_6]$, 150 mM sodium chloride, 2 mM magnesium chloride) and 1 mg/mL X-gal (ThermoFisher Scientific) in distilled H_2O. Cells were rinsed twice with PBS and once with

100% methanol. The stained cell culture plates were protected from the light and air-dried. The β-galactosidase staining was imaged using phase-contrast microscopy.

PCR CHROMATIN IMMUNOPRECIPITATION

Cultured cells, treated or not with the Notch inhibitor N-[N-(3,5-difluorophenacetyl)-L-alanyl]-S-phenylglycine t-butyl ester (DAPT; 10 µM) (Sigma-Aldrich) overnight, were fixed with 1% formaldehyde (16% formaldehyde (w/v), Methanol-free, ThermoFisher Scientific) for 8 minutes. Glycine (125 µM) was added for 5 minutes. Cells were washed twice with ice-cold PBS 0.5% Triton-X100, scraped and collected by centrifugation (1,000 × g for 5 minutes at 4°C). The pellet was resuspended in 1,400 µl of modified RIPA buffer (50 mM Tris-HCl pH 8, 150 mM NaCl, 2 mM EDTA pH 8,1% Triton-X100, 0.5% Sodium deoxycholate, 1% SDS, 1% protease inhibitors). The lysate was sonicated for 4 minutes by using a 250 Digital Sonifier (Branson) with 0.7s 'On' and 1.3s 'Off' pulses at 40% power amplitude, yielding a DNA fragments between 100 and 1,000 bp. The lysate was centrifuged for 10 minutes at 16,000 × G (4°C), and supernatant transferred to a new eppendorf tube. 50 µl of sheared chromatin was set apart as “input”, and 5 µg of either rat anti-Notch1 (Cell Signaling Technology) or mouse anti-V5 tag (ThermoFisher Scientific) were added to the remainder of the chromatin. Samples were incubated overnight at 4 °C on a rotator. 20 µl Pierce Protein A/G Magnetic Beads (ThermoFisher Scientific) were added to the samples and incubated at 4°C for at least 5 hours. A/G Magnetic Beads were collected and washed 5 times with washing buffer (50 mM Tris-HCl, 200 mM LiCl, 2 mM EDTA, pH 8, 1% Triton, 0.5% Sodium deoxycholate, 0.1% SDS, 1% protease inhibitors), and twice with TE buffer. The A/G magnetic beads were resuspended in 50 µl of TE buffer, and 1.5 µl of RNase A (ThermoFisher Scientific) was added to the A/G beads samples and to the input, followed by incubation for 30 minutes at 37°C. After addition of 1.5 µl of proteinase K (ThermoFisher Scientific) and overnight incubation at 65°C in a thermoshaker (800 rpm), the DNA was purified using 1.8 × volume of Agencourt AMPure XP (Beckman Coulter) according to the manufacturer’s specifications, and eluted in 20 µl of TE buffer (ThermoFisher Scientific). The input, control IgG and immunoprecipitated DNA fractions were then subjected to quantitative PCR using SYBR Green (PowerUp™ SYBR™ Green, ThermoFisher Scientific). Primer sequences are listed in the Key Resources Table. Raw Ct values were analyzed and results were presented as % of input.

LUCIFERASE REPORTER ASSAY

Sequences verified by PCR were cloned into the pGL3 basic luciferase plasmid (Promega) lacking promoter and enhancer elements. HUVECs were transduced with control lentiviruses or NICD^{OE} lentiviruses. Four days after viral transduction, cells were trypsinized and transfected with empty pGL3 plasmids or plasmids containing sequences of the *CPT1A* promoter, as identified by chromatin immunoprecipitation (ChIP)-qPCR, using Nucleofector transfection reagent (Lonza), as per manufacturer's specifications. Cells were co-transfected with the respective luciferase reporters and also the Renilla plasmid, as a control, and allowed to grow for 72 hours before being collected with PBS, centrifuged, then lysed. Luciferase activity was measured by Dual Luciferase Reporter Kit (Promega) according to the manufacturer's specifications.

MOUSE STUDIES

IN SITU DETECTION OF ECS SUPEROXIDE LEVELS: Aortas and portal veins were harvested from the animals at 4 or 12 hours after LPS injection (10 mg/kg, i.p.) and treated i.p. with 400 µL vehicle or 0.5 M sodium acetate (Sigma-Aldrich) solution daily, were opened longitudinally for en-face dehydroethidium (DHE; ThermoFisher Scientific) staining. DHE (20 µmol/l) was topically applied to the samples and incubated in a light-protected humidified chamber at 37°C for 30 minutes followed by Hoechst33342 (1 µg/mL; ThermoFisher Scientific) staining for 15 minutes and finally Alexa-647 conjugated isolectin B4 (ThermoFisher Scientific) for 1 hour. Imaging was performed immediately using a Zeiss LSM 780 confocal microscope (oil objective: x40 NA 1.3) (Carl Zeiss). The endothelium was identified by an isolectin B4 positive signal. For all images in a single experiment, the samples were all stained at the same time, and acquisition settings were kept constant for all image acquisitions. Quantification of DHE fluorescence intensity was performed using Fiji software. Average intensity images were generated and ECs nuclei were selected using the particle-analyzer tool. Per sample, 5 images were analyzed and corrected total cell fluorescence was calculated for DHE.

DETERMINATION OF CYTOKINE CONCENTRATIONS: Levels of cytokines were measured in blood serum of LPS treated CPT1A$^{\Delta EC}$ mice and their WT littermates using MACSPlex Cytokine Kit according to the manufacturer's instructions (mouse, Miltenyi Biotec).

LEUKOCYTE INFILTRATION INTO THE LUNGS: Lungs were dissected and fixed in 4% PFA overnight at 4°C, dehydrated, embedded in paraffin and sectioned. Immunostaining of leukocytes was done with rat anti-Mouse CD45 antibody (BD Pharmingen). The sections were then incubated with an appropriate secondary antibody (Jackson Immuno Research) and TSA Cy3 amplification (Perkin Elmer). Nuclei were counterstained with Hoechst33342. Imaging was performed using a Leica DMI6000B inverted microscope (Leica Microsystems). Morphometric analysis of the CD45$^+$ area in % of lung area was done using Leica MM AF powered by MetaMorph analysis software.

DSS-INDUCED ACUTE COLITIS MODEL: CPT1A$^{\Delta EC}$ and WT mice were exposed to vehicle or 2.5% dextrane sulfate sodium (DSS) (36,000-50,000 M.Wt., MP Biomedicals) in their drinking water for 7 consecutive days. Control groups The severity of colitis was evaluated by assessing the disease activity index (DAI) (which scores body weight loss, stool consistency and blood in the stool and anal region) of CPT1A$^{\Delta EC}$ and WT mice under DSS treatment. On day 7, mice were injected via the tail vein with dextran-rhodamine (70,000 kDA, ThermoFisher Scientific). Ten minutes after injection, mice were perfused and fixed (using 1% PFA perfusion) and the colon was harvested and processed for immunohistochemistry. Colon sections were stained with H&E for morphological analyses, with anti-CD105 (R&D Systems) to identify blood vessels, anti-CD45 antibodies to analyze immune cell infiltration and PCNA to identify proliferating cells. The sections were then incubated with an appropriate secondary antibody (Jackson Immuno Research) and TSA Fluorescein or TSA Cy5 amplification (Perkin Elmer) when needed. Nuclei were counterstained with Hoechst33342 (ThermoFisher Scientific). Imaging was performed using a Leica DMI6000B inverted microscope (Leica Microsystems). The leakiness of the vessels was measured by quantifying the extravascular dextran-rhodamine positive area. Morphometric analysis of the CD45$^+$ area in % of colon area was done using Leica MM AF powered by MetaMorph analysis software. Quantification of the vessel area in the colonic mucosa was done using Fiji software. EC proliferation was measured as the number of PCNA$^+$ CD105$^+$ ECs and expressed as a percentage of the total number of CD105$^+$ ECs per imaged filed using Fiji software.

HUMAN TISSUE ANALYSIS

IN SITU DETECTION OF CPT1A IN THE VASCULATURE: Human lung and kidney sections, obtained from Pathology Department from University of Leuven (KU Leuven), were used for immunostaining with anti-CD31 (Dako) and anti-CPT1A (Proteintech) primary antibodies. Appropriate fluorescently conjugated secondary antibodies (Jackson Immuno Research) were used, followed by TSA Cy5 amplification (Perkin Elmer) when needed. Imaging was performed immediately using a Zeiss LSM 780 confocal microscope (oil objective: x40) (Carl Zeiss).

QUANTIFICATION AND STATISTICAL ANALYSIS

Data represent mean ± SEM of at least three independent experiments. Statistical significance was calculated by standard two-tailed t test with Welch's correction, ANOVA (for multiple comparisons within one dataset), one sample t test (for comparisons to point-normalized data) and by log-rank test (for comparisons of survival distributions of two groups) using Prism v6.0f. When inter-experimental variability was large between experiments with ECs isolated from individual umbilical cord donors, mixed model statistics (R version 3.2.4 using Kenward-Roger approximation) was used with experiment (i.e. donor) as random factor to correct for confounding variation between individual EC isolations. Self-contained gene set analysis was performed via rotation gene set analysis (R, limma package). $P < 0.05$ was considered statistically significant.

DATA AND SOFTWARE AVAILABILITY

DATA RESOURCES

The microarray data have been deposited in the GEO database under ID code GSE89174. The RNA sequencing data have been deposited in the GEO database under ID code E-MTAB-6595.

SOFTWARE

All software is freely or commercially available and is listed in the STAR Methods description and

Key Resources Table.

Main Figure 1

Figure 1

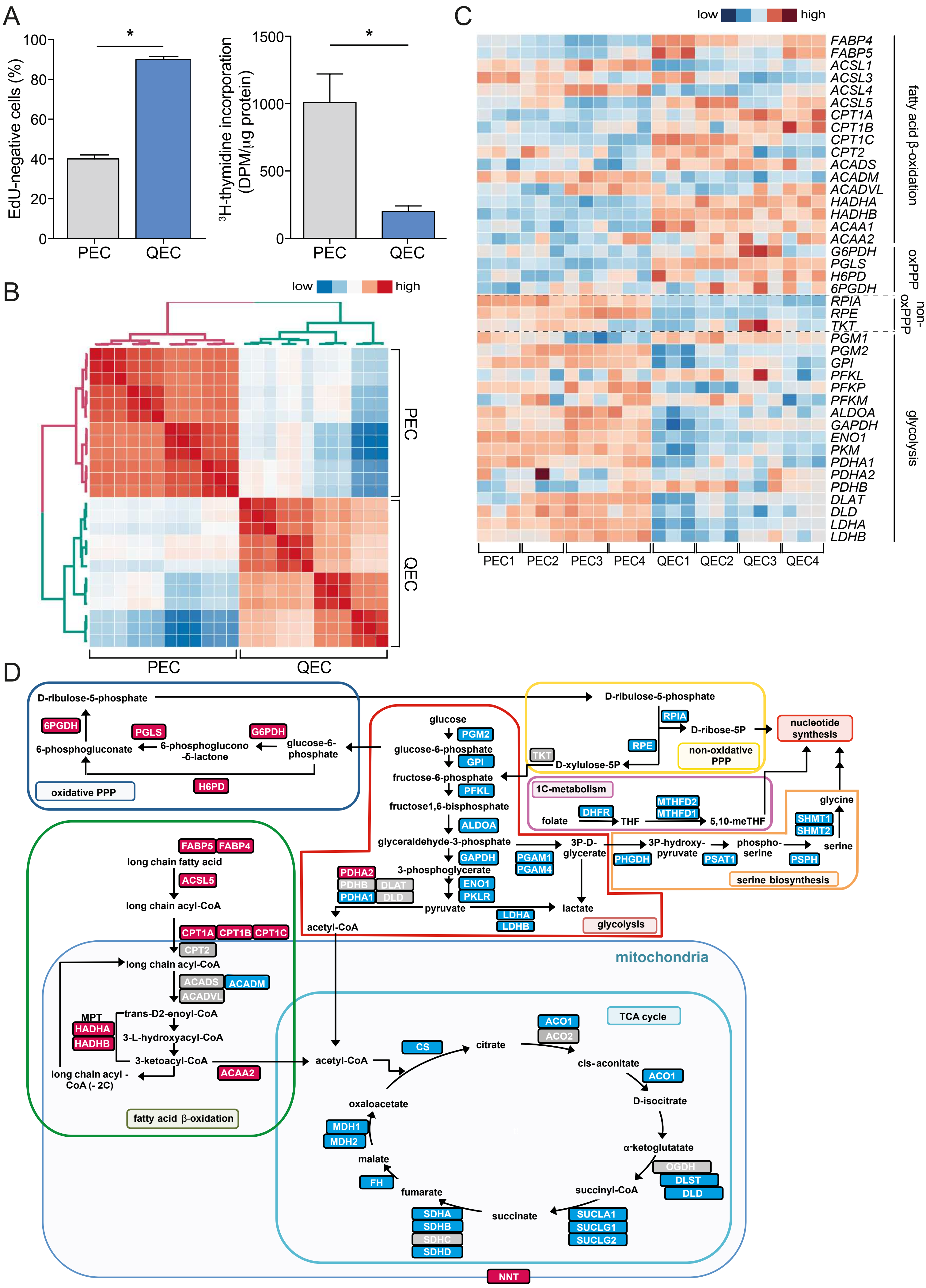

Figure 2

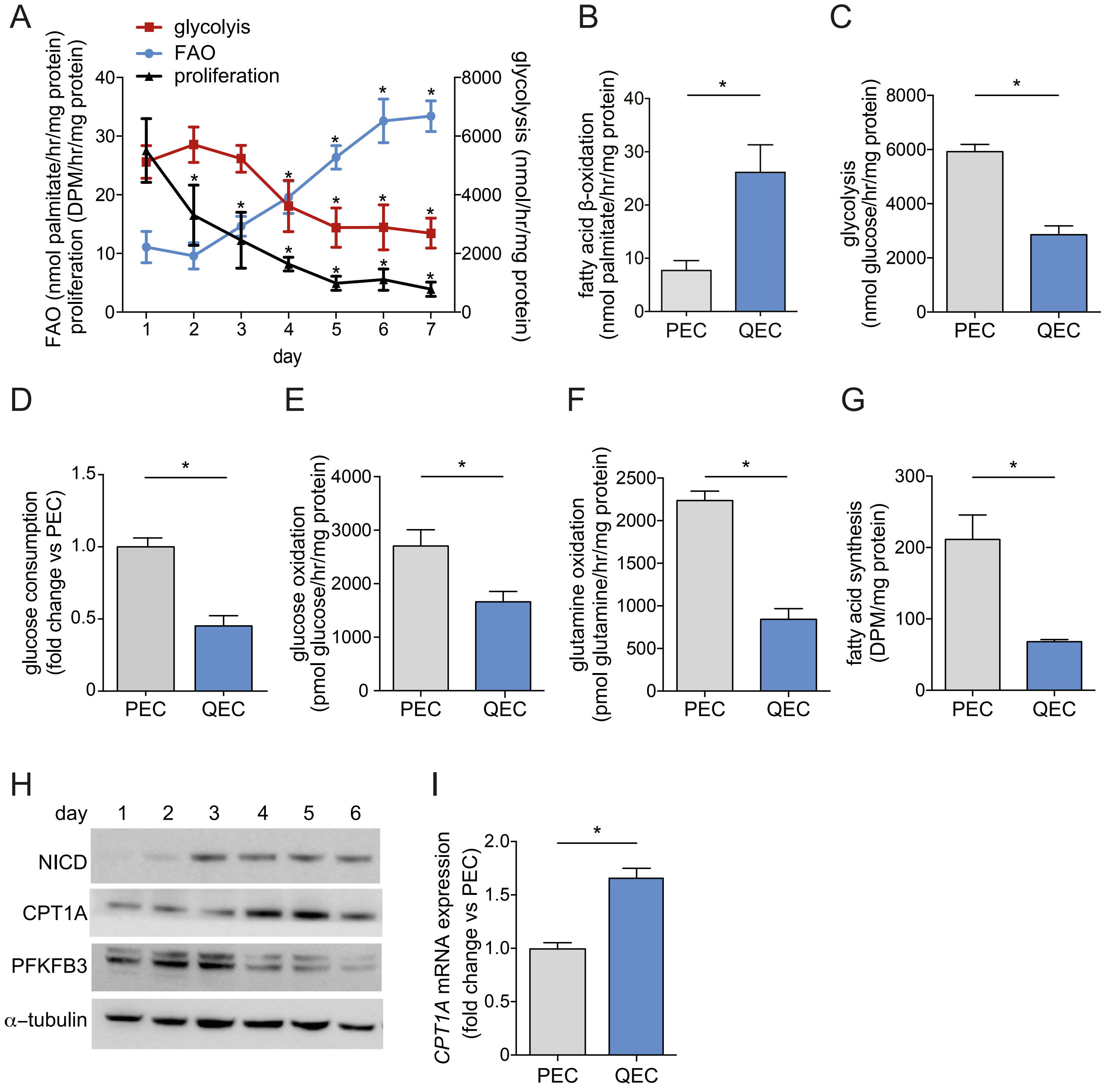
A
glycolyis
FAO
proliferation
FAO (nmol palmitate/hr/mg protein)
proliferation (DPM/hr/mg protein)
glycolysis (nmol/hr/mg protein)
0
10
20
30
40
0
2000
4000
6000
8000
1
2
3
4
5
6
7
day
*
B
fatty acid β-oxidation
(nmol palmitate/hr/mg protein)
0
10
20
30
40
PEC
QEC
*
C
glycolysis
(nmol glucose/hr/mg protein)
0
2000
4000
6000
8000
PEC
QEC
*
D
glucose consumption
(fold change vs PEC)
0
0.5
1.0
1.5
PEC
QEC
*
E
glucose oxidation
(pmol glucose/hr/mg protein)
0
1000
2000
3000
4000
PEC
QEC
*
F
glutamine oxidation
(pmol glutamine/hr/mg protein)
0
500
1000
1500
2000
2500
PEC
QEC
*
G
fatty acid synthesis
(DPM/mg protein)
0
100
200
300
PEC
QEC
*
H
day
1
2
3
4
5
6
NICD
CPT1A
PFKFB3
α–tubulin
I
CPT1A mRNA expression
(fold change vs PEC)
0
0.5
1.0
1.5
2.0
PEC
QEC
*

Main Figure 3

Figure 3

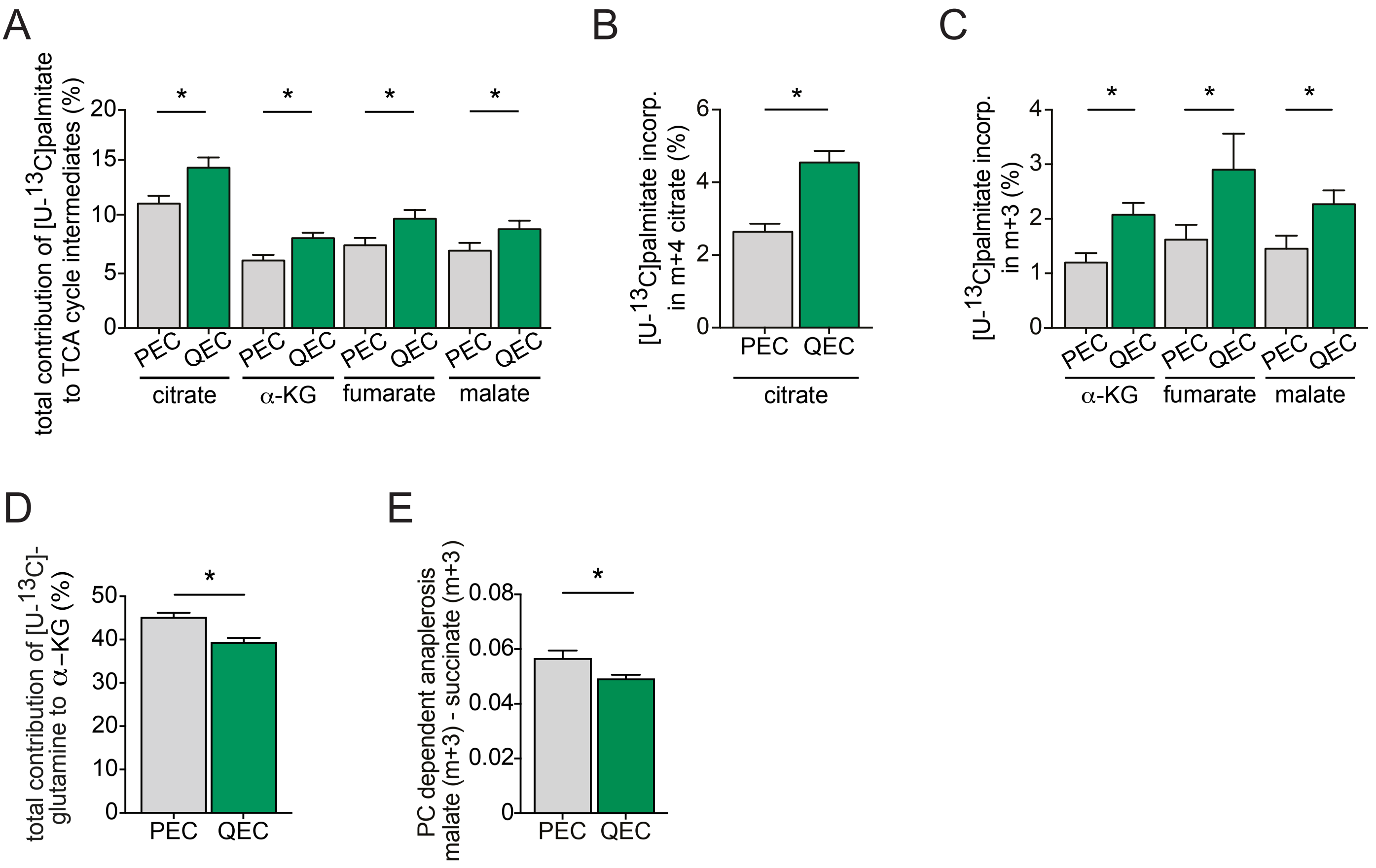

Main Figure 4

Figure 4

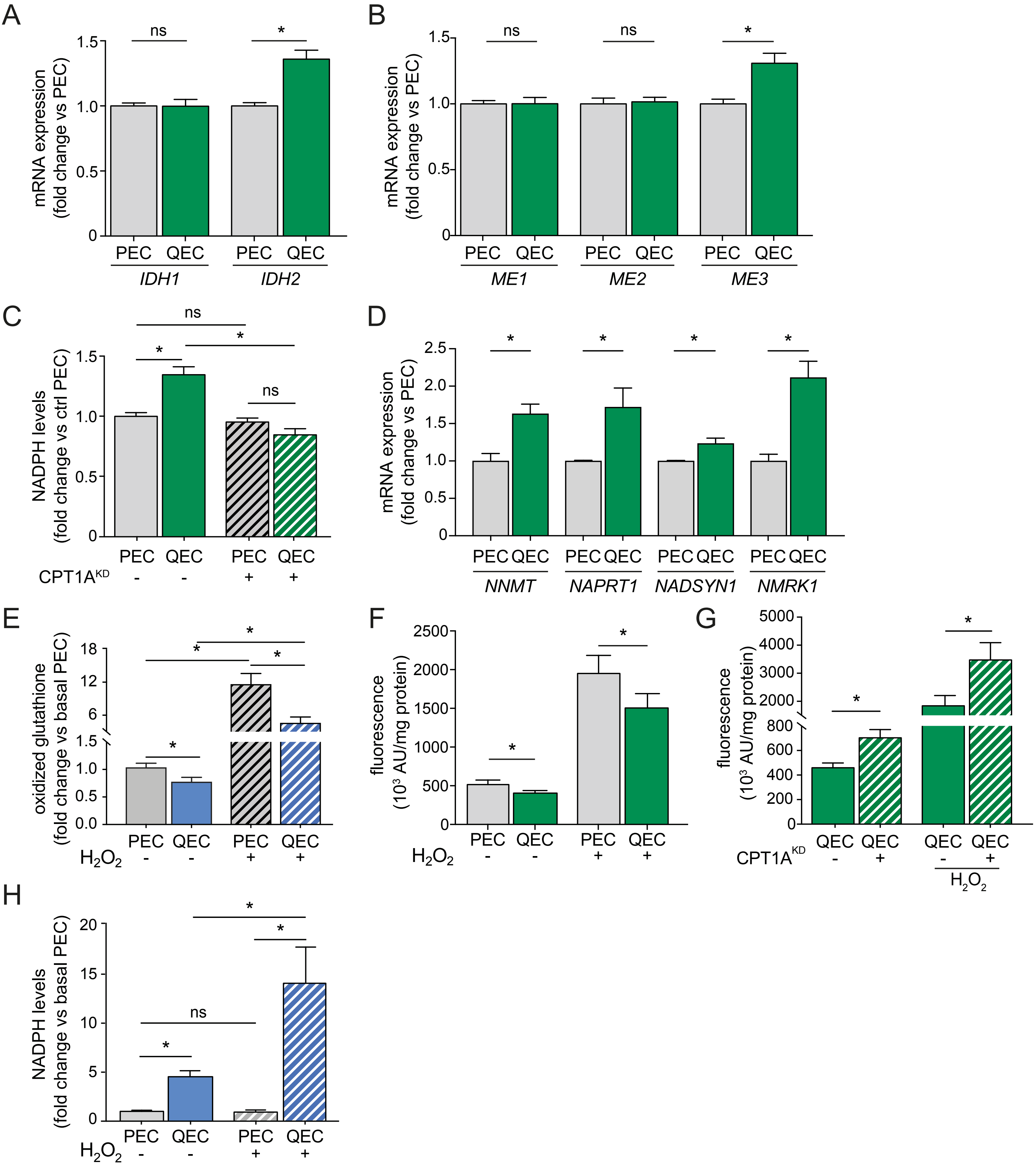

Figure 5

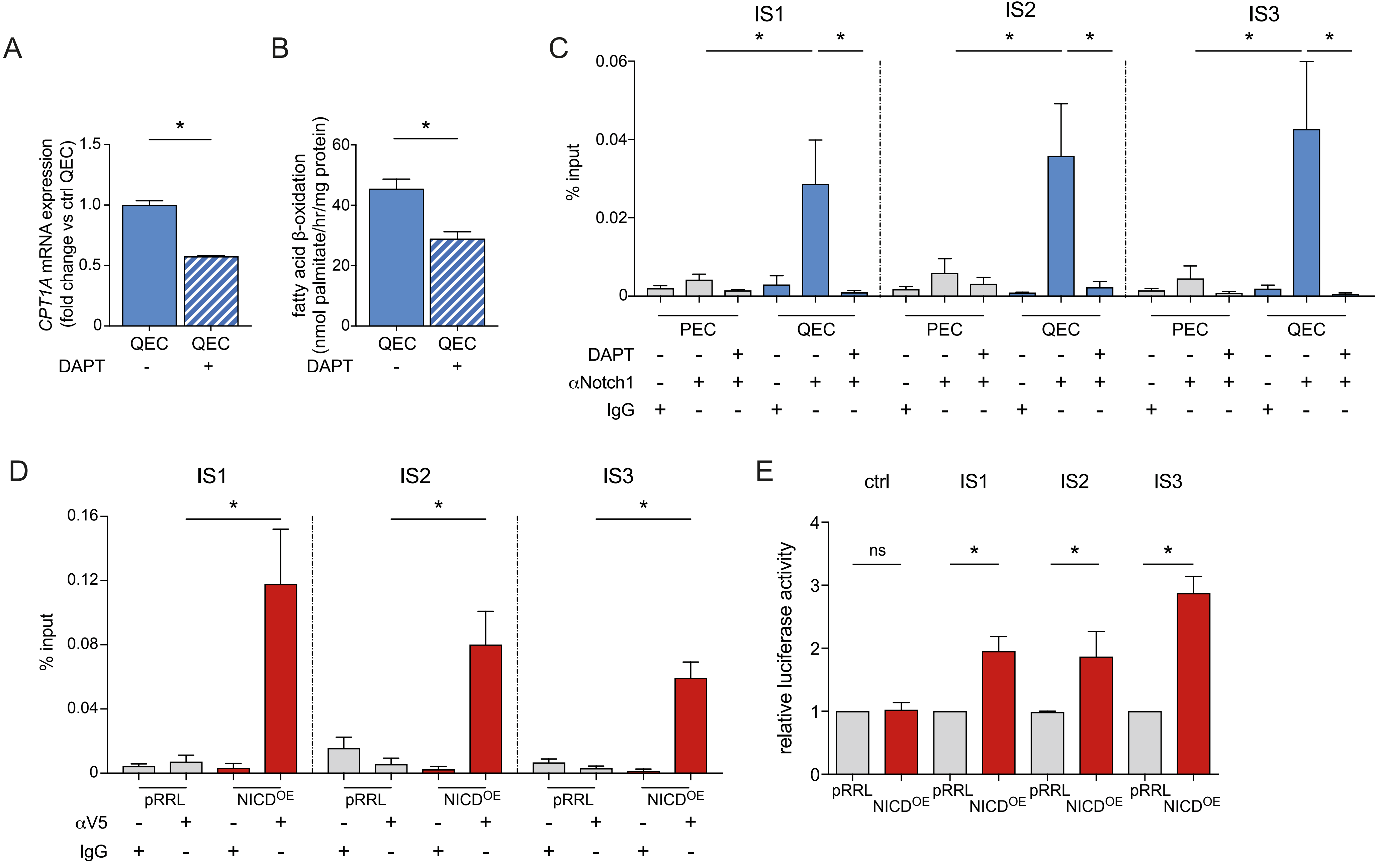

Main Figure 5

Main Figure 6

Figure 6

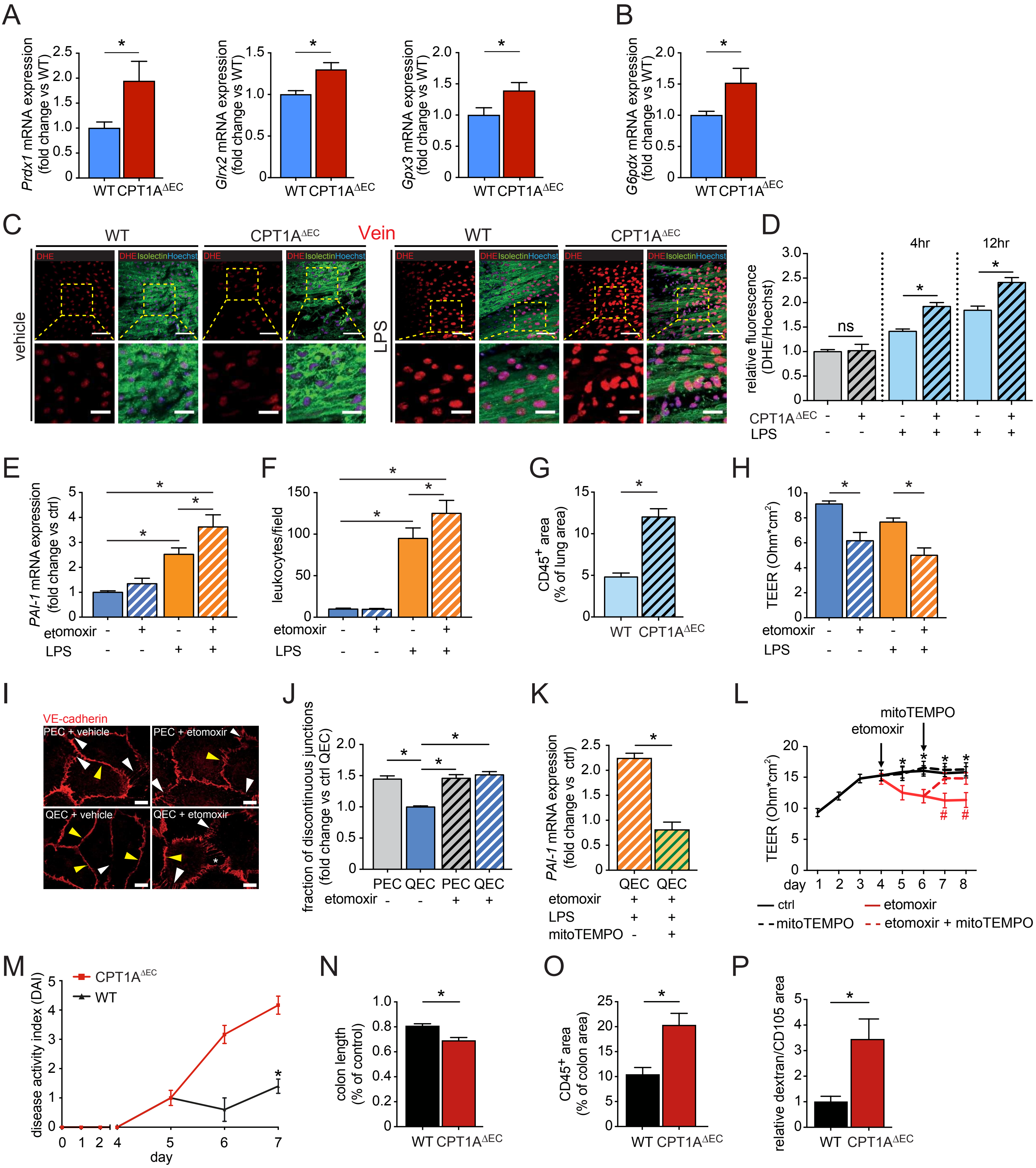

Main Figure 7

Figure 7

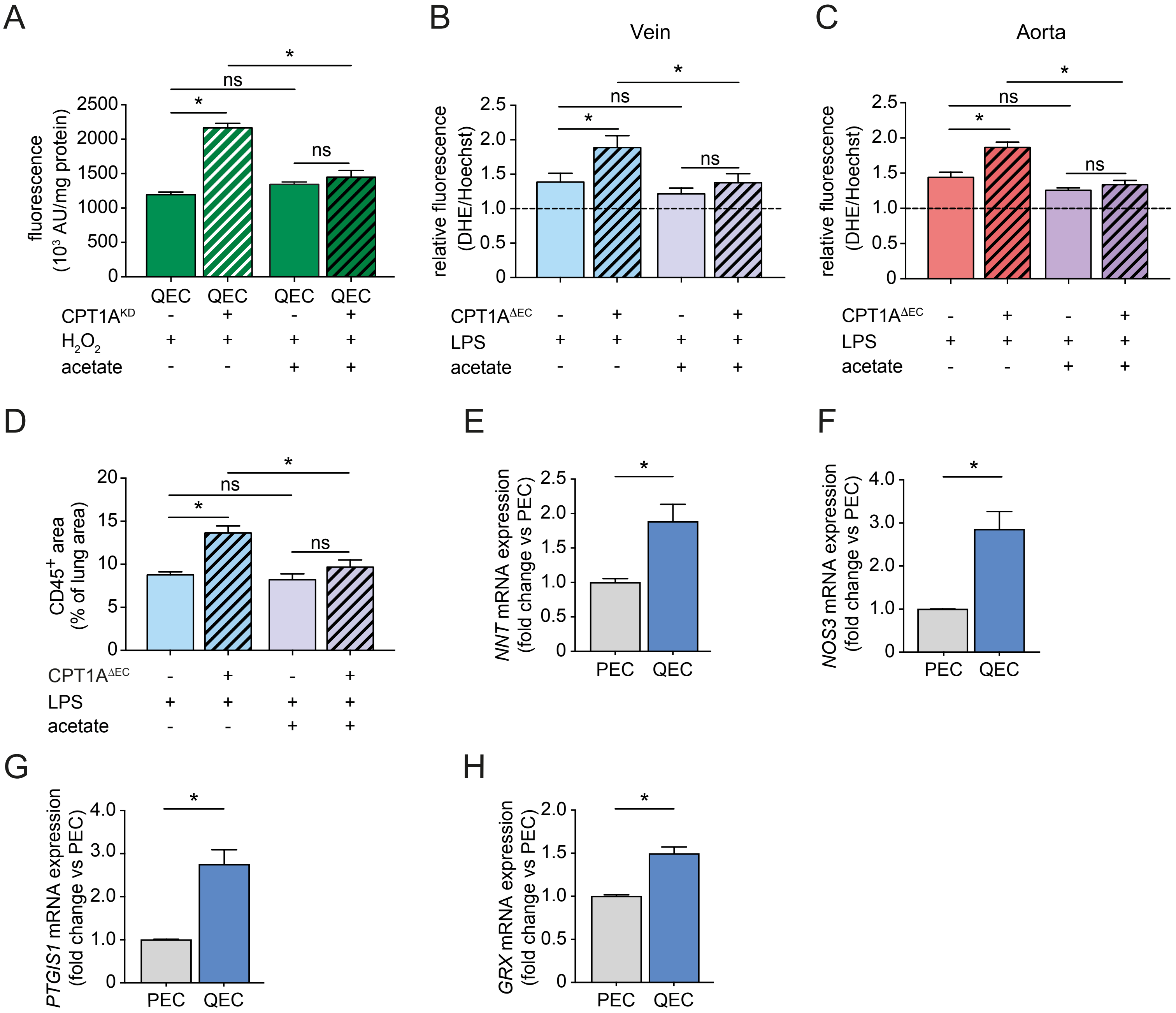

QUIESCENT ENDOTHELIAL CELLS UPREGULATE FATTY ACID β-OXIDATION FOR REDOX HOMEOSTASIS

KEY RESOURCES TABLE

REAGENT or RESOURCE	SOURCE	IDENTIFIER
Antibodies		
Anti-Mouse IgG, HRP-linked	Cell Signaling Technology	7076S; RRID:AB_330924
Anti-Rabbit IgG, HRP-linked	Cell Signaling Technology	7074S; RRID:AB_2099233
Donkey anti-Goat IgG	Jackson ImmunoResearch	705-065-003; RRID:AB_2340396
Donkey anti-Mouse IgG	Jackson ImmunoResearch	715-065-151; RRID:AB_2340785
Donkey anti-Rabbit IgG	Jackson ImmunoResearch	711-065-152; RRID:AB_2340593
Donkey anti-Rat IgG	Jackson ImmunoResearch	712-065-153; RRID:AB_2315779
Goat anti-CD105	R&D Systems	AF1320; RRID:AB_354735
Goat anti-Rabbit IgG, Alexa Fluor 568	ThermoFisher Scientific	A-11036; RRID:AB_10563566
Goat anti-Rabbit IgG, Alexa Fluor 647	ThermoFisher Scientific	A-21245; RRID:AB_2535813
Human-anti-CD102-APC	Miltenyi Biotec	130-112-030; RRID:AB_2654351
Mouse anti-CD31	Dako, Agilent	M0823; RRID:AB_2114471
Mouse anti-PCNA	Leica Biosystems	NCL-L-PCNA; RRID:AB_2315078
Mouse anti-V5 tag	ThermoFisher Scientific	R960-25; RRID:AB_2556564
Mouse anti-α-Tubulin	Sigma-Aldrich	T6074-100UL; RRID:AB_477582
Rabbit anti-acetyllysine	PTM-BioLab	PTM-105; RRID:N/A
Rabbit anti-Cleaved Notch1 (NICD)	Cell Signaling Technology	4147S; AB_2153348
Rabbit anti-CPT1A	Cell Signaling Technology	12252S; RRID:N/A
Rabbit anti-CPT1A	Proteintech	15184-1-AP; RRID:AB_2084676
Rabbit anti-PFKFB3	Cell Signaling Technology	13123S; RRID:AB_2617178
Rabbit anti-Phospho-AMPKα Thr172	Cell Signaling Technology	2531S; RRID:AB_330330
Rabbit anti-Total AMPKα	Cell Signaling Technology	2532S; RRID:AB_330331

Rabbit anti-VE-cadherin	ThermoFisher Scientific	PA5-19612; RRID:AB_10979589
Rat anti-CD45	BD Pharmingen	553076; RRID:AB_394606
Rat anti-CD45-PeCy7	ThermoFisher Scientific	25-0451-82; RRID:AB_469625
Rat anti-Notch1	Cell Signaling Technology	3447S; RRID:AB_2153498
Bacterial and Virus Strains		
N/A	N/A	N/A
Biological Samples		
Human blood samples (Commissie Medische Ethiek ZU/KU Leuven approval number S57736)	This paper	N/A
Chemicals, Peptides, and Recombinant Proteins		
[1-^{14}C]-D-glucose	Hartmann Analytic	ARC 0120A
[5-^{3}H] D-glucose	Perkin Elmer	NET531001MC
[6-^{14}C] D-glucose	Perkin Elmer	NEC045X050UC
[6-^{14}C]-D-glucose	Hartmann Analytic	ARC 0121A
[6-^{3}H] thymidine	Perkin Elmer	NET355L005MC
[9,10-^{3}H] palmitic acid	Perkin Elmer	NET043001MC
[U-^{13}C] D-glucose	Cambridge isotope laboratories	CLM-1396
[U-^{13}C] L-glutamine	Cambridge isotope laboratories	CLM-1166
[U-^{13}C] potassium palmitate	Cambridge isotope laboratories	CLM-3943
[U-^{13}C] sodium acetate	Sigma-Aldrich	282014
[U-^{14}C] acetate	Perkin Elmer	NEC553050UC
[U-^{14}C] glutamine	Perkin Elmer	NEC451050UC
[U-^{14}C] palmitic acid	Perkin Elmer	NEC534050UC
1-[2,3,4-trimethoxybenzyl]piperazine dihydrochloride (TMZ)	Sigma-Aldrich	653322
5-ethynyl-2´-deoxyuridine (EdU)	ThermoFisher Scientific	A10044
Alexa-488 Fluor conjugated phalloidin	ThermoFisher Scientific	A12379
Alexa-647 Fluor conjugated isolectin B4	ThermoFisher Scientific	I32450
Calcein	ThermoFisher Scientific	C1430
CM-H_2DCFDA	ThermoFisher Scientific	C6827
CPT1A inhibitor (+)-etomoxir sodium salt hydrate (2[6(4-chlorophenoxy)hexyl]oxirane-2-carboxylate	WuXi AppTec	N/A

Delta like ligand 4 (rhDll4)	R&D Systems	1506-D4-050/CF
Dextran sulfate sodium (DSS) 36,000-50,000 M.Wt.	MP Biomedicals	0216011010
Dextran, Tetramethylrhodamine, 70,000 MW, Lysine Fixable	Thermo Fisher Scientific	D1818
DHE (dihydroethidium)	ThermoFisher Scientific	D1168
dNTP Set (100 mM)	ThermoFisher Scientific	10297018
eBioscience™ Fixable Viability Dye eFluor™ 450	ThermoFisher Scientific	65-0863-14
Ficoll-paque plus	GE Healthcare	17144002
Hoechst 33342	ThermoFisher Scientific	H3570
Potassium hydroxycitrate tribasic monohydrate	Sigma-Aldrich	59847
L-carnitine	Sigma-Aldrich	C0283
L-glutamine	ThermoFisher Scientific	25030024
Lipopolysaccharides from Escherichia coli 0111:B4	Sigma-Aldrich	L2630-100MG
MitoSOX™ Red	ThermoFisher Scientific	M36008
MitoTEMPO	Sigma-Aldrich	SML0737
Oligo(dT)20 Primer	ThermoFisher Scientific	18418020
Oligomycin	Sigma-Aldrich	O4876
Phosphatase inhibitors (PhosSTOP™)	Roche	04906837001
Protease inhibitors (cOmplete™, EDTA-free Protease Inhibitor Cocktail)	Roche	11873580001
Proteinase K	ThermoFisher Scientific	25530049
RNase A	ThermoFisher Scientific	EN0531
RNaseOUT™ Recombinant Ribonuclease Inhibitor	ThermoFisher Scientific	10777019
Sodium acetate	Sigma-Aldrich	S2889
Sodium palmitate	Sigma-Aldrich	P9767
Sodium pyruvate	ThermoFisher Scientific	11360070
Tamoxifen	Sigma-Aldrich	T5648
Trichloroacetic acid (TCA)	Sigma-Aldrich	T6399
X-Gal (5-bromo-4-chloro-3-indolyl-β-D-galactoside)	ThermoFisher Scientific	15520034
γ-secretase inhibitor DAPT (N-[N-(3,5-Difluorophenacetyl)-L-alanyl]-S-phenylglycine t-butyl ester)	Sigma-Aldrich	D5942
Critical Commercial Assays		
Acetyl-Histone Antibody Sampler Kit	Cell Signaling Technology	9933T
Agencourt AMPure XP	Beckman Coulter	A63880

Amplex® Red Hydrogen Peroxide/Peroxidase Assay Kit	ThermoFisher Scientific	A22118
ATPlite™	Perkin Elmer	6016943
CD31 MicroBead Kit, human	Miltenyi Biotec	130-091-935
CD31 MicroBeads, mouse	Miltenyi Biotec	130-097-418
CD45 MicroBeads, mouse	Miltenyi Biotec	130-052-301
Click-iT® EdU Alexa Fluor® 488 Imaging Kit	ThermoFisher Scientific	C10337
Click-iT® EdU Alexa Fluor® 647 Imaging Kit	ThermoFisher Scientific	C10340
Cytotoxicity Detection Kit^{PLUS} (LDH)	Roche	04744934001
Dual Luciferase Reporter Kit	Promega	E1910
Illumina™ TotalPrep™ RNA Amplification Kit	ThermoFisher Scientific	AMIL1791
iScript cDNA synthesis kit	Bio-Rad	1708891
Lung Dissociation Kit, mouse	Miltenyi Biotec	130-095-927
MACSPlex Cytokine Kit (mouse)	Miltenyi Biotec	130-101-740
Nucleofector™ Kits for Human Umbilical Vein Endothelial Cells (HUVEC)	Lonza	VPB-1002
Pierce Protein A/G Magnetic Beads	ThermoFisher Scientific	88802
Pierce™ ECL Western Blotting Substrate	ThermoFisher Scientific	32106
PowerUp™ SYBR® Green Master Mix	ThermoFisher Scientific	A25742
PureLink® RNA Mini Kit	ThermoFisher Scientific	12183018A
SuperScript™ III Reverse Transcriptase	ThermoFisher Scientific	18080044
SuperSignal™ West Femto Maximum Sensitivity Substrate	ThermoFisher Scientific	34095
TaqMan™ Fast Universal PCR Master Mix (2X), no AmpErase™ UNG	ThermoFisher Scientific	4364103
TSA® Cyanine 3 (Cy3) System	Perkin Elmer	NEL704A001KT
TSA® Cyanine 5 (Cy5) System	Perkin Elmer	NEL705A001KT
TSA® Fluorescein System	Perkin Elmer	NEL701A001KT
Deposited Data		
Microarray raw and analyzed data	This paper	GEO: GSE89174
RNA-sequencing raw and analyzed data	This paper	ArrayExpress: E-MTAB-6595
Experimental Models: Cell Lines		
293T cells	ATCC	CRL-3216
Human umbilical artery endothelial cells (HUAECs); (Approved by Medical Ethical Committee KU Leuven/UZ Leuven; approval number S57123)	UZ Leuven	N/A
Human umbilical vein endothelial cells (HUVECs); Approved by Medical Ethical Committee KU Leuven/UZ Leuven;	UZ Leuven	N/A

approval number S57123		
Mouse endothelial cells; Approved by the Institutional Animal Ethics Commitee oft he KU Leuven.	This paper	N/A
Experimental Models: Organisms/Strains		
Mouse: CPT1A$^{lox/lox}$ C57Bl/6	Schoors et al., 2015	N/A
Mouse: Cre-driver line Cdh5(PAC)-Cre^{ERT2} C57Bl/6	Benedito et al., 2009	N/A
Oligonucleotides		
ChiP-qPCR (Table S8)	IDT	N/A
qRT-PCR Primers (Table S8)	IDT	N/A
shRNA (Table S8)	Sigma-Aldrich Schoors et al., 2015	N/A
Recombinant DNA		
pGL3 basic luciferase plasmid	Promega	E1751
pHyPer-dMito vector	Evrogen	FP942
pLKO-shRNA2 vector	Clontech	No. PT4052-5
pRRLsinPPT.CMV.MCS MM W prevector	Gift from M. Mazzone	N/A
V5 tagged murine Notch1 NICD cDNA	Gift from M. Potente	N/A
Software and Algorithms		
Adobe Illustrator CC	Adobe Systems Incorporated	https://www.adobe.com/be_en/products/illustrator.html
D3heatmap package	Cantelmo et al., 2016	N/A
EdgeR package	Cantelmo et al., 2016	N/A
Fiji (Image J)	Open Source	https://fiji.sc
FlowJo 8.8.6 software	FlowJo, LLC	https://www.flowjo.com
Prism v.6 software	Grpahpad	http://www.graphpad.com
Leica MM AF powered by MetaMorph® analysis software	Leica microsystems	N/A
limma package	Cantelmo et al., 2016	N/A
Pathview package	Cantelmo et al., 2016	N/A
Pvclust package	Cantelmo et al., 2016	N/A
RStudio	Open Source	https://www.rstudio.com
Xcalibur™ Software	ThermoFisher Scientific	N/A
Other		
16% Formaldehyde (w/v), Methanol-free	ThermoFisher Scientific	28906
6.5 mm Transwell® with 0.4 µm Pore Polyester Membrane Insert	Corning	3470

Antibiotic-Antimycotic (100X)	ThermoFisher Scientific	15240062
Bovine Serum Albumin	Sigma-Aldrich	A8806
CAT-peg	Sigma-Aldrich	C4963
Cell lysis buffer (10x)	Cell Signaling Technology	9803
Collagenase I	ThermoFisher Scientific	17100017
Collagenase I	Sigma-Aldrich	C0130
Collagenase II	ThermoFisher Scientific	17101015
Collagenase IV	Worthington Biochemical Corporation	LS004188
Corning® 100µm Cell Strainer	Corning	431752
DIPPMPO	Enzo Life Science	ALX-430-119-M050
Dispase II	ThermoFisher Scientific	17105041
DNase I	Sigma-Aldrich	D4527
DTPA	Sigma-Aldrich	D6518
Dulbecco's phosphate-buffered saline (DPBS)	ThermoFisher Scientific	14190144
Dulbecco's Modified Eagle medium	ThermoFisher Scientific	41965047
EGM2 (Endothelial growth medium)	PromoCell	C-22011
Endothelial cell growth factor supplements (ECGS/ Heparin)	PromoCell	C-30120
Endothelial Cell Growth Medium 2 SupplementMix	PromoCell	C-39216
Falcon® 70 µm Cell Strainer	Corning	352350
FBS (Fetal Bovine Serum)	Biochrom BmgH	S0115
FBS (Fetal Bovine Serum), charcoal stripped	Sigma-Aldrich	F6765
Gelatin from bovine skin	Sigma-Aldrich	G9391
Hydrogen peroxide 30%	Merck, Millipore	8222871000
IGEPAL® CA-630	Sigma-Aldrich	I8896
Ketamine 100mg/ml	NIMATEK	N/A
Medium 199 (M199), HEPES	ThermoFisher Scientific	22340020
MEM Non-Essential Amino Acids Solution	ThermoFisher Scientific	11140050
Nitrocellulose Pre-Cut Blotting Membranes, 0.45 µm pore size	ThermoFisher Scientific	LC2001
NuPAGE™ 10% Bis-Tris Protein Gels, 1.5 mm, 10-well	ThermoFisher Scientific	NP0315BOX
NuPAGE™ 4-12% Bis-Tris Protein Gels, 1.5 mm, 10-well	ThermoFisher Scientific	NP0335BOX
NuPAGE™ LDS Sample Buffer (4X)	ThermoFisher Scientific	NP0007
NuPAGE™ MES SDS Running Buffer (20X)	ThermoFisher Scientific	NP0002
NuPAGE™ MOPS SDS Running Buffer (20X)	ThermoFisher Scientific	NP0001
NuPAGE™ Sample Reducing Agent (10X)	ThermoFisher Scientific	NP0009

NuPAGE™ Transfer Buffer (20X)	ThermoFisher Scientific	NP00061
Penicillin/streptomycin	ThermoFisher Scientific	15140122
PVDF Pre-cut Blotting Membranes, 0.2 µm pore size	ThermoFisher Scientific	LC2002
SOD-peg	Sigma-Aldrich	S9549
Sodium butyrate	Sigma-Aldrich	303410
SuperFrost Excell object slides	Thermo Scientific Menzel	J5800AMNZ
TE (Tris-EDTA) buffer	ThermoFisher Scientific	12090015
Trichostatin A (TSA)	Sigma-Aldrich	T8552
TRIzol LS reagent	ThermoFisher Scientific	10296028
Trypsin-EDTA (0.25%)	ThermoFisher Scientific	25200056
XYL-M2%	Livestock Pharma	BEV170581

Figure S1

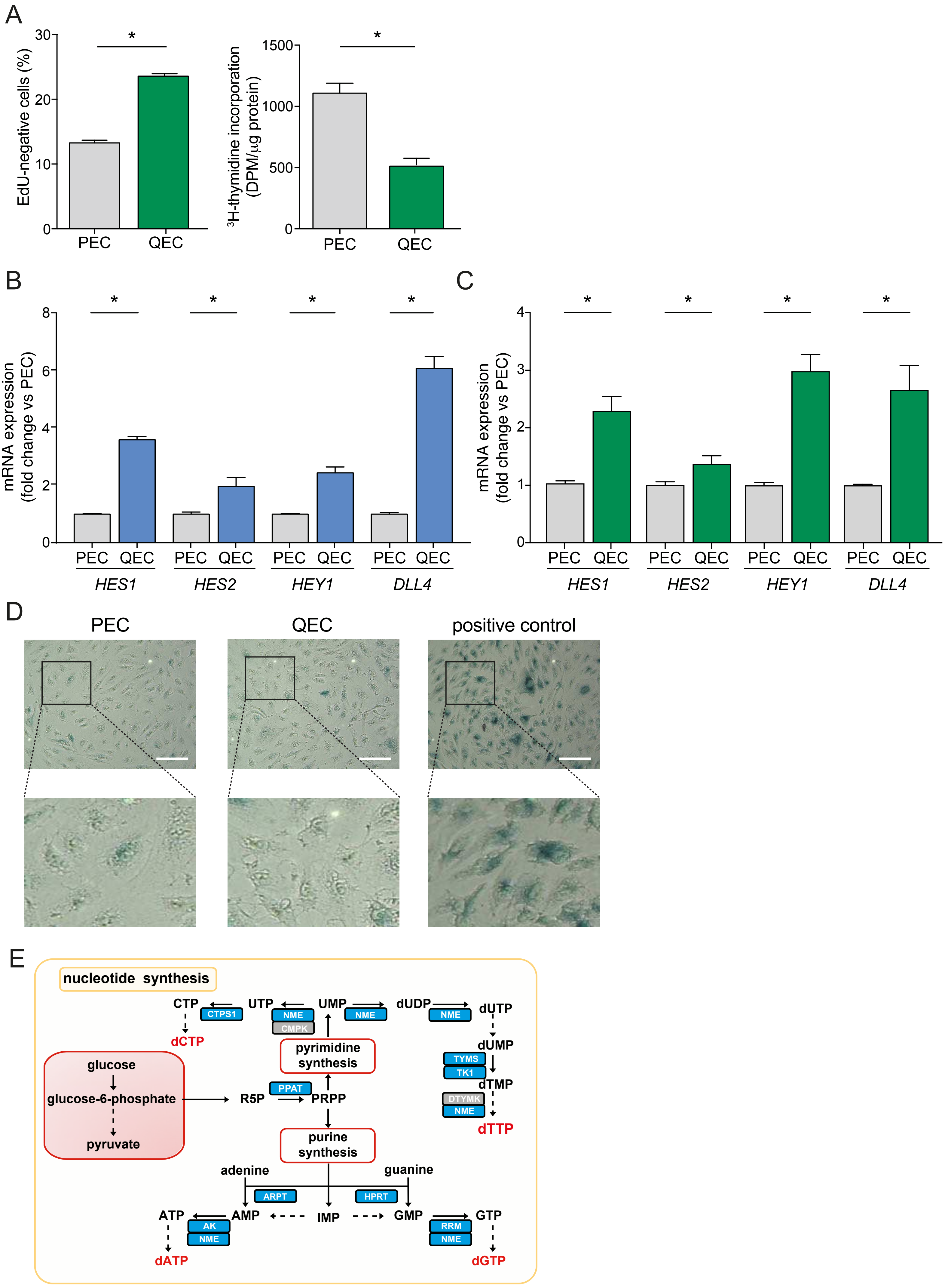
A
EdU-negative cells (%)
30
20
10
0
*
PEC
QEC
^{3}H-thymidine incorporation (DPM/μg protein)
1500
1000
500
0
*
PEC
QEC
B
mRNA expression (fold change vs PEC)
8
6
4
2
0
*
PEC QEC
HES1
HES2
HEY1
DLL4
C
mRNA expression (fold change vs PEC)
4
3
2
1
0
*
PEC QEC
HES1
HES2
HEY1
DLL4
D
PEC
QEC
positive control
E
nucleotide synthesis
CTP
CTPS1
UTP
NME
CMPK
UMP
NME
dUDP
NME
dUTP
dCTP
pyrimidine synthesis
dUMP
TYMS
TK1
dTMP
DTYMK
NME
dTTP
glucose
glucose-6-phosphate
pyruvate
R5P
PPAT
PRPP
purine synthesis
adenine
guanine
ARPT
HPRT
ATP
AK
NME
AMP
IMP
GMP
RRM
NME
GTP
dATP
dGTP

SUPPLEMENTAL FIGURE LEGENDS

FIGURE S1 (RELATED TO FIGURE 1): INDUCTION OF QUIESCENCE VIA CONTACT INHIBITION OR NOTCH ACTIVATION.

(**A**) Percentage of EdU^{neg} cells (EdU incorporation assay; left) and ^{3}H-thymidine incorporation into DNA (proliferation assay; right) in Dll4-induced QECs vs PECs (n=4). DPM, disintegrations per minute. (**B-C**) qRT-PCR analysis of NOTCH target genes *HES1, HES2, HEY1* and the NOTCH ligand *DLL4* in contact-inhibited QECs relative to PECs (n=5) (B) and in Dll4-induced QECs relative to PECs (C) (n=3). (**D**) Representative micrographs of senescence-associated β-galactosidase staining in Dll4-induced QECs vs PECs and aged ECs (positive control); note the minimal / absent β-galactosidase staining in PECs and QECs. Lower panels show larger magnifications of the boxed areas in the upper panels. Scale bar: 100 µm. (n=3) (**E**) Pathway map showing changes in transcript levels of genes involved in nucleotide synthesis in QECs relative to PECs. Dashed arrows indicate multiple steps in the presented pathway (not shown for reasons of simplicity). Color scale: gray: unchanged, change <15%; blue: downregulated by at least 15%. For full gene names, see Table S3. Statistics: mixed models statistics (A) or two-tailed t test with Welch correction (B,C). Data are mean ± SEM; *p<0.05.

Figure S2

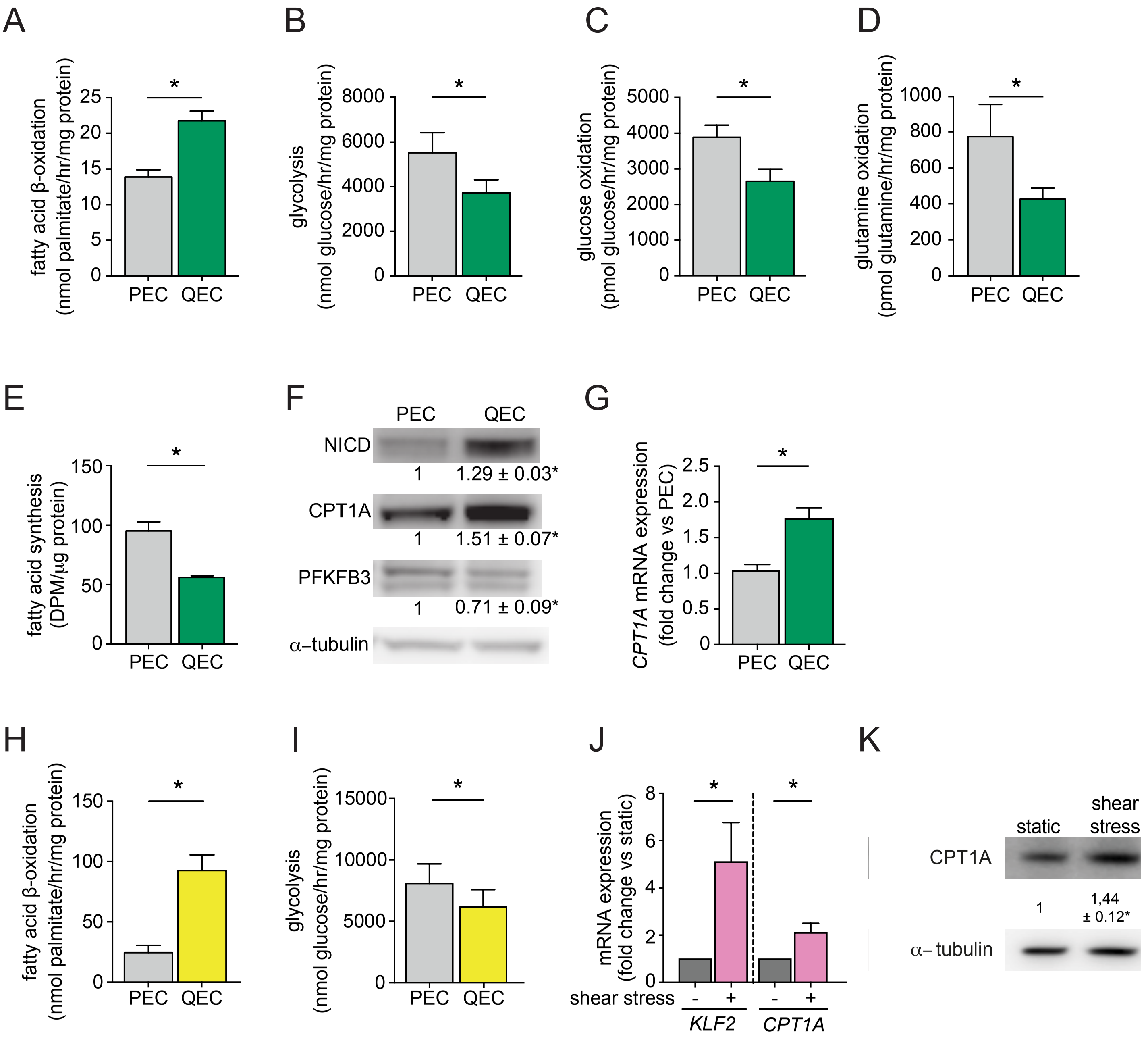
A
fatty acid β-oxidation
(nmol palmitate/hr/mg protein)
0
5
10
15
20
25
PEC
QEC
*
B
glycolysis
(nmol glucose/hr/mg protein)
0
2000
4000
6000
8000
PEC
QEC
*
C
glucose oxidation
(pmol glucose/hr/mg protein)
0
1000
2000
3000
4000
5000
PEC
QEC
*
D
glutamine oxidation
(pmol glutamine/hr/mg protein)
0
200
400
600
800
1000
PEC
QEC
*
E
fatty acid synthesis
(DPM/μg protein)
0
50
100
150
PEC
QEC
*
F
PEC
QEC
NICD
1
1.29 ± 0.03*
CPT1A
1
1.51 ± 0.07*
PFKFB3
1
0.71 ± 0.09*
α–tubulin
G
CPT1A mRNA expression
(fold change vs PEC)
0
0.5
1.0
1.5
2.0
2.5
PEC
QEC
*
H
fatty acid β-oxidation
(nmol palmitate/hr/mg protein)
0
50
100
150
PEC
QEC
*
I
glycolysis
(nmol glucose/hr/mg protein)
0
5000
10000
15000
PEC
QEC
*
J
mRNA expression
(fold change vs static)
0
2
4
6
8
shear stress
-
+
KLF2
-
+
CPT1A
*
*
K
static
shear stress
CPT1A
1
1,44
± 0.12*
α– tubulin

FIGURE S2 (RELATED TO FIGURE 2): METABOLIC ADAPTATIONS IN QECS.

(**A-E**) Metabolic adaptations in QECs upon induction of EC quiescence by Dll4 stimulation. FAO (A), glycolytic rate (B), glucose oxidation (C), glutamine oxidation (D), and fatty acid synthesis (measured by [U-^{14}C]-acetate incorporation in fatty acids) (E) in QECs vs PECs (n=4-5). (**F**) Representative immunoblot for Notch intracellular domain (NICD), CPT1A and PFKFB3 in Dll4-induced QECs vs PECs. Densitometric quantification normalized to α-tubulin is shown beneath each blot (n=5). (**G**) qRT-PCR analysis of *CPT1A* expression in Dll4-induced QECs relative to PECs (n=3). (**H,I**) Analysis of FAO (H) and glycolysis (I) in human arterial ECs (HAECs) in contact inhibited QECs vs PECs (n=3). (**J**) qRT-PCR analysis of *KLF2* and *CPT1A* expression in control ECs (static condition) and ECs exposed to laminar shear stress (shear stress) (10 dynes/cm^2) (n=6). qRT-PCR data are expressed relative to the levels of control (static) ECs. (**K**) Representative immunoblot for CPT1A in control ECs (static condition) and ECs exposed to laminar shear stress (shear stress) (10 dynes/cm^2). Densitometric quantification of the ratio of CPT1A to α-tubulin, expressed relative to the levels of control (static) ECs, is shown beneath the blot (n=6). DPM, disintegrations per minute. Statistics: mixed models statistics (A-E, H,I), one sample t test (F,J,K) or two-tailed t test with Welch correction (G). Data are mean ± SEM; *p<0.05.

Figure S3

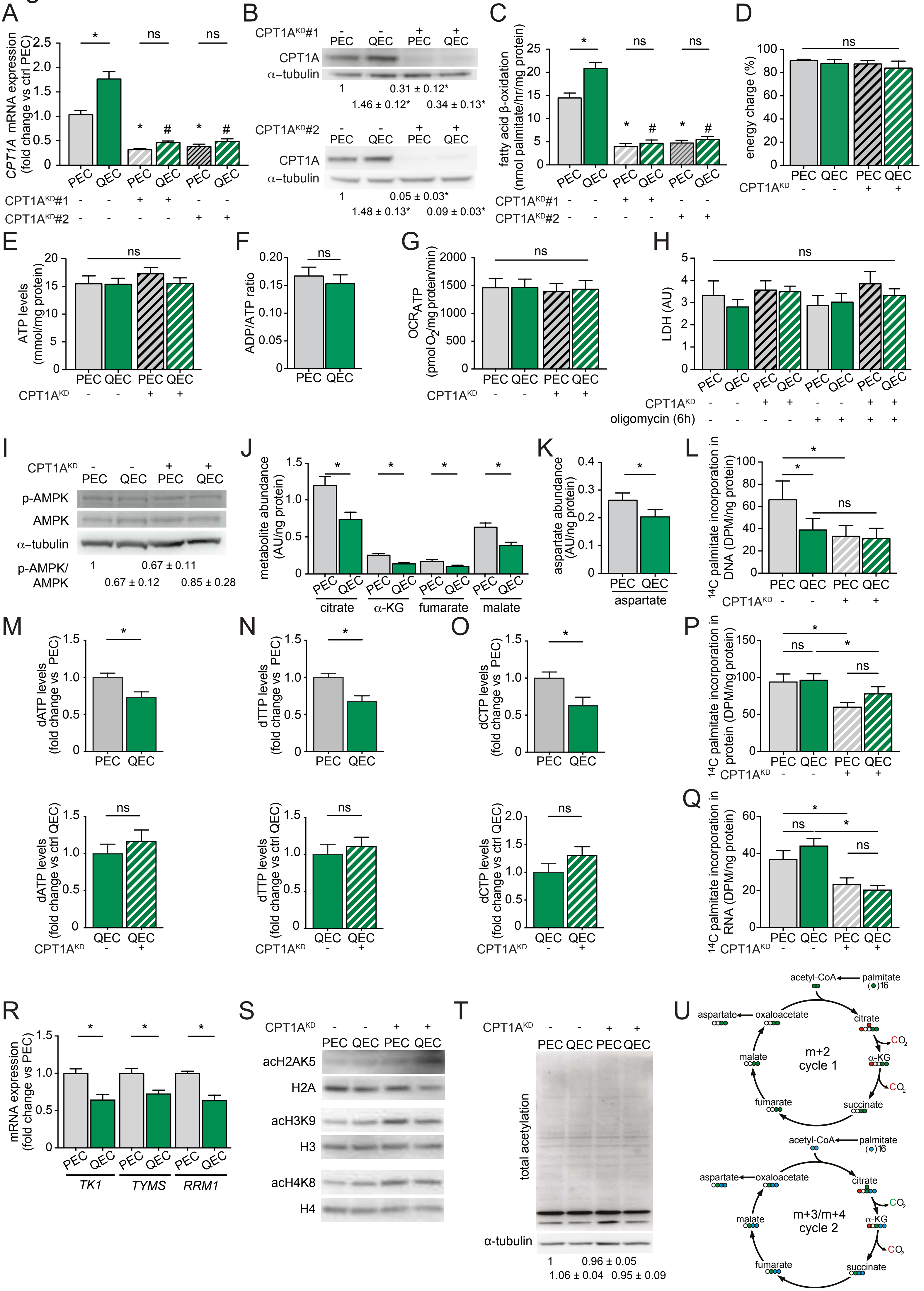
A
CPT1A mRNA expression (fold change vs ctrl PEC)
2.5
2.0
1.5
1.0
0.5
0
*
ns
ns
*
#
*
#
PEC
QEC
PEC
QEC
PEC
QEC
CPT1A^KD#1 - - + + - -
CPT1A^KD#2 - - - - + +
B
CPT1A^KD#1 - - + +
PEC QEC PEC QEC
CPT1A
α–tubulin
1
0.31 ± 0.12*
1.46 ± 0.12*
0.34 ± 0.13*
CPT1A^KD#2 - - + +
PEC QEC PEC QEC
CPT1A
α–tubulin
1
0.05 ± 0.03*
1.48 ± 0.13*
0.09 ± 0.03*
C
fatty acid β-oxidation (nmol palmitate/hr/mg protein)
25
20
15
10
5
0
*
ns
ns
*
#
*
#
PEC
QEC
PEC
QEC
PEC
QEC
CPT1A^KD#1 - - + + - -
CPT1A^KD#2 - - - - + +
D
energy charge (%)
100
80
60
40
20
0
ns
PEC QEC PEC QEC
CPT1A^KD - - + +
E
ATP levels (mmol/mg protein)
20
15
10
5
0
ns
PEC QEC PEC QEC
CPT1A^KD - - + +
F
ADP/ATP ratio
0.20
0.15
0.10
0.05
0
ns
PEC QEC
G
OCR_ATP (pmol O_2/mg protein/min)
2000
1500
1000
500
0
ns
PEC QEC PEC QEC
CPT1A^KD - - + +
H
LDH (AU)
5
4
3
2
1
0
ns
PEC QEC PEC QEC PEC QEC PEC QEC
CPT1A^KD - - + + - - + +
oligomycin (6h) - - - - + + + +
I
CPT1A^KD - - + +
PEC QEC PEC QEC
p-AMPK
AMPK
α–tubulin
p-AMPK/AMPK
1
0.67 ± 0.11
0.67 ± 0.12
0.85 ± 0.28
J
metabolite abundance (AU/ng protein)
1.5
1.0
0.5
0
*
*
*
*
PEC QEC
citrate
PEC QEC
α-KG
PEC QEC
fumarate
PEC QEC
malate
K
aspartate abundance (AU/ng protein)
0.4
0.3
0.2
0.1
0
*
PEC QEC
aspartate
L
14C palmitate incorporation in DNA (DPM/ng protein)
100
80
60
40
20
0
*
*
ns
PEC QEC PEC QEC
CPT1A^KD - - + +
M
dATP levels (fold change vs PEC)
1.5
1.0
0.5
0
*
PEC QEC
dATP levels (fold change vs ctrl QEC)
1.5
1.0
0.5
0
ns
QEC QEC
CPT1A^KD - +
N
dTTP levels (fold change vs PEC)
1.5
1.0
0.5
0
*
PEC QEC
dTTP levels (fold change vs ctrl QEC)
1.5
1.0
0.5
0
ns
QEC QEC
CPT1A^KD - +
O
dCTP levels (fold change vs PEC)
1.5
1.0
0.5
0
*
PEC QEC
dCTP levels (fold change vs ctrl QEC)
2.0
1.5
1.0
0.5
0
ns
QEC QEC
CPT1A^KD - +
P
14C palmitate incorporation in protein (DPM/ng protein)
150
100
50
0
*
ns
*
ns
PEC QEC PEC QEC
CPT1A^KD - - + +
Q
14C palmitate incorporation in RNA (DPM/ng protein)
60
40
20
0
*
ns
*
ns
PEC QEC PEC QEC
CPT1A^KD - - + +
R
mRNA expression (fold change vs PEC)
1.5
1.0
0.5
0
*
*
*
PEC QEC
TK1
PEC QEC
TYMS
PEC QEC
RRM1
S
CPT1A^KD - - + +
PEC QEC PEC QEC
acH2AK5
H2A
acH3K9
H3
acH4K8
H4
T
CPT1A^KD - - + +
PEC QEC PEC QEC
total acetylation
α-tubulin
1
0.96 ± 0.05
1.06 ± 0.04
0.95 ± 0.09
U
acetyl-CoA
palmitate
(●)16
aspartate
oxaloacetate
citrate
CO_2
malate
m+2
cycle 1
α-KG
CO_2
fumarate
succinate
acetyl-CoA
palmitate
(●)16
aspartate
oxaloacetate
citrate
CO_2
malate
m+3/m+4
cycle 2
α-KG
CO_2
fumarate
succinate

FIGURE S3 (RELATED TO FIGURE 2): EFFECT OF FAO INHIBITION ON ENERGY HOMEOSTASIS, BIOMASS SYNTHESIS AND HISTONE ACETYLATION (DLL4-INDUCED QEC MODEL).

(**A,B**) qRT-PCR analysis (n=3) (A) and representative immunoblot (B) of CPT1A expression in QECs and PECs transduced with scrambled shRNA (ctrl) or previously characterized CPT1A shRNAs (CPT1A^{KD}#1, n=5; CPT1A^{KD}#2, n=4) (Schoors et al., 2015). α-tubulin is used as loading control for the immunoblots. Densitometric quantification of the ratio of CPT1A to α-tubulin, expressed relative to the levels of control PECs, is shown beneath each blot. (**C**) FAO in PECs and QECs transduced with scrambled shRNA or CPT1A shRNA (shCPT1A^{KD}#1 or shCPT1A^{KD}#2) (n>3). (**D-I**) Comparable energy homeostasis in PECs and QECs, which is unaffected upon silencing of CPT1A as reflected by the unchanged energy charge (([ATP] + 1/2 [ADP]) / ([ATP] + [ADP] + [AMP])) (D) and ATP levels (E) in PECs vs QECs transduced with scrambled shRNA (ctrl) or CPT1A shRNA (CPT1A^{KD}) (n=4) and by equal ATP/ADP ratios in PECs vs QECs (n=5) (F). This is further confirmed by equal oxygen consumption rates (OCR) coupled to ATP synthesis (OCR$_{ATP}$; sensitive to oligomycin) in ctrl and CPT1A^{KD} PECs and QECs (n=3) (G) and the corresponding absence of a prominent impact of oligomycin treatment on the viability of both ctrl and CPT1A^{KD} PECs and QECs (n=3) (H) and finally, by the unaltered ratios of p-AMPK/AMPK (an established read-out for energy stress) as shown by a representative immunoblot of AMPK and p-AMPK in ctrl and CPT1A^{KD} PECs and QECs with α-tubulin as loading control. Densitometric quantification of the ratio of p-AMPK to total AMPK, expressed relative to control PECs, is shown beneath the blot (n=3; p=ns) (I). (**J,K**) Reduced abundances of TCA intermediates (J) and aspartate (precursor for nucleotide synthesis) (K) in QECs vs PECs (n=7). (**L**) Reduced ^{14}C palmitate carbon incorporation into DNA in QECs vs PECs and in ctrl vs CPT1A^{KD} PECs but not in ctrl vs CPT1A^{KD} QECs implying that QECs did not substantially rely on FAO for DNA synthesis. **(M-O)** Cellular content of dATP (M), dTTP (N) and dCTP (O) in QECs *versus* PECs (top panels), and in ctrl vs CPT1A^{KD} QECs (bottom panels) (n=8). QECs had lower dNTP levels than PECs, in agreement with their lower need to synthesize large amounts of dNTPs for DNA synthesis as compared to proliferating cells. CPT1A^{KD} did not further reduce dNTP levels in QECs, confirming that FAO is dispensable for dNTP synthesis in QECs. **(P,Q)** Similar incorporation of ^{14}C palmitate carbon into protein (P) and RNA (Q) in QECs vs PECs, and similar reduction of this incorporation by CPT1A^{KD} in QECs and PECs (n=4), showing that

FAO in QECs is dispensable for biomass synthesis. (**R**) Reduced mRNA levels of key genes involved in nucleotide synthesis (*TK1*, thymidine kinase; *TYMS*, thymidylate synthetase; *RRM1,* ribonucleotide reductase catalytic subunit M1) in QECs vs PECs (n=4). (**S,T**) Comparable levels of histone (S) and total protein (T) acetylation in ctrl and CPT1A^{KD} QECs or PECs. Representative immunoblots for acetylated H2AK5 (acH2AK5), H3K9 (acH3K9), H4K8 (acH4K8) in ctrl and CPT1A^{KD} QECs or PECs with total levels of H2A, H3 and H4 as loading controls are shown. Densitometric quantifications of the ratio of acetylated over total histone levels (n=4) are shown in Table S5 (S). Representative immunoblots for total acetylation of proteins in ctrl and CPT1A^{KD} PECs and QECs with α-tubulin as loading control are shown. Densitometric quantification of the acetylated total protein normalized to α-tubulin and expressed relative to control PECs is shown beneath the blot (n=3) (T). (**U**) Schematic representation of the contribution of fatty acid-derived carbons to TCA cycle intermediates (green during the first cycle (upper panel); blue during the second cycle (bottom panel)), showing the production of m+3 and m+4 TCA cycle intermediates in the second TCA cycle. Carbons released as CO_2 are indicated in red (cycle 1) or green and red (cycle 2). Data in (D-T) were performed using the CPT1A^{KD}#1 shRNA. AU, arbitrary units. DPM, disintegrations per minute. Statistics: ANOVA and Bonferroni post-hoc test (A), one sample t test (B,I, T), mixed models statistics (C,D-G, J-L, P,Q), or two-tailed t test with Welch correction (M-O, R). Data are mean ± SEM; ns, not significant; *p<0.05 vs control PEC; #p<0.05 vs control QEC. See also Table S5.

Figure S4

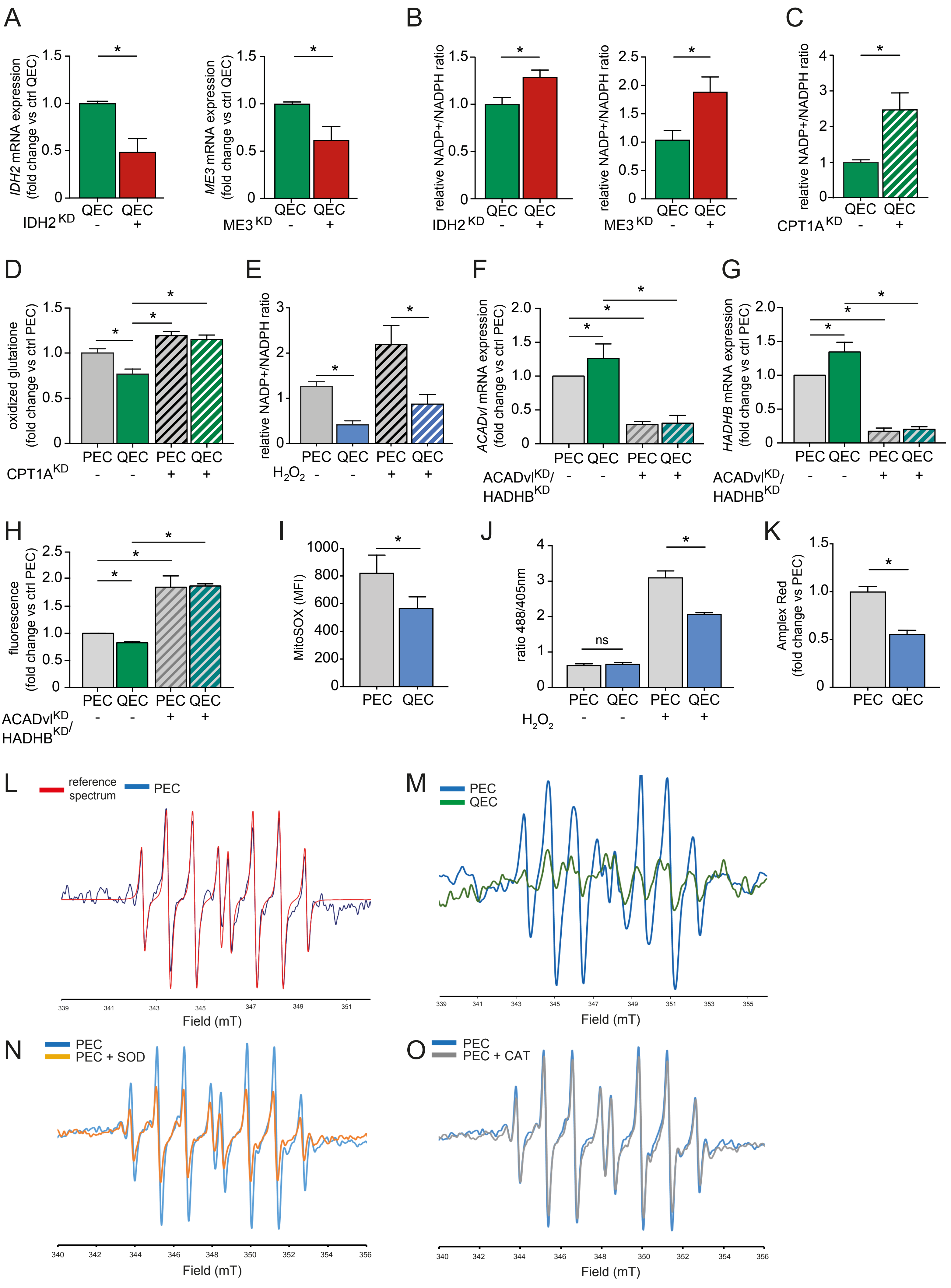
A
IDH2 mRNA expression (fold change vs ctrl QEC)
1.5
1.0
0.5
0
*
QEC QEC
IDH2 KD - +
ME3 mRNA expression (fold change vs ctrl QEC)
ME3 KD - +
B
relative NADP+/NADPH ratio
IDH2 KD - +
2.5
2.0
1.5
1.0
0.5
0
ME3 KD - +
C
relative NADP+/NADPH ratio
4
3
2
1
0
CPT1A KD - +
D
oxidized glutatione (fold change vs ctrl PEC)
PEC QEC PEC QEC
CPT1A KD - - + +
E
relative NADP+/NADPH ratio
3
2
1
0
H_2O_2 - - + +
F
ACADvl mRNA expression (fold change vs ctrl PEC)
2.0
1.5
1.0
0.5
0
ACADvl KD/ HADHB KD - - + +
G
HADHB mRNA expression (fold change vs ctrl PEC)
ACADvl KD/ HADHB KD - - + +
H
fluorescence (fold change vs ctrl PEC)
2.5
2.0
1.5
1.0
0.5
0
ACADvl KD/ HADHB KD/ - - + +
I
MitoSOX (MFI)
1000
800
600
400
200
0
PEC QEC
J
ratio 488/405nm
4
3
2
1
0
ns
H_2O_2 - - + +
K
Amplex Red (fold change vs PEC)
1.5
1.0
0.5
0
PEC QEC
L
reference spectrum
PEC
339 341 343 345 347 349 351
Field (mT)
M
PEC
QEC
339 341 343 345 347 349 351 353 355
Field (mT)
N
PEC
PEC + SOD
340 342 344 346 348 350 352 354 356
Field (mT)
O
PEC
PEC + CAT
340 342 344 346 348 350 352 354 356
Field (mT)

FIGURE S4 (RELATED TO FIGURE 4): ROLE OF FAO IN REDOX HOMEOSTASIS.

(**A**) qRT-PCR analysis of *IDH2* and *ME3* expression in QECs transduced with scrambled shRNA (control), IDH2 shRNA (IDH2^{KD}) or ME3 shRNA (ME3^{KD}) (n=3). (**B,C**) Relative NADP$^+$/ NADPH ratio in ctrl and IDH2^{KD} or ME3^{KD} QECs (n=3) (B) and CPT1A^{KD} QECs (n=3) (C). (**D**) Quantitative analysis of oxidized glutathione (% of total GSSG + GSH, expressed relative to ctrl PECs) in ctrl and CPT1A^{KD} QECs and PECs (n=4). (**E**) Relative NADP$^+$/NADPH ratio in contact-inhibited QECs vs PECs without and with 50 µM H_2O_2 supplementation (n=4). (**F,G**) qRT-PCR analysis of mRNA levels of Acyl-CoA Dehydrogenase, Very Long Chain (*ACADvl*) (F) and hydroxyacyl-CoA dehydrogenase/3-ketoacyl-CoA thiolase/enoyl-CoA hydratase (*HADHB*) (G) in QECs and PECs transduced with scrambled shRNA (control) or ACADvl/HADHB shRNA (ACADvl^{KD}/HADHB^{KD}) (n=3). qRT-PCR data are expressed relative to the levels of non-silenced control PECs. (**H**) Intracellular ROS levels (CM-H_2DCFDA fluorescence) of ctrl and ACADvl^{KD}/ HADHB^{KD} PECs and QECs, expressed relative to the levels of non-silenced control PECs (n=3). (**I**) Significantly decreased mitochondrial $O_2^{\bullet-}$ levels (flow cytometry after incubation with the MitoSOX dye) in contact-inhibited QECs vs PECs (n=4). (**J**) Mitochondrial H_2O_2 levels assessed by HyPER-dMito probe in PECs and contact-inhibited QECs in baseline or upon supplementation with H_2O_2 (50 µM, 15 min). While similar in baseline PECs vs QECs, mitochondrial H_2O_2 was lower in QECs than PECs in stress conditions (H_2O_2 supplementation). Data show the ratio of fluorescence (emission measured at 530 nm) upon excitation at 488 nm (fluorescence increases in the presence of H_2O_2) and 405 nm (fluorescence decreases in the presence of H_2O_2). (**K**) Decreased total H_2O_2 levels in contact-inhibited QECs vs PECs as assessed using the H_2O_2 probe Amplex Red. (**L**) OH$^\circ$ detection by electron paramagnetic resonance (EPR) spectroscopy. Detection of OH$^\circ$ in PEC lysates and specificity of the signal was validated by using a reference spectrum for trans DIPPMPO-OH adducts (a close overlap between the spectrum for PECs and the reference spectrum means high specificity of OH$^\circ$ detection). A representative spectrum of the EPR signal observed with lysate from PECs (blue), and simulation for trans DIPPMPO-OH adduct (red) is shown. **(M)** Representative OH$^\circ$ EPR spectra recorded in PECs (blue) and contact-inhibited QECs (green), showing reduced (close to background) signal in QECs, indicating lower OH$^\circ$ levels in QECs than PECs. (n=3) **(N,O)** Representative OH$^\circ$ EPR spectra recorded in PECs without (blue) or with superoxide dismutase (SOD) treatment (orange) (N) and in PECs without (blue) or with catalase (CAT) treatment (grey) (O). SOD but not catalase treatment reduced the OH° signal, indicating that OH° was derived (at least partly) from $O_2^{\bullet -}$ and not from H_2O_2. Unless otherwise indicated, all experiments were performed using the Dll4 induced quiescence model. Statistics: two-tailed t test with Welch correction (A-C,K), ANOVA and Bonferroni post-hoc test (D,E,J) one sample t test (F-H), mixed models statistics (I). Data are mean ± SEM; *$p<0.05$.

Figure S5

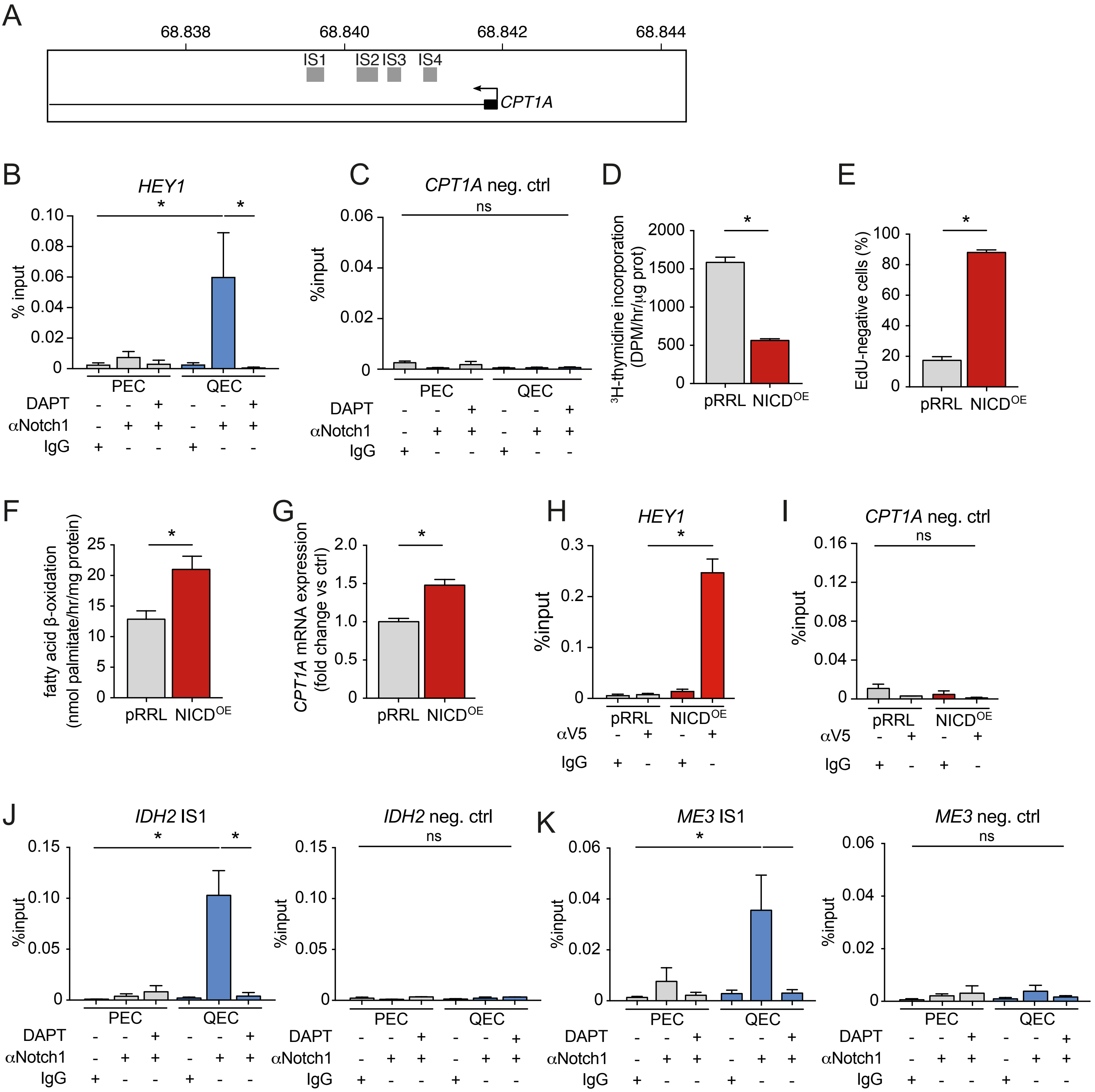
A
68.838
68.840
68.842
68.844
IS1
IS2
IS3
IS4
CPT1A
B
HEY1
% input
0.10
0.08
0.06
0.04
0.02
0
*
*
PEC
QEC
DAPT - - + - - +
αNotch1 - + + - + +
IgG + - - + - -
C
CPT1A neg. ctrl
ns
%input
0.06
0.04
0.02
0
PEC
QEC
DAPT - - + - - +
αNotch1 - + + - + +
IgG + - - + - -
D
^{3}H-thymidine incorporation (DPM/hr/μg prot)
2000
1500
1000
500
0
*
pRRL
NICD^{OE}
E
EdU-negative cells (%)
100
80
60
40
20
0
*
pRRL
NICD^{OE}
F
fatty acid β-oxidation (nmol palmitate/hr/mg protein)
25
20
15
10
5
0
*
pRRL
NICD^{OE}
G
CPT1A mRNA expression (fold change vs ctrl)
2.0
1.5
1.0
0.5
0
*
pRRL
NICD^{OE}
H
HEY1
%input
0.3
0.2
0.1
0
*
pRRL
NICD^{OE}
αV5 - + - +
IgG + - + -
I
CPT1A neg. ctrl
ns
%input
0.16
0.12
0.08
0.04
0
pRRL
NICD^{OE}
αV5 - + - +
IgG + - + -
J
IDH2 IS1
%input
0.15
0.10
0.05
0
*
*
PEC
QEC
DAPT - - + - - +
αNotch1 - + + - + +
IgG + - - + - -
IDH2 neg. ctrl
ns
%input
0.15
0.10
0.05
0
PEC
QEC
DAPT - - + - - +
αNotch1 - + + - + +
IgG + - - + - -
K
ME3 IS1
%input
0.06
0.04
0.02
0
*
PEC
QEC
DAPT - - + - - +
αNotch1 - + + - + +
IgG + - - + - -
ME3 neg. ctrl
ns
%input
0.06
0.04
0.02
0
PEC
QEC
DAPT - - + - - +
αNotch1 - + + - + +
IgG + - - + - -

Figure S5 (related to Figure 5): Effect of Notch-signaling on CPT1A expression.

(**A**) Scheme showing the interaction sites (IS) (grey boxes) of NICD-RBPj within the first intron of *CPT1A* (chromosome 11, human genome build hg38). Numbers above the scheme denote chromosomal location. Black box, exon. (**B**) ChIP-qPCR analysis of NICD interacting with a known NICD-RBPj binding site within the *HEY1* promoter in PECs and contact inhibited QECs, without or with treatment with the γ-secretase inhibitor DAPT (positive control for Fig. 5C, S5J,K). Samples were pulled down with anti-Notch1 (αNotch1) or control IgG antibody (n=4). (**C**) ChIP-qPCR analysis of NICD binding to *CPT1A* using primers spanning a distant fragment within *CPT1A* (lacking a NICD-RBPj binding site), in PECs and contact inhibited QECs, without or with treatment with DAPT (negative control for Fig. 5C; the data are displayed using the same Y-axis scale as in Fig. 5C to demonstrate background level of the amplification signal). Samples were pulled down with anti-Notch1 (αNotch1) or control IgG antibody (n=3; p=ns). (**D**) ^{3}H-thymidine incorporation into DNA (proliferation assay) in NICD overexpressing (NICD^{OE}) ECs as compared to ECs transduced with a control vector (pRRL) (n=3). DPM, disintegrations per minute. (**E**) Percentage of EdU^{neg} cells (EdU incorporation assay) in control ECs (empty vector; pRRL) and ECs upon NICD overexpression (NICD^{OE}) (n=3). (**F**) FAO flux in NICD overexpressing (NICD^{OE}) ECs as compared to ECs transduced with a control vector (pRRL) (n=3). (**G**) qRT-PCR analysis of *CPT1A* expression in NICD overexpressing (NICD^{OE}) ECs as compared to ECs transduced with a control vector (pRRL) (n=3). (**H**) ChIP-qPCR analysis of NICD interacting with a known NICD-RBPj binding site within the *HEY1* promoter upon control (pRRL) or overexpression of V5-tagged NICD (NICD^{OE}) (positive control for Fig. 5D). Samples were pulled down with anti-V5 (αV5) or control IgG antibody (G) (n=4). (**I**) ChIP-qPCR analysis of NICD binding to *CPT1A* using primers spanning a distant fragment within *CPT1A* (lacking a NICD-RBPj binding site) upon control (pRRL) or overexpression of V5-tagged NICD (NICD^{OE}) (negative control for Fig. 5D; the data are displayed using the same Y-axis scale as in Fig. 5D to demonstrate background level of the amplification signal). Samples were pulled down with anti-V5 (αV5) or control IgG antibody (n=3; p=ns). (**J**) ChIP-qPCR analysis of NICD binding to the IDH2 promoter at the binding site (IS) 1 (left) or using primers spanning a distant fragment within IDH2 (lacking a NICD-RBPj binding site) (right, negative control) in PECs and contact inhibited QECs, without or with treatment with the γ- secretase inhibitor DAPT. Samples were pulled down with anti-Notch1 (αNotch1) or control IgG antibody (n=5). (**K**) ChIP-qPCR analysis of NICD binding to the ME3 promoter at the binding site (IS) 1 (left) or using primers spanning a distant fragment within ME3 (lacking a NICD-RBPj binding site) (right, negative control) in PECs and contact inhibited QECs, without or with treatment with the γ- secretase inhibitor DAPT. Samples were pulled down with anti-Notch1 (αNotch1) or control IgG antibody (n=5). Data in (B,C,H-K) are presented as percentage of input. Statistics: by ANOVA and Bonferroni post-hoc test (B,C,H-K), mixed models statistics (D-F), or two-tailed t test with Welch correction (G). Data are mean ± SEM; ns, not significant; *$p<0.05$.

Figure S6

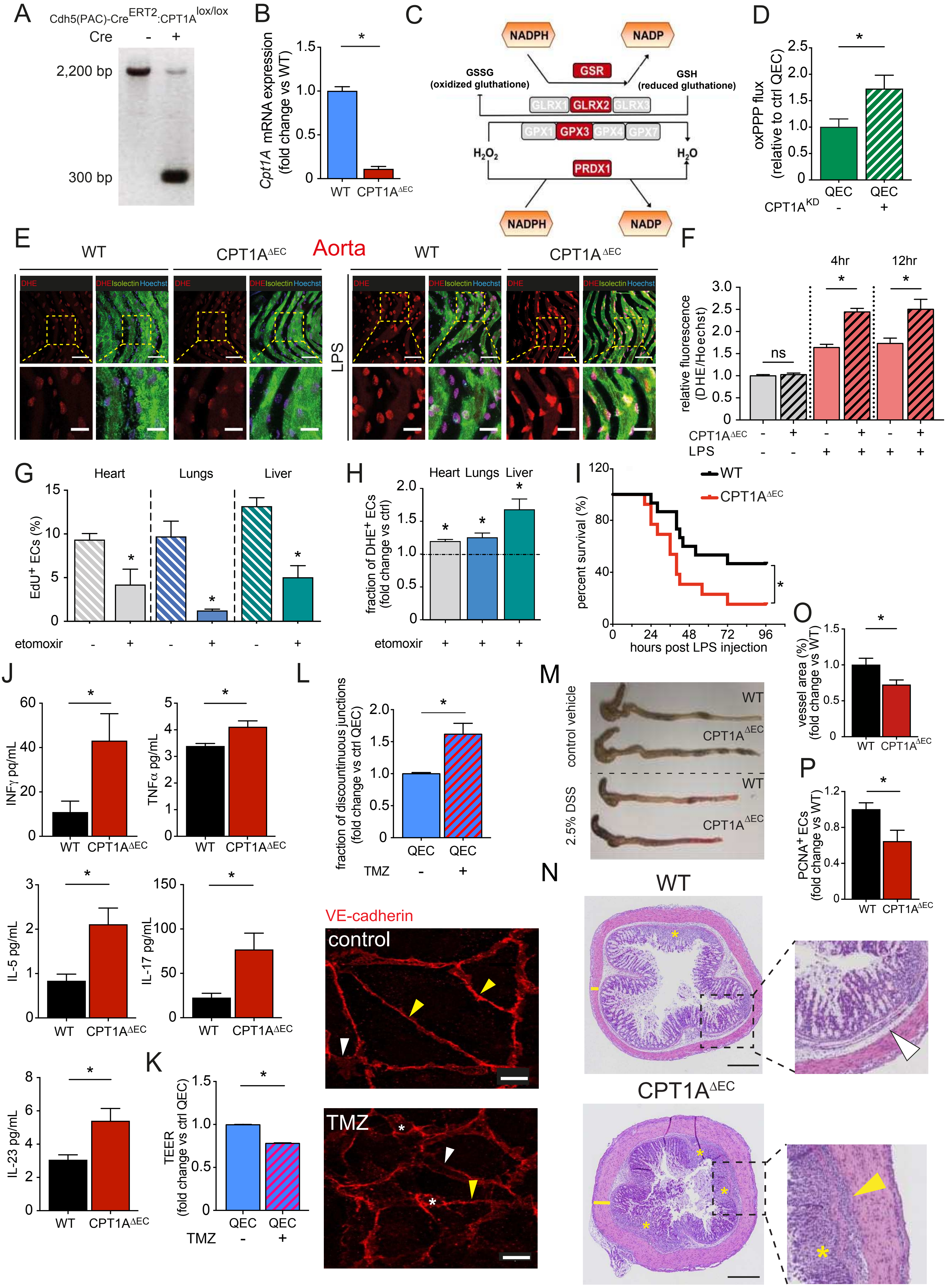
A
Cdh5(PAC)-Cre^{ERT2}:CPT1A$^{lox/lox}$
Cre - +
2,200 bp
300 bp
B
Cpt1A mRNA expression (fold change vs WT)
1.5 1.0 0.5 0
*
WT CPT1A$^{\Delta EC}$
C
NADPH
NADP
GSR
GSSG (oxidized gluthatione)
GSH (reduced gluthatione)
GLRX1 GLRX2 GLRX3
GPX1 GPX3 GPX4 GPX7
H_2O_2
H_2O
PRDX1
NADPH
NADP
D
oxPPP flux (relative to ctrl QEC)
2.5 2.0 1.5 1.0 0.5 0
*
QEC QEC
CPT1A^{KD} - +
E
WT CPT1A$^{\Delta EC}$
Aorta
WT CPT1A$^{\Delta EC}$
DHE
DHE Isolectin Hoechst
LPS
F
4hr 12hr
relative fluorescence (DHE/Hoechst)
3.0 2.5 2.0 1.5 1.0 0.5 0
ns * *
CPT1A$^{\Delta EC}$ - + - + - +
LPS - - + + + +
G
Heart Lungs Liver
EdU$^+$ ECs (%)
15 10 5 0
* * *
etomoxir - + - + - +
H
Heart Lungs Liver
fraction of DHE$^+$ ECs (fold change vs ctrl)
2.0 1.5 1.0 0.5 0
* * *
etomoxir + + +
I
WT
CPT1A$^{\Delta EC}$
percent survival (%)
120 80 40 0
0 24 48 72 96
hours post LPS injection
*
O
vessel area (%) (fold change vs WT)
1.5 1.0 0.5 0
*
WT CPT1A$^{\Delta EC}$
J
INFγ pg/mL
60 40 20 0
*
WT CPT1A$^{\Delta EC}$
TNFα pg/mL
5 4 3 2 1 0
*
WT CPT1A$^{\Delta EC}$
IL-5 pg/mL
3 2 1 0
*
WT CPT1A$^{\Delta EC}$
IL-17 pg/mL
150 100 50 0
*
WT CPT1A$^{\Delta EC}$
IL-23 pg/mL
8 6 4 2 0
*
WT CPT1A$^{\Delta EC}$
K
TEER (fold change vs ctrl QEC)
1.5 1.0 0.5 0
*
QEC QEC
TMZ - +
L
fraction of discountinuous junctions (fold change vs ctrl QEC)
2.0 1.5 1.0 0.5 0
*
QEC QEC
TMZ - +
VE-cadherin
control
TMZ
*
*
M
control vehicle
2.5% DSS
WT
CPT1A$^{\Delta EC}$
WT
CPT1A$^{\Delta EC}$
P
PCNA$^+$ ECs (fold change vs WT)
1.2 0.8 0.4 0
*
WT CPT1A$^{\Delta EC}$
N
WT
*
CPT1A$^{\Delta EC}$
* * * *
*

FIGURE S6 (RELATED TO FIGURE 6): ROLE OF FAO IN VASCULOPROTECTION *IN VITRO* AND *IN VIVO.*

(**A**) Genotyping for the presence of the CPT1A floxed (2,200 bp) and excision band (300 bp) in mouse tail genomic DNA isolated from WT and CPT1A$^{\Delta EC}$ littermates after tamoxifen treatment of Cdh5(PAC)-Cre^{ERT2}:CPT1A$^{lox/lox}$ mice. (**B**) qRT-PCR analysis of *Cpt1A* expression in isolated liver ECs of WT or CPT1A$^{\Delta EC}$ mice (n=5). (**C**) Pathway map showing changes in transcript levels of genes involved in glutathione metabolism in ECs isolated from WT and CPT1A$^{\Delta EC}$ mice (color scale: red, upregulated genes by at least 15%; gray: unchanged, change <15%). For full gene names, see Table S6. (**D**) oxPPP flux in ctrl and CPT1A^{KD} QECs (n=3). (**E**,**F**) Superoxide formation in the aorta of WT or CPT1A$^{\Delta EC}$ mice at 4 and 12 hours after injection of vehicle (PBS) or LPS. Superoxide formation is evaluated with the oxidative fluorescent dye DHE. (E) Representative photomicrographs of aorta open book preparations from mice treated for 12 hours, stained for DHE (red), the EC marker isolectin B4A (green) and nuclei (Hoechst; blue). Lower panels show larger magnifications of the boxed areas in the upper panels. Scale bar: 50 µm for upper panels and 20 µm in lower panels. (F) Quantification of $O_2^{\cdot -}$ formation (DHE fluorescence normalized for Hoechst fluorescence) of the aorta open book preparations from wild type and CPT1A$^{\Delta EC}$ mice treated with vehicle or LPS for 4 or 12 hours (n=3 independent experiments, each comprising n>4 mice per group). (**G**) Percentage of EdU^{+} ECs in the indicated tissues of control (vehicle) and etomoxir treated P8 neonates (48 hr; 30 mg/kg) (flow cytometry analysis upon staining for EdU, n=4). (**H**) Fraction of DHE^{+} ECs in the indicated tissues of control (vehicle) and etomoxir treated P8 neonates (48 hr; 30 mg/kg). The values are expressed relative to vehicle treated control (dashed horizontal line) (flow cytometry analysis upon staining for DHE to measure cellular ROS levels, n=4). (**I**) Survival curve of WT and CPT1A$^{\Delta EC}$ mice after injection of 10 mg/kg LPS intraperitoneally (n≥7). (**J**) Levels of pro-inflammatory cytokines (IFNγ, TNFα, IL-5, IL-17, IL-23) in serum of WT and CPT1A$^{\Delta EC}$ mice 24 hours after injection of 10 mg/kg LPS intraperitoneally (n≥5). (**K**) TEER measurement of QEC monolayers treated with vehicle (control) or the long-chain 3-ketoacyl CoA thiolase (LC 3-KAT) inhibitor trimetazidine (TMZ) (n=4). (**L**) Quantification of discontinuous junctions in QECs with vehicle (control) or with TMZ treatment. Representative images of QECs, stained for VE-cadherin (red) without (vehicle) or with TMZ treatment are shown. Scale bar: 10 µm. White arrowheads denote discontinuous junctions, yellow arrowheads denote continuous junctions, asterisk denotes a gap between ECs resulting from discontinuous junctions. (**M**) Representative images of colons of WT and CPT1A$^{\Delta EC}$ mice treated with control vehicle or 2.5% DSS in their drinking water for 7 consecutive days. (**N**) Representative images of hematoxylin and eosin stained sections of colon from WT and CPT1A$^{\Delta EC}$ mice after DSS treatment. Right panels are magnifications of the respective boxed areas. Asterisks denote loss of crypts; white arrowhead indicates separation of the crypt base from the muscularis mucosa (WT), yellow arrowhead denotes more severe separation of the crypt base from the muscularis mucosa, infiltrated with inflammatory cells (CPTA1$^{\Delta EC}$); yellow lines visualize the thickness of the colonic wall. Scale bar: 500 µm. (**O**) Quantification of the vessel area in the colonic mucosa from WT and CPT1A$^{\Delta EC}$ mice after DSS treatment (n=10). (**P**) Quantification of proliferating PCNA^{+} ECs in WT and CPT1A$^{\Delta EC}$ mice after DSS treatment (n=10). Statistics: two-tailed t test with Welch correction (B,D,F,G,H,J,K,L,O,P) or by log-rank test for survival curve comparison (I). Data are mean ± SEM; ns, not significant; $^{*}p<0.05$. See also Table S6.

Figure S7

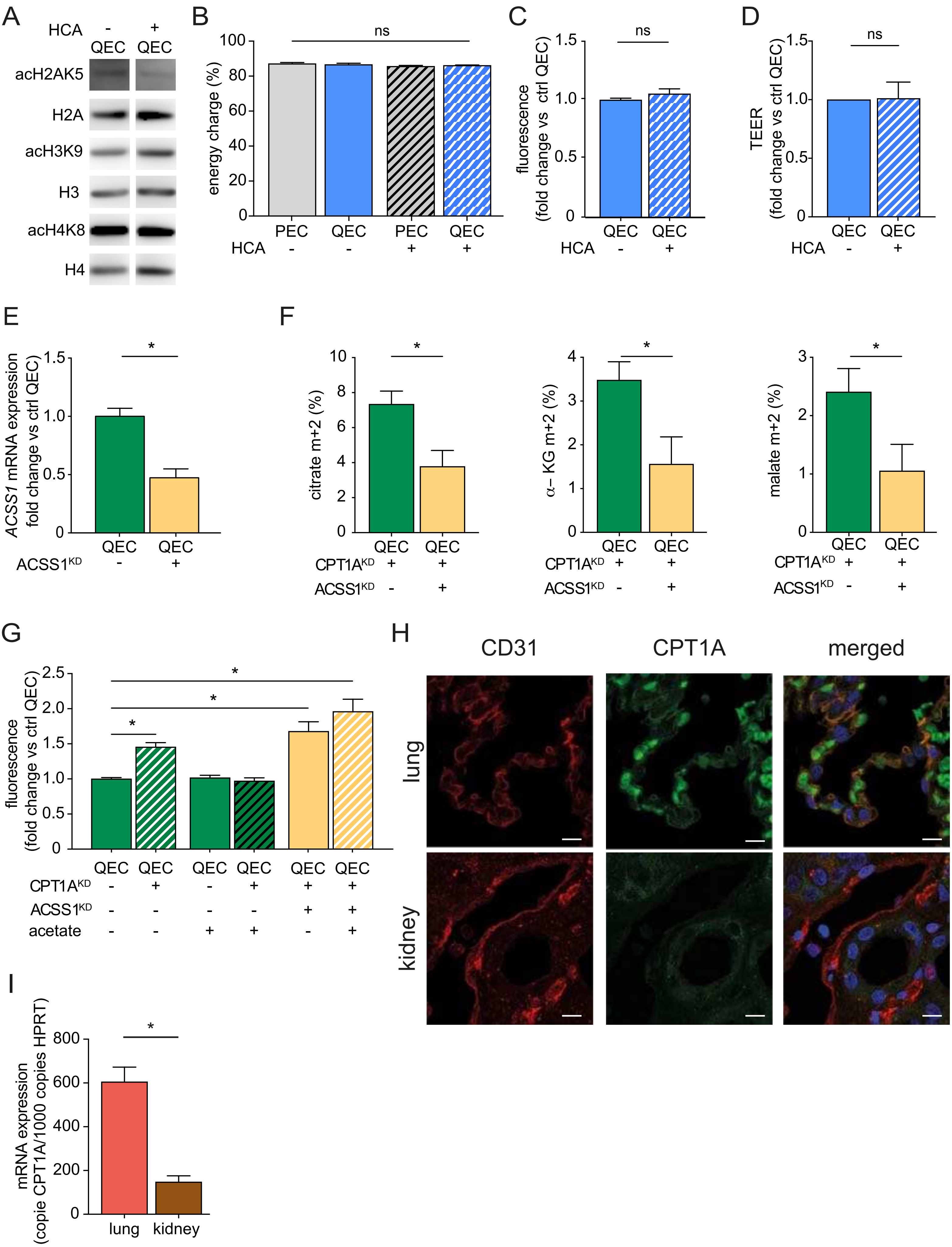
A
HCA - +
QEC QEC
acH2AK5
H2A
acH3K9
H3
acH4K8
H4
B
ns
energy charge (%)
100
80
60
40
20
0
PEC QEC PEC QEC
HCA - - + +
C
ns
fluorescence (fold change vs ctrl QEC)
1.5
1.0
0.5
0
QEC QEC
HCA - +
D
ns
TEER (fold change vs ctrl QEC)
1.5
1.0
0.5
0
QEC QEC
HCA - +
E
*
ACSS1 mRNA expression fold change vs ctrl QEC)
1.5
1.0
0.5
0
QEC QEC
ACSS1KD - +
F
*
citrate m+2 (%)
10
8
6
4
2
0
QEC QEC
CPT1AKD + +
ACSS1KD - +
*
α– KG m+2 (%)
4
3
2
1
0
QEC QEC
CPT1AKD + +
ACSS1KD - +
*
malate m+2 (%)
3
2
1
0
QEC QEC
CPT1AKD + +
ACSS1KD - +
G
*
*
*
fluorescence (fold change vs ctrl QEC)
2.5
2.0
1.5
1.0
0.5
0
QEC QEC QEC QEC QEC QEC
CPT1AKD - + - + + +
ACSS1KD - - - - + +
acetate - - + + - +
H
CD31
CPT1A
merged
lung
kidney
I
*
mRNA expression (copie CPT1A/1000 copies HPRT)
800
600
400
200
0
lung kidney

FIGURE S7 (RELATED TO FIGURE 7): MECHANISMS OF ACETATE RESCUE.

(A-D) QECs treated with hydroxycitrate (HCA, 1mM), an inhibitor of ATP citrate lyase, the enzyme that converts citrate to acetyl-CoA, did not show any differences in histone acetylation (A), energy charge (B), ROS levels (C) and endothelial barrier integrity measured by TEER (D). (A) Representative immunoblots for acetylated H2AK5 (acH2AK5), H3K9 (acH3K9) and H4K8 (acH4K8) in QECs treated with vehicle (control) or HCA. Total levels of H3, H2A, and H4 were used as loading controls. Densitometric quantifications of the ratio of acetylated proteins over total proteins levels (n=3) are shown in Table S7. (B) Energy charge (([ATP] + 1/2 [ADP]) / ([ATP] + [ADP] + [AMP])) in QECs vs PECs treated with vehicle (control) or HCA (n=5). (C) Quantification of intracellular ROS levels (CM-H_2DCFDA fluorescence) in QECs treated with vehicle (control) or HCA upon supplementation with H_2O_2 (50 µM, 2hr) (n=4). (D) TEER analysis of QECs treated with vehicle (control) or HCA (n=3). (**E-G**) Knock-down of acyl-CoA synthetase short chain family member 1 (ACSS1), converting acetate to acetyl-CoA in mitochondria, confirmed that QECs use acetate to sustain the TCA cycle and redox homeostasis. (E) qRT-PCR analysis of mRNA levels of ACSS1 in ctrl and ACSS1^{KD} QECs (n=3). (F) Analysis of m+2 labeled TCA intermediates (from [U-^{13}C]-acetate) in CPT1A^{KD} QECs upon transduction with scramble shRNA or ACCS1 knockdown (ACSS1^{KD}), showing lower ^{13}C-acetate incorporation in citrate, α-KG and malate in CPT1A^{KD}/ACSS1^{KD} QECs than CPT1A^{KD} QECs (n=5). (G) Quantification of intracellular ROS levels (CM-H_2DCFDA fluorescence) control and CPT1A^{KD} QECs with additional transduction with scramble shRNA or ACCS1 knockdown (ACSS1^{KD}), exposed to H_2O_2 (50 µM, 2 hr) and treated with control vehicle or 500 µM acetate (n=4), showing that ACSS1^{KD} inhibited the acetate-mediated rescue of the elevated ROS levels in CPT1A^{KD} QECs. Elevated levels in QECs, in which both ACSS1 and CPT1A were silenced, may be attributable to the excess stress due to double viral transductions and/or may suggest use of acetate from endogenous/exogenous (not additionally supplemented) sources. (**H**) Representative images of immunostaining for CD31 (red), CPT1A (green) and nuclei (blue) in different human organs (lung, more highly oxygenated tissue; kidney, poorly oxygenated tissue). Scale bar: 10 µm. (**I**) qRT-PCR analysis of *CPT1A* expression in QECs from human lung and kidney. Statistics: mixed models statistics (B, F, I), two-tailed t test with Welch correction (C, E), one sample t test (D) or by ANOVA and Bonferroni post-hoc test (G). Data are mean ± SEM; ns, not significant, *$p<0.05$. See also Table S7.

SUPPLEMENTAL TABLES

TABLE S1: ROAST ANALYSIS OF TRANSCRIPTOMIC DATA SHOWING MOST REGULATED PATHWAYS IN QECS COMPARED TO PECS (RELATED TO FIGURE 1)

Pathway	**NGenes**	**PropDown**	**PropUp**	**Direction**	**p value**	**FDR-adjusted p value**
Fatty acid oxidation	22	23%	59%	Up	1.00E-04	1.00E-04
Glycolysis	21	71%	10%	Down	1.00E-04	1.00E-04
Serine/glycine metabolism	11	64%	0%	Down	1.00E-04	1.00E-04
Tricarboxylic acid cycle	24	63%	21%	Down	1.00E-04	1.00E-04
1-carbon metabolism	33	42%	36%	Down	8.50E-03	1.21E-02
Pentose phosphate pathway	10	40%	40%	Down	2.84E-01	3.54E-01
Nucleotide degradation	12	50%	33%	Down	1.00E-04	1.00E-04
Nucleotide synthesis	33	67%	15%	Down	1.00E-04	1.00E-04
Oxidative phosphorylation	102	36%	39%	Down	5.40E-01	6.00E-01
Fatty acid synthesis	11	45%	36%	Down	7.41E-01	7.41E-01

NGenes: number of genes in set; PropDown, proportion of genes in set with z < sqrt(2); PropUp: proportion of genes in set with z > sqrt(2); Direction: direction of change, “Up” or “Down”; Statistics: two-sided directional p value; FDR-adjusted p value: two-sided directional false discovery rate. NOTE: ROAST analyzes both the oxidative pentose phosphate pathway (oxPPP) and non-oxidative PPP (non-oxPPP) together, explaining the observed FDR-adjusted p value, but subsequent heatmap analysis and pathway mapping revealed that expression of oxPPP genes was upregulated, while that of non-oxPPP genes was downregulated in QECs as compared to PECs (Fig. 1C,D).

TABLE S2: LIST OF GENES ENCODING ENZYMES OF CENTRAL CARBON METABOLISM (RELATED TO FIGURE 1)

Pathway	**Symbol**	**Gene name**
Fatty acid oxidation	ACAA1	acetyl-CoA acyltransferase 1
	ACAA2	acetyl-CoA acyltransferase 2
	ACADM	acyl-CoA dehydrogenase, C-4 to C-12 straight chain
	ACADS	acyl-CoA dehydrogenase, C-2 to C-3 short chain
	ACADVL	acyl-CoA dehydrogenase, very long chain
	ACSL1	acyl-CoA synthetase long-chain family member 1
	ACSL3	acyl-CoA synthetase long-chain family member 3
	ACSL4	acyl-CoA synthetase long-chain family member 4
	ACSL5	acyl-CoA synthetase long-chain family member 5
	CPT1A	carnitine palmitoyltransferase 1A
	CPT1B	carnitine palmitoyltransferase 1B
	CPT1C	carnitine palmitoyltransferase 1C
	CPT2	carnitine palmitoyltransferase 2
	FABP4	fatty acid binding protein 4
	FABP5	fatty acid binding protein 5
	HADHA	hydroxyacyl-CoA dehydrogenase/3-ketoacyl-CoA thiolase/enoyl-CoA hydratase (trifunctional protein), alpha subunit
	HADHB	hydroxyacyl-CoA dehydrogenase/3-ketoacyl-CoA thiolase/enoyl-CoA hydratase (trifunctional protein), beta subunit
Glycolysis & link to TCA cycle	ALDOA	aldolase, fructose-bisphosphate A
	DLAT	dihydrolipoamide S-acetyltransferase
	DLD	dihydrolipoamide dehydrogenase
	ENO1	enolase 1, (alpha)
	GAPDH	glyceraldehyde-3-phosphate dehydrogenase
	GPI	glucose-6-phosphate isomerase
	LDHA	lactate dehydrogenase A
	LDHB	lactate dehydrogenase B
	PDHA1	pyruvate dehydrogenase (lipoamide) alpha 1
	PDHA2	pyruvate dehydrogenase (lipoamide) alpha 2
	PDHB	pyruvate dehydrogenase (lipoamide) beta
	PFKL	phosphofructokinase, liver type
	PFKM	phosphofructokinase, muscle
	PFKP	phosphofructokinase, platelet
	PGAM1	phosphoglycerate mutase 1
	PGAM4	phosphoglycerate mutase family member 4
	PGM1	phosphoglucomutase 1
	PGM2	phosphoglucomutase 2

	PKLR	pyruvate kinase, liver and RBC
Serine biosynthesis	PHGDH	phosphoglycerate dehydrogenase
	PSAT1	phosphoserine aminotransferase 1
	PSPH	phosphoserine phosphatase
	SHMT1	serine hydroxymethyltransferase 1
	SHMT2	serine hydroxymethyltransferase 2
One carbon metabolism	DHFR	dihydrofolate reductase
	MTHFD1	MTHFD1 methylenetetrahydrofolate dehydrogenase, cyclohydrolase and formyltetrahydrofolate synthetase 1
	MTHFD2	methylenetetrahydrofolate dehydrogenase (NADP+ dependent) 2, methenyltetrahydrofolate cyclohydrolase
Oxidative PPP	G6PDH	glucose-6-phosphate dehydrogenase
	H6PD	hexose-6-phosphate dehydrogenase
	6PGDH	6-phosphogluconate dehydrogenase
	PGLS	6-phosphogluconolactonase
Non-oxidative PPP	RPE	ribulose-5-phosphate-3-epimerase
	RPIA	ribose 5-phosphate isomerase A
	TKT	transketolase
Tricarboxylic acid cycle	ACO1	aconitase 1
	ACO2	aconitase 2
	CS	citrate synthase
	DLST	dihydrolipoamide S-succinyltransferase (E2 component of 2-oxo-glutarate complex)
	FH	fumarate hydratase
	MDH1	malate dehydrogenase 1
	MDH2	malate dehydrogenase 2
	OGDH	oxoglutarate (alpha-ketoglutarate) dehydrogenase (lipoamide)
	SDHA	succinate dehydrogenase complex flavoprotein subunit A
	SDHB	succinate dehydrogenase complex iron sulfur subunit B
	SDHC	succinate dehydrogenase complex subunit C
	SDHD	succinate dehydrogenase complex subunit D
	SUCLA2	succinate-CoA ligase, ADP-forming, beta subunit
	SUCLG1	succinate-CoA ligase, alpha subunit
	SUCLG2	succinate-CoA ligase, GDP-forming, beta subunit
	NNT	nicotinamide nucleotide transhydrogenase

TABLE S3: LIST OF GENES ENCODING ENZYMES OF NUCLEOTIDE SYNTHESIS (RELATED TO FIGURE 1 AND FIGURE S1E)

Pathway	Symbol	Gene name
Nucleotide synthesis	AK1	adenylate kinase 1
	AK2	adenylate kinase 2
	AK3	adenylate kinase 3
	AK4	adenylate kinase 4
	AK5	adenylate kinase 5
	APRT	adenine phosphoribosyltransferase
	CMPK1	cytidine/uridine monophosphate kinase 1
	CMPK2	cytidine/uridine monophosphate kinase 2
	CTPS1	CTP synthase 1
	CTPS2	CTP synthase 2
	DTYMK	deoxythymidylate kinase
	HPRT1	hypoxanthine phosphoribosyltransferase 1
	NME1	NME/NM23 nucleoside diphosphate kinase 1
	NME2	NME/NM23 nucleoside diphosphate kinase 2
	NME3	NME/NM23 nucleoside diphosphate kinase 3
	NME4	NME/NM23 nucleoside diphosphate kinase 4
	NME5	NME/NM23 family member 5
	NME6	NME/NM23 nucleoside diphosphate kinase 6
	NME7	NME/NM23 family member 7
	PPAT	phosphoribosyl pyrophosphate amidotransferase
	RRM1	ribonucleotide reductase catalytic subunit M1
	RRM2	ribonucleotide reductase regulatory subunit M2
	RRM2B	ribonucleotide reductase regulatory TP53 inducible subunit M2B
	TYMS	thymidylate synthetase
	TK1	thymidine kinase 1, soluble
	TK2	thymidine kinase 2, mitochondrial

TABLE S4: DENSITOMETRIC QUANTIFICATION OF BAND INTENSITIES OF THE BLOT IN FIG. 2H (RELATED TO FIGURE 2)

	NICD/α-tubulin	**CPT1A/α-tubulin**	**PFKFB3/α-tubulin**
Day 1	1	1	1
Day 2	2.88 ± 0.62 ns	0.83 ± 0.98 ns	1.33 ± 0.12 ns
Day 3	8.36 ± 2.16 *	0.89 ± 0.18 ns	1.09 ± 0.22 ns
Day 4	14.17 ± 4.14 *	1.63 ± 0.19 *	0.66 ± 0.07 *
Day 5	10.39 ± 2.77 *	2.27 ± 0.27 *	0.59 ± 0.15 *
Day 6	13.05 ± 3.30 *	2.15 ± 0.31 *	0.65 ± 0.11 *

Data are mean ± SEM; ns, not significant, *p<0.05 vs day 1 by one sample t test.

TABLE S5: DENSITOMETRIC QUANTIFICATION OF BAND INTENSITIES OF THE BLOT IN FIG. S3S (RELATED TO FIGURE 2)

	acH2AK5/H2A	**acH3K9/H3**	**acH4K8/H4**
PEC	1	1	1
QEC	1,70 ± 0,32 ns	1,31 ± 0,12 ns	1,03 ± 0,19 ns
PEC + CPT1a^{KD}	1,33 ± 0,34 ns	1,79 ± 0,45 ns	1,09 ± 0,47 ns
QEC + CPT1a^{KD}	1,21 ± 0,37 ns	1,80 ± 0,41 ns	1,51 ± 0,36 ns

Data are mean ± SEM; ns, not significant vs PEC by one sample t test.

TABLE S6: LIST OF GENES ENCODING ENZYMES OF GLUTATHIONE METABOLISM LISTED IN FIGURE S6C (RELATED TO FIGURE 6)

Pathway	**Symbol**	**Gene name**
Gluthathione metabolism	GCLM	glutamate-cysteine ligase modifier subunit
	GCLC	glutamate-cysteine ligase catalytic subunit
	GLRX1	glutaredoxin 1
	GLRX2	glutaredoxin 2
	GLRX3	glutaredoxin 3
	GSS	glutathione synthetase
	GSR	glutathione reductase
	GPX1	glutathione peroxidase 1
	GPX3	glutathione peroxidase 3
	GPX4	glutathione peroxidase 4
	GPX7	glutathione peroxidase 7
	PRDX1	peroxiredoxin 1

TABLE S7: DENSITOMETRIC QUANTIFICATION OF BAND INTENSITIES OF THE IN BLOT FIG. S7A (RELATED TO FIGURE 7)

	acH2AK5/H2A	acH3K9/H3	acH4K8/H4
QEC	1	1	1
QEC + HCA	0,94 ± 0,18 ^{ns}	4,8 ± 3,42^{ns}	0,80 ± 0,04 ^{ns}

HCA, hydroxycitrate. Data are mean ± SEM; ns, not significant vs control QEC by one sample t test.

TABLE S8: LIST OF OLIGONUCLEOTIDES USED FOR CHIP-QPCR, QRT-PCR AND SHRNA GENE SILENCING (RELATED TO KEY RESOURCE TABLE)

	Oligonucleotide	Sequence / ID number
ChiP-qPCR primers	CPT1A negative control set Forward	GCTGATGACGGCTATGGTGT
	CPT1A negative control set Reverse	CGTCTCAGGGCAAGAGAACT
	CPT1A PP1 Forward	GACAGCGGGAGAAATGCAAC
	CPT1A PP1 Reverse	GCCCCGAGTGCTCATTCATAA
	CPT1A PP2 Forward	TGCTGATAGTCCCCAGACCA
	CPT1A PP2 Reverse	CTTCCACAGGTGTCCGGTTT
	CPT1A PP3 Forward	GAGAGGAACCGAAAGCCTGT
	CPT1A PP3 Reverse	CGCCCTTGGCTTTCGTTAAA
	HEY1 Forward	AATTCAGCGGCGCGAGA
	HEY1 Reverse	CTCACGCTTTGCCTCTGGTTA
	IDH2 negative control set Forward	TCCTCGACACCATCAAGAGC
	IDH2 negative control set Reverse	ATCCCCTAGAAAGGCCTCCAG
	IDH2 PP1 Forward	GCCCTTTGTGCGCCTGA
	IDH2 PP1 Reverse	CCCCAGCTGCGACGTG
	ME3 negative control set Forward	GTCTGGAGTGTAGACCAGGG
	ME3 negative control set Reverse	TCGACTACGCGTACAAACACA
	ME3 PP1 Forward	GGAGCTGGTGAGTTCCTCAA
	ME3 PP1 Reverse	GCCAAGATGGAGAGTCTCCAGG
qRT-PCR primers	hCPT1A	Hs.PT.58.15595902
	hDLL4	Hs.PT.56a.3416363
	hGLRX (GRX)	Hs.PT.58.27459908
	hHES1	Hs.PT.56a.4181121
	hHES2	Hs.PT.58.20440320.g
	hHEY1	Hs.PT.56a.38951967
	hHPRT	Hs.PT.58.2145446
	hIDH1	Hs.PT.58.39451262
	hIDH2	Hs.PT.53a.4256195
	hME1	Hs.PT.58.38957126
	hME2	Hs.PT.56a.27979491
	hME3	Hs.PT.58.1622989
	hNADSYN1	Hs.PT.58.3735792

	hNAPRT1	Hs.PT.58.39886719
	hNMRK1	Hs.PT.58.1334287
	hNNMT	Hs.PT.58.26066181.g
	hNNT	Hs.PT.58.2919060
	hNOS3 (eNOS)	Hs.PT.58.21447620
	hPTGS1	Hs.PT.58.47173257
	hRRM1	Hs.PT.58.3077760
	hSerpine1	Hs.PT.58.3938488.g
	hTK1	Hs.PT.58.4323868
	hTYMS	Hs.PT.58.20192843
	mCPT1A	Mm.PT.56a.23381430
	mG6PDX	Mm.PT.58.13826440
	mGLRX2	Mm.PT.58.32498587
	mGPX3	Mm.PT.58.29885432
	mHPRT	Mm.PT.42.12662529
	mPRDX1	Mm.PT.49a.10082950.g
shRNA oligonucleotides	ACADvl	SHCLNV-NM_000018 CCGGGCAGACATCTTCACGGTCTTTCTCGAGAAAGACCGTGAAGATGTCTGCTTTTT
	ACSS1	SHCLNV-NM_032501: TRCN0000045381 CCGGCAAGGTGGTTATCACCTTCAACTCGAGTTGAAGGTGATAACCACCTTGTTTTTG
	CPT1A sequence 1	Schoors et al., 2015 GCCATGAAGCTCTTAGACAAA
	CPT1A sequence 2	Schoors et al., 2015 CGATGTTACGACAGGTGGTTT
	HADHB	SHCLNV-NM_000183: TRCN0000245333 CCGGCGTTAGCCAAACCCAATATAACTCGAGTTATATTGGGTTTGGCTAACGTTTTTG
	IDH2	SHCLNV-NM_002168: TRCN0000027245 CCGGCGACTTCGACAAGAATAAGATCTCGAGATCTTATTCTTGTCGAAGTCGTTTTT
	ME3	SHCLNV-NM_006680: TRCN0000064835 CCGGCGACTGTCTTTAATCTCTAAACTCGAGTTTAGAGATTAAAGACAGTCGTTTTTG
	scramble	SHC002V CCGGCAACAAGATGAAGAGCACCAACTC